3-29-2017 12:00 AM

Developments in PET-MRI for Radiotherapy Planning Applications

John Christian Patrick, *The University of Western Ontario*

Supervisor: Dr. Stewart Gaede, *The University of Western Ontario*

A thesis submitted in partial fulfillment of the requirements for the Doctor of Philosophy degree in Medical Biophysics

Recommended Citation

Patrick, John Christian, "Developments in PET-MRI for Radiotherapy Planning Applications" (2017). *Electronic Thesis and Dissertation Repository*. 4535.
https://ir.lib.uwo.ca/etd/4535

Abstract

The hybridization of magnetic resonance imaging (MRI) and positron emission tomography (PET) provides the benefit of soft-tissue contrast and specific molecular information in a simultaneous acquisition. The applications of PET-MRI in radiotherapy are only starting to be realised. However, quantitative accuracy of PET relies on accurate attenuation correction (AC) of, not only the patient anatomy but also MRI hardware and current methods, which are prone to artefacts caused by dense materials. Quantitative accuracy of PET also relies on full characterization of patient motion during the scan. The simultaneity of PET-MRI makes it especially suited for motion correction. However, quality assurance (QA) procedures for such corrections are lacking. Therefore, a dynamic phantom that is PET and MR compatible is required. Additionally, respiratory motion characterization is needed for conformal radiotherapy of lung. 4D-CT can provide 3D motion characterization but suffers from poor soft-tissue contrast. In this thesis, I examine these problems, and present solutions in the form of improved MR-hardware AC techniques, a PET/MRI/CT-compatible tumour respiratory motion phantom for QA measurements, and a retrospective 4D-PET-MRI technique to characterise respiratory motion.

Chapter 2 presents two techniques to improve upon current AC methods that use a standard helical CT scan for MRI hardware in PET-MRI. One technique uses a dual-energy computed tomography (DECT) scan to construct virtual monoenergetic image volumes and the other uses a tomotherapy linear accelerator to create CT images at megavoltage energies (1.0 MV) of the RF coil. The DECT-based technique reduced artefacts in the images translating to improved μ-maps. The MVCT-based technique provided further improvements in artefact reduction, resulting in artefact free μ-maps. This led to more AC of the breast coil.

In chapter 3, I present a PET-MR-CT motion phantom for QA of motion-correction protocols. This phantom is used to evaluate a clinically available real-time dynamic MR images and a respiratory-triggered PET-MRI protocol. The results show the protocol to perform well under motion conditions. Additionally, the phantom provided a good model for performing QA of respiratory-triggered PET-MRI.

Chapter 4 presents a 4D-PET/MRI technique, using MR sequences and PET acquisition methods currently available on hybrid PET/MRI systems. This technique is validated using the motion phantom presented in chapter 3 with three motion profiles. I conclude that our 4D-PET-MRI technique provides information to characterise tumour respiratory motion while using a clinically available pulse sequence and PET acquisition method.

Keywords

Hybrid Imaging, positron emission tomography (PET), magnetic resonance imaging (MRI), attenuation correction, megavoltage computed tomography (MVCT), dual-energy computed tomography (DECT), quality assurance (QA), respiratory motion, phantom, motion-correction, four dimensional positron emission tomography magnetic resonance imaging (4D-PET/MRI).

Co-Authorship Statement

Chapter 2 of this thesis is adapted from a technical paper submitted to *Medical Physics*, "Technical Note: Comparison of Megavoltage, Dual-energy, and Single-energy CT-based μ-maps for a 4 Channel Breast Coil in PET/MRI" by J.C. Patrick, R.T. Thompson, A. So, J. Butler, D. Faul, R.Z. Stodilka, S. Yartsev, F.S. Prato, and S. Gaede. All authors contributed to the design of the study, the interpretation of the results, and reviewing the manuscript. S.G. was also the principal investigator and oversaw the project. In addition to the above, I performed all off-line data processing, software programming, data analysis, results analysis, and wrote the manuscript.

Chapter 3 is also adapted from an original research article submitted for publication to *The Journal of Nuclear Medicine*. The article is entitled, "Accuracy and Sensitivity of Respiratory-Triggered PET-MRI Evaluated Using a Multi-Modality Motion Phantom", by J.C. Patrick, M.A. Tavallaei, H. Biernaski, R.T. Thompson, R.Z. Stodilka, M. Drangova, S. Gaede. All authors contributed to the interpretation of the results and reviewing the manuscript. In addition to the above contributions, M.A.T. designed and fabricated motion stage used in study and assisted in the experimental set-up. H.B. assisted in the experimental set-up and provided technical assistance with operation of the imaging console. R.Z.S., M.D., and S.G. made significant contributions to the design of the study and S.G. was principal investigator and oversaw the project. I contributed to the design of the study, design and fabrication of phantom, assisted in experimental set-up and operation, data analysis and related programming, and wrote the manuscript.

Chapter 4 is also adapted from an original research article to be submitted for publication. The article is entitled, "Description and evaluation of an amplitude-based 4D-PET/MRI protocol to characterize tumour respiratory motion", by J.C. Patrick, J Thiessen, D. Capaldi, R.T. Thompson, R.Z. Stodilka, M. Drangova, S. Gaede. All authors contributed to the design of the study, the interpretation of the results, and reviewing the manuscript. S.G. was also principal investigator and oversaw the project. Additionally, I performed all off-line data processing and related software programming, analyzed data, and wrote the manuscript.

Acknowledgments

The pursuit of my Ph.D. has been a challenging journey. As with most journeys in life, it is the encouragement and guidance of others that help us overcome the challenges and reach our destination. I am fortunate and very grateful to have been surrounded by people who have provided both forms of support.

First and foremost, I would like to give a heartfelt thanks to my supervisor Dr. Stewart Gaede. Thank you, not only for your expert advice and providing me with opportunities to learn and grow but also for your guidance and words of encouragement in times when I was very discouraged. You have been a mentor and a friend and I am sincerely grateful to have had the opportunity to learn from you in aspects both professional and personal.

I would also like to thank my advisory committee members, Dr. Terry Thompson, Dr. Robert Stodilka, and Dr. Maria Drangova. Thank-you for the many hours you have all taken out of your busy schedules to meet with me. Whether it was to advise on experiment design, my mid-level examination, providing feedback on my thesis, or helping me prepare for my thesis examination, you were always there to provide insightful critiques and input. You have all demonstrated a level of professionalism and compassion that I aspire to emulate.

I would like to extend my gratitude to Dr. Frank Prato for his years of encouragement, and positivity. Regardless of how busy you get, you have always been very generous with your time and invaluable advice. Thank you! I would also like to thank Dr. Aaron Ward for his inspiring lessons in pedagogy. You have forever changed my perspective on the skill of teaching and I hope to continue to learn and improve as I move forward in my career. To Dr. Jerry Battista, thank you for the many insightful discussions. Your ability to find the perfect analogy to make complicated subjects more intuitive has brought clarity to many topics.

None of the work within this thesis could have been possible without the skill and technical knowledge of our PET/MRI medical imaging technologists John Butler and Heather Biernaski. Thank you! I would also like to thank the administrative staff for their help with coordinating meetings and managing finances. Barb Barons, Brenda Dubois, Michele Avon, Shelagh Ross, and Wendy Hough – Thank you for all of the important work you do to keep the departments running smoothly. Additionally, I would like to thank Jeff Kempe for his technical support and stimulating lunchtime discussions over the past few years.

Thank you to Dr. Michael Kovacs and Jeff Corsaut of the Nordal cyclotron and PET radiochemistry facility for providing isotope used in this work. Also, thank you to Dr. David Faul and Dr. Gerald Moran for providing helpful input and technical guidance, in addition to Siemens Canada for supplying the four-channel breast coil and E7 tools software package.

Although not directly involved with my thesis work, Dr. Alex Thomas has played an important role in providing guidance and insight from his many experiences. He has been, and continues to be, a great mentor and friend. Thank you for your advice, many lessons, and planting the idea of graduate school in my head. I look forward to many more 'chin-wags' and scotch-nights.

I would like to thank my lab mates, Matthew Mouawad, Dr. Ilma Xhaferllari, and Dr. Omar El-Sherif. Much like siblings, we seemed to find a good balance of razzing each other while always cheering each other on. We have rejoiced in each other’s successes and we were there to console each other during disappointments. I hope that in the many years to come, that bond will remain strong. Thank you for the many great memories!

To my brother-in-law, Dr. Eric Sabondjian, you have always been a great friend who has been generous with both support and advice. As I have continued to follow down the same career path, you have always been there to offer insight from your experiences. Thank you. You’ll always be a ninja and trailblazer in my books.

To my sister Susan: thank you for always cheering me on, cheering me up, and looking out for me. To my Dad and Annette: thank you for all of your love and encouragement. To my Mom: thank you for your unconditional love, support, and unlimited patience. I love you all!

Lastly, to my wonderful wife Lindsay Patrick, thank you for your love, support, and patience through all of my graduate studies. Words cannot fully express the gratitude and love I have in my heart for you. I can't wait to begin the next chapter of our life together!

Table of Contents

List of Tables

List of Figures

List of Abbreviations

^{176}Lu	^{176}Lutetium
^{18}F	^{18}Fluorine
^{18}F-FDG	^{18}F-Fluorodeoxyglucose
2D	Two-Dimensional
3D	Three-Dimensional
4D	Four-Dimensional
^{68}Ge	^{68}Germanium
A-P	Anterior-Posterior
AC	Attenuation Corrected
APD	Avalanche Photodiode
B_0	Main static magnetic field
BGO	Bismuth Germanium Oxide
Bq	Becquerel
CNR	Contrast-to-Noise Ratio
cps	counts per second
CT	Computed Tomography
DECT	Dual-Energy Computed Tomography
DSCT	Dual-Source Computed Tomography
FBP	Filtered Back-Projection
FoV	Field of View
$G_{Frequency}$	Frequency-encoding gradient
G_{Phase}	Phase-encoding gradient
G_{Slice}	Slice-encoding gradient
HU	Hounsfield Unit
IGRT	Image-Guided Radiation Therapy
iPAT	integrated Parallel Acquisition Technique
IR	Iterative Reconstruction
keV	kilo electron Volt
kV	kilovoltage
LoR	Line of Response

LSO	Lutetium Oxyorthosilicate
MeV	Mega electron Volt
MnCl2·4H2O	Manganese(II) Chloride Tetrahydrate
MRAC	Magnetic Resonance Attenuation Correction
MRI	Magnetic Resonance Imaging
MV	Megavoltage
MVCT	Megavoltage Computed Tomography
NAC	Non-Attenuation Corrected
NaCl	Sodium Chloride
NBAC	Narrow Beam Attenuation Coefficient
NEMA	National Electrical Manufacturers Association
NSCLC	Non-Small Cell Lung Cancer
OP-OSEM	Ordinary-Poisson Ordered Subsets Expectation Maximization
PDF	Probability Distribution Function
PET	Positron Emission Tomography
PMT	Photomultiplier Tube
PROPELLER	Parallel Lines with Enhanced Reconstruction
PTV	Planning Target Volume
PVE	Partial Volume Effect
RF	Radiofrequency
ROI	Region of Interest
RT	Radiation Therapy
S-I	Superior-Inferior
SECT	Single-Energy Computed Tomography
TE	Echo Time
TR	Repetition Time
TrueFISP	True Fast Imaging with Steady-state Precession
TSE	Turbo Spin Echo
TurboFLASH	Turbo Fast Low Angle Shot
VIBE	Volumetric Interpolated Breath-hold Examination
VOI	Volume of Interest
Z	Atomic Number

γ	Gyromagnetic ratio
γ_{Co-60}	Cobalt-60 gamma photon
μ	Linear attenuation coefficient
ω	Larmor frequency
ω_{Slice}	Slice precession frequency

Chapter 1

1 Introduction

The effectiveness of cancer treatment is increasingly dependent on imaging for diagnosis, intervention planning, and assessment of treatment response. Among the modalities commonly used for intervention planning, X-ray Computed Tomography (CT) is the standard of care and the basis from which nearly all radiotherapy treatments are planned. Complementary to CT, which provides detailed anatomical information about therapy targets and surrounding tissues, Positron Emission Tomography (PET) can provide biological information through the visualization of radiotracer distribution within the patient. The hybridization of these two modalities as PET-CT has not only become a powerful tool in cancer detection but also allows for improved target volume definition when used in radiotherapy planning. Magnetic Resonance Imaging (MRI) has also been increasingly used in radiotherapy treatment planning due to its superior soft-tissue contrast, and in recent years, its hybridization with PET has attracted the attention of the radiation oncology community. As with most new technologies, work with PET-MRI is an ongoing area of research in an effort to improve, and expand its applications. This thesis examines several methods to improve the utility of PET-MRI for radiotherapy treatment planning applications. The work herein includes a description and comparison of CT-based techniques to correct PET signal attenuation due to the presence of MRI radiofrequency coils, the development of a PET/MRI/CT-compatible tumour respiratory motion phantom for use in quality assurance and/or development of protocols designed to correct or characterize respiratory motion, and lastly, the description and evaluation of a four-dimensional (4D) PET-MRI technique for the characterization of tumour motion that can complement 4D-CT based radiation treatment planning. In this first chapter, I will discuss the principles of each imaging modality used in subsequent chapters, some of the challenges associated with the hybridization of those modalities including issues related to attenuation correction, investigate various techniques used to mitigate the effects of motion during imaging, techniques used to characterize motion, and provide some motivation behind this work. Finally, I will provide an overview of the thesis itself.

1.1 Computed Tomography Principles

X-ray computed tomography (CT) is a non-invasive high-resolution anatomic imaging modality that has been commonly used for clinical diagnostic purposes since the early 1970's. Today it is among the most important imaging technologies for both oncologic diagnosis and intervention planning. In a technique described by Hounsfield in 1972, and later by Ambrose in 1973, a CT scanner uses a rotating x-ray source to take attenuation measurements over a large number of angles to reconstruct a two-dimensional (2D) cross-sectional image, usually in the transverse plane.[1,2] The CT scanner acquires many of these image sections of a patient, usually in the longitudinal direction, to construct a three-dimensional (3D) image volume of the patient's internal organs. Comprehensive technical descriptions of CT scanners can be found in various scientific publications and textbooks.[3,4]

1.1.1 CT Artefacts and Reduction Techniques

In general terms, an image artefact is any feature within an image that is not present in that actual subject being imaged. In CT, there are many different sources of artefacts, all of which may mimic or obscure pathology. Fortunately, the mechanisms behind these artefacts have been studied and methods for avoidance and reduction can be taken to ensure good quality images. The majority of CT artefacts can be grouped into one of four categories, based on their source: Hardware-based, reconstruction-based, patient-based, and physics-based. The next four sub-sections will describe the various artefacts that can be derived from these sources, the mechanisms behind each of these, and strategies designed to avoid or reduce their presence in images.

1.1.1.1 Hardware-based Artefacts

Ring artefacts are characterized by rings of dark or bright voxels centered on the point of rotation of the CT gantry. This is caused by a defective or uncalibrated detector on a third generation scanner and is more likely to be visible through a uniform medium like air or a uniform phantom. Although ring artefacts are less visible against the heterogeneity of clinical scans, their presence is more likely to negatively impact the diagnostic quality of the image rather than be mistaken for disease (Figure 1-1). These artefacts can be avoided with a calibration scan and adjusting the detector gain to match the other detectors. In the case where calibrations fail, repairing or replacing the faulty detector should solve the problem.

Figure 1-1: Ring artefact in a pelvic CT. Image was adapted from Boas *et al*. (2012).[5]

1.1.1.2 Reconstruction-based Artefacts

In a helical CT scan, the reconstruction process involves a helical interpolation. In a single-row detector system, when a high contrast edge falls between two acquired image slices, the reconstruction algorithm alternates between measurements from a single acquired row and interpolated values between two acquired rows all while the table is advancing during the scan. Some projection angles have greater contributions from the high-density feature, while other angles have more contributions from the low-density feature. This results in alternating light and dark bands radiating outwards from the center of the transverse image. If you are to scroll through the image slices, these bands will appear to rotate, giving them their name ‘windmill artefacts’. In a multi-row detector CT, this interpolation process can complicate windmill artefacts even further. This is because there is now the potential for several detector rows to fall on that high contrast edge during gantry rotation. A higher scan pitch results in more radial bands because more detector rows cross the high contrast edge during a rotation. Therefore, lowering the pitch, using a 180-degree versus a 360-degree interpolation, or using thinner acquisition slices can minimize windmill artefacts.

Cone beam artefacts are also reconstruction-based. As the number of detector rows acquiring data during a scan increases, as in the case of cone beam, wider collimation is required. However, the collected data is no longer contained within a flat plane. Instead, it is contained within the intersecting volume between cones. Features located further from the central axis experience artefacts that are similar to partial volume. This increases in detectors located in the outer rows, where x-rays detected correspond less with their planar location. Although reconstructions will require more time, using appropriate multi-row detector geometry within a specific cone beam reconstruction strategy, rather than a standard reconstruction technique, can reduce resulting artefacts.

Stair step artefacts appear as serrations at the edges of structures on coronal or sagittal CT images. Although less severe in helical scans, stair step artefacts can occur in multi-row and 3D reformatted images within non-overlapping reconstruction intervals of scans using wide collimators. Today’s multi-row CTs have greatly reduced stair step artefacts due to the thinner sections of data that are acquired.

Another artefact that can result from the helical interpolation process is zebra artefact. This appears as faint alternating stripes of more or less noise along the z-direction of the image and is more pronounced along the outer portions of the image as you move away from the rotation axis of the CT. Again, this type of artefact can be reduced with thinner sectioned data acquisition. Figure 1-2 highlights the various types of CT reconstruction-based artefacts.

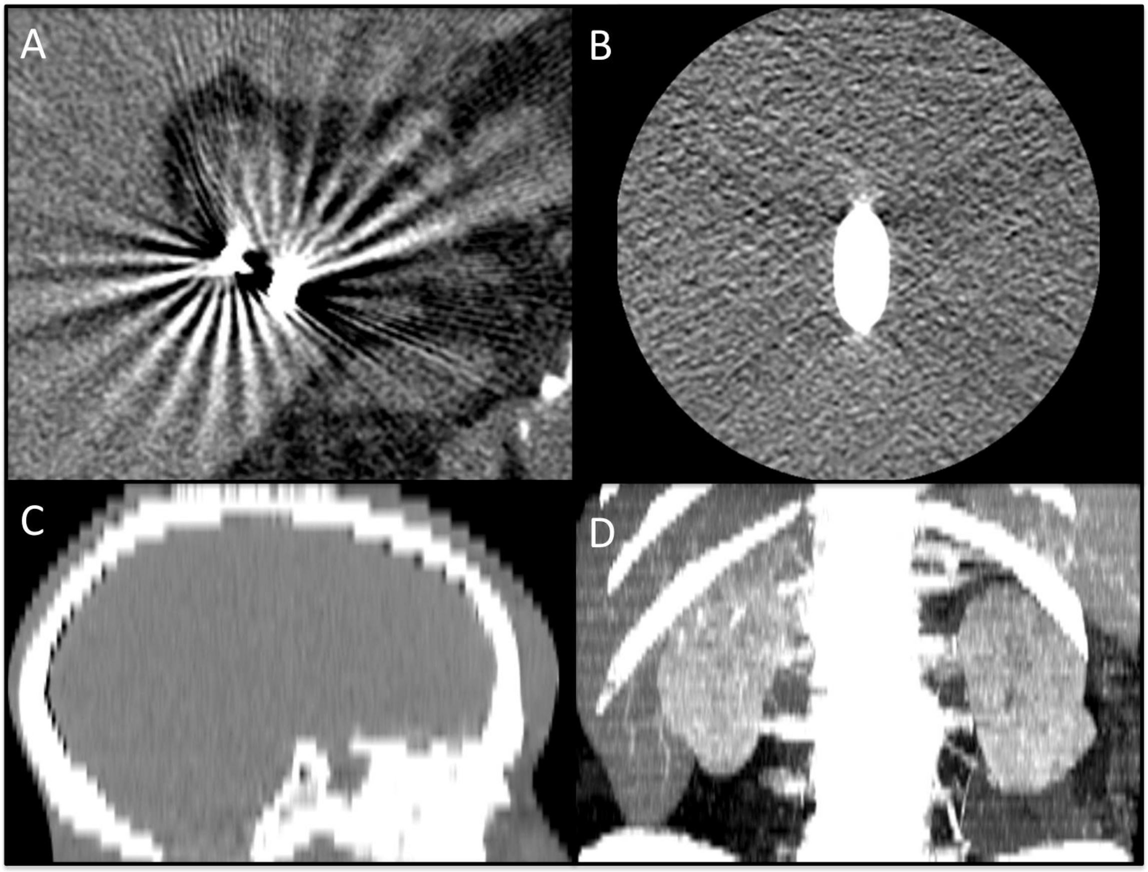

Figure 1-2: Reconstruction-based artefacts. A) Windmill artefact streaks around cholecystectomy clips. Image adapted from Boas *et al.* (2012),[5] B) Cone beam artefacts shown around a Teflon rod positioned with a 70 mm offset form scanner isocenter, C) Stair step artefact in a sagittal reformatted image from an axial CT with 5 mm collimation and reconstruction interval, D) Zebra artefacts shown in a maximum intensity projection image from a thoracic helical CT. Images for B-D adapted from Barrett *et al.* (2004).[6]

1.1.1.3 Patient-based Artefacts

Incomplete projections cause shading or streaking artefacts across the transverse plane of CT images. This patient-based artefact happens when part of the patient lies outside of the scanner's field of view (FoV). Incomplete projections can also be caused by highly attenuating items such as equipment coming in between the beam and detectors of the CT during a scan. Although this can be resolved by ensuring that no patient parts lay outside the FoV or equipment lay in the beam's path, some scanners are able to detect inconsistencies in reference data channels to avoid using suspicious reference data. Some systems are also designed with reference detectors on the tube side (or ray path within the gantry) to eliminate any interference with reference data.[6]

Patient motion is another potential source of artefact in CT. Some patient motion can be avoided through shortened scan times, immobilization devices, and in some cases sedation. However, some motion is involuntary and cannot be avoided during a scan. This results in slice misregistration artefacts appearing as streaks or shading throughout the image. Some CT scanners have built-in motion artefact reduction features. Some of these features involve either scanning more than 360 degrees of a bed position or excluding some of the CT projections from the reconstruction to either average out the motion or exclude projections with the maximum discrepancy respectively. Some systems also make use of gating to capture a single phase of the cardiac or respiratory cycle. I will explore more of these motion management methods in the context of radiotherapy planning in section 1.5.1.1. Figure 1-3 highlights examples of patient-based CT artefacts.

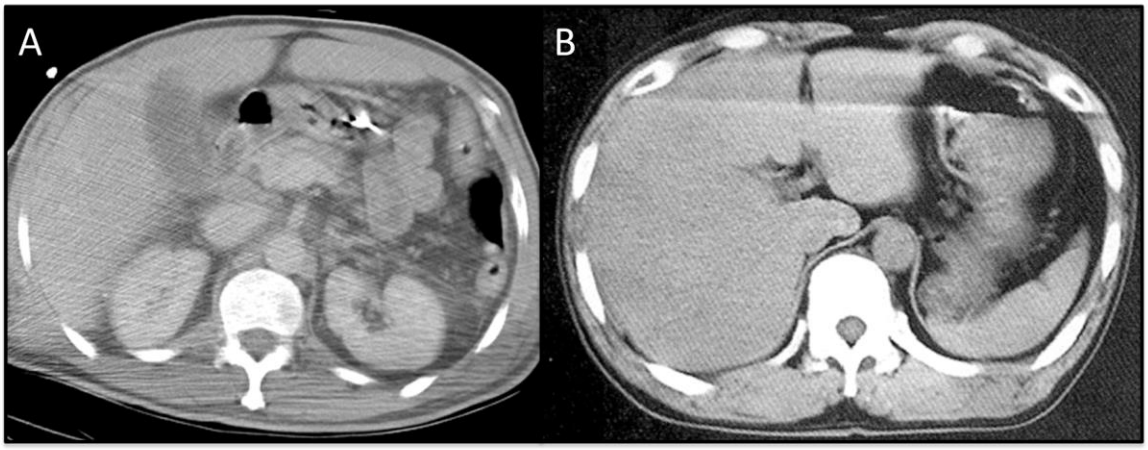

Figure 1-3: Patient-based artefacts. A) Streaking artefact in CT from incomplete projections caused by patient's arms being placed at their side but outside the FoV. B) Motion artefact caused by respiration during CT scan. Images adapted from Barrett *et al.* (2004).[6]

It is not uncommon for a patient to have metal on or inside of them. Whether in the form of an aneurism clip, artificial joint or dental implant, metal produces artefacts in CT images that appear as bright and dark streaks projecting outward from the metal object. This is caused by the metal's density, which lay outside of the normal range that the CT system was designed to calculate. In some cases, metal can be removed from the FoV, and some scanners are equipped with metal artefact reduction software.[7] This software may reduce or remove the streaks associated with metal but often at the cost of losing detail locally. Even though metal artefacts can often be considered a patient-based problem, the mechanisms by which they occur are physics-based. I examine some of these mechanisms of metal artefact in more detail in the following section, 1.1.1.4.

1.1.1.4 Physics-based Artefacts

Aside from the averaging of CT number values of materials within a single voxel, partial volume effect can result in shading artefacts caused by inconsistencies between detector views. This happens when an object lies within the beam at one point of rotation, but outside of the beam at the opposite point of rotation. Fortunately, this type of artefact can be avoided by acquiring with thin acquisition sections.

Photon starvation occurs in highly attenuating regions within a patient's body or with certain dense materials. The inadequate number of photons making their way through the object to the detectors causes noisy projections, making streaks in the images. Increasing the tube current can minimize this particular artefact. However, a consequence of increasing tube current is an increased patient dose from the x-ray beam. To avoid increasing current, some CTs are capable of automatically varying the tube current in a process called milliamperage modulation. Another method to reduce artefacts from photon starvation is through adaptive filtration. Here software is used to smooth attenuation profiles in areas that are highly attenuated prior to image reconstruction.

Another physics-based artefact can result from undersampling. This can happen when intervals between projections are too large, causing view aliasing appearing as thin stripes projecting at a distance from the object. Undersampling can also cause ray aliasing, which appears as stripes that are close to the object being imaged. View aliasing can be resolved by increasing the number of projections per rotation and ray aliasing can be resolved by increasing resolution through methods like quarter-detector shift or flying focal spot. Figure 1-4 highlights streaking artefacts and aliasing in CT.

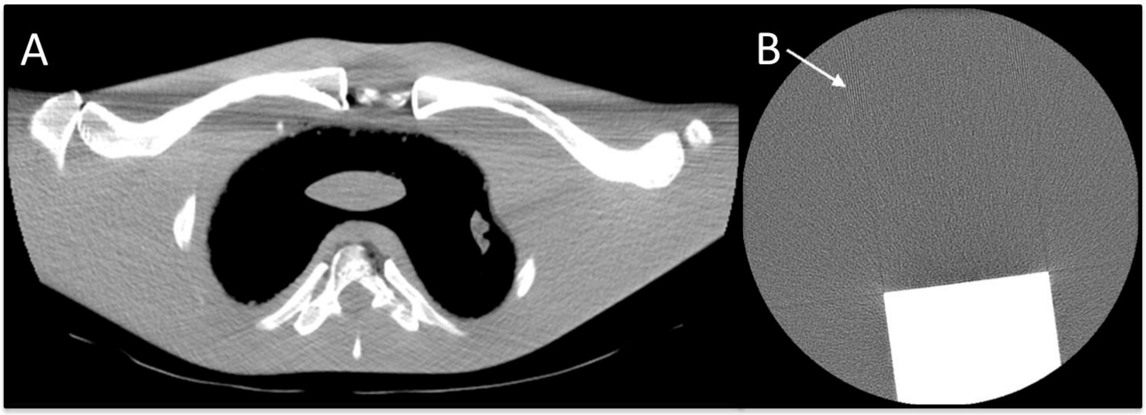

Figure 1-4: A) Streaking artefacts caused by photon starvation in CT of shoulder phantom, B) Arrow pointing to aliasing caused by undersampling in CT of Teflon block phantom in water. Images adapted from Barrett *et al.* (2004).[6]

The final type of physics-based artefact I will discuss happens as a beam passes through a medium and lower energy photons are absorbed more readily than higher energy photons. This causes the mean beam energy to increase, in other words get ‘harder’. This causes cupping artefacts and/or dark streaks to appear to be projecting from dense objects, which can be seen in Figure 1-5. Cupping can occur in objects with rounded cross-sectional profiles. The edge of the object will often have a higher CT number than the middle of the object, even when it may be composed of homogenous material. This is now typically corrected with a simple beam hardening correction, commonly built into current CT systems. Streaking artefacts from beam hardening can occur in bone, contrast medium, or in other highly attenuating materials. This can be improved with the use of filtration, calibration correction, or beam hardening correction software. Filtration is used to harden the beam prior to it passing through the object of interest. This is often accomplished with a metallic filter. Bow tie filters can also be used to harden just the edges of a beam, which pass through the thinner anatomy of a patient. Calibration correction is used to determine an appropriate compensation for anatomy specific scans. Beam hardening correction software uses an iterative approach to reduce dark bands and blurring in soft-tissue/bone interfaces. This is primarily used when imaging bony anatomy. However, the above strategies are often insufficient when attempting to correct for materials with much higher electron densities like metals. One method to reduce the effects of beam hardening from materials with densities greater than bone is by scanning with two different energy spectra, using a dual energy CT (DECT) scanner. Information taken from the two energy spectra can be used to calculate virtual monochromatic images of the subject, which have substantially reduced beam-hardening artefacts. Another method of reducing the effects of beam hardening from materials with densities greater than bone is to make the beam itself harder, or in other words, scan at higher energies. These higher energy photons are less likely to be absorbed by high atomic number objects, resulting in reduced artefacts. A third method to reduce streaking artefacts in CT, caused by high-density materials is iterative reconstruction. I explore both DECT and imaging with higher energy x-rays in the following two sections, followed by a very brief section on the use of iterative reconstruction techniques for metal artefact reduction in CT.

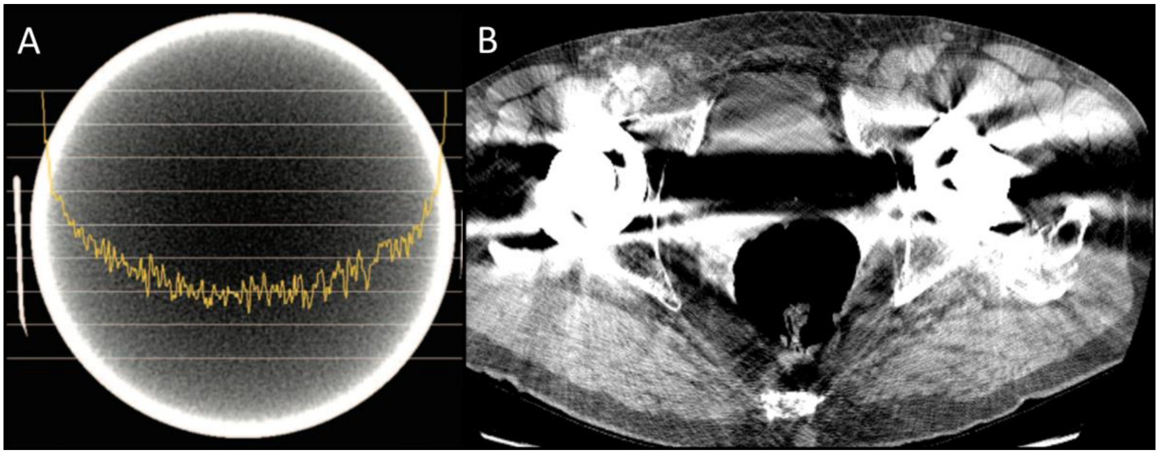

Figure 1-5: Physics-based artefacts. A) Cupping artefact due to beam hardening in CT image of cylindrical uniform water phantom. Adapted from Barrett *et al.* (2004),[6] B) Streaking due to beam hardening in CT image of hip replacements. Adapted from Boas *et al.* (2012).[5]

1.1.2 Dual-energy Computed Tomography (DECT)

DECT uses two different photon energy spectra, each composed of a bremsstrahlung spectra and characteristic peaks of target materials, with maximum photon energy being determined by the x-ray tube voltage. Although dual-energy images can be acquired sequentially, by either taking two separate helical scans at different voltages or single rotations at alternating tube voltages, several manufacturers have taken various design approaches to achieving DECT in a timelier and less motion artefact prone way. Some systems use a single x-ray tube and achieve two different energy spectra by quickly switching between low and high voltages.[8-10] Another approach often referred to as dual-source CT (DSCT), involves a CT gantry equipped with two detector arrays and two x-ray tubes operating at two different voltages.[11,12] To minimize the amount of spectral overlap when using standard x-ray tubes, 80 and 140 keV are the most commonly used energies in DECT. In DSCT scanners, this spectral overlap can be further minimized with the use of tin filters. Figure 1-6 characterizes DECT and DSCT.

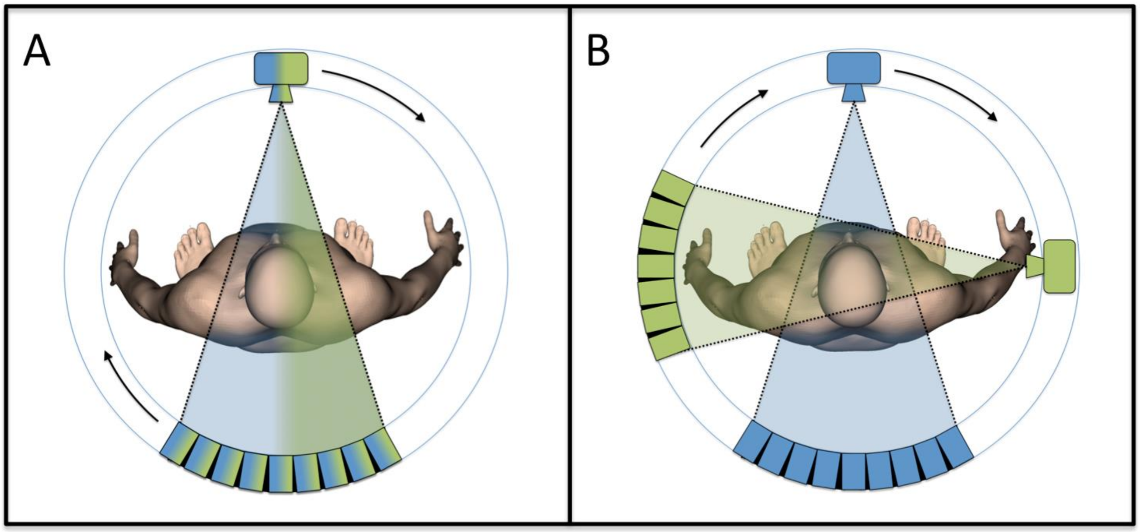

Figure 1-6: Dual-energy CT source configurations. A) Single tube configurations rapidly switch between low and high voltages, B) Dual-source CT configurations use two separate x-ray tubes, operating at different voltages to achieve dual-energy imaging.[13]

Data acquired at two different tube potentials allows us to extract various forms of spectral information, depending on the type of post-processing used. The most common approach is to first reconstruct the CT images from each energy dataset. Spectral information can then be extracted based on differences calculated from the two image sets. There are mainly three types of information that are extracted with these image-based algorithms: material differentiation, material quantification, and image optimization.

Algorithms used to differentiate specific materials like calcium and magnesium from uric-acid, as in the case of locating kidney stones, are based on the photoelectric effect within specific density ranges. Here, a slope is defined between density values at each spectra and a different colour is assigned to either side of the slope.[14-16]

Quantifying a substance, such as contrast medium, within an image volume can also be calculated. This can be achieved using an algorithm called ‘three material decomposition’. Density measurements can be interpreted as a value’s displacement from normal tissue densities in relation to values defined by the photoelectric effect of the contrast material used.[17-19]

The third type of post-processing algorithm is used for image optimization. One type of image optimization is called nonlinear blending. This algorithm creates an optimum contrast image by combining high iodine contrast with low noise.[20] Another image optimization algorithm is able to calculate virtual monoenergetic image volumes from the manipulation of either projection data[21] or image data[22] from each of the two energy spectrums. This technique is particularly useful for reducing beam-hardening artefacts in images containing materials with higher electron densities like iodinated contrast agents.[23]

1.1.3 Megavoltage Computed Tomography (MVCT)

As mentioned previously, one method of reducing CT artefacts produced from high-density materials is to make the beam itself harder, or in other words increase the average energy of the x-ray beam. Work by Schreiner *et al.* shows that higher energy photons emitted from Cobalt-60 source (γ_{Co-60} = 1.25 MeV) and a linear accelerator (linac) (mean x-ray = 1.3 MeV) are not as susceptible to absorption through photoelectric effect. Instead, photons at megavoltage energies are more likely to interact with high-density material through Compton scattering, providing better photon penetration. This results in images that are less artefact prone than images produced in the kilovoltage energy range.[24] It was also noted that MVCT images show a linear relationship between the Hounsfield values of the imaging volumes and the electron densities of the corresponding materials in those volumes (Figure 1-7).[25]

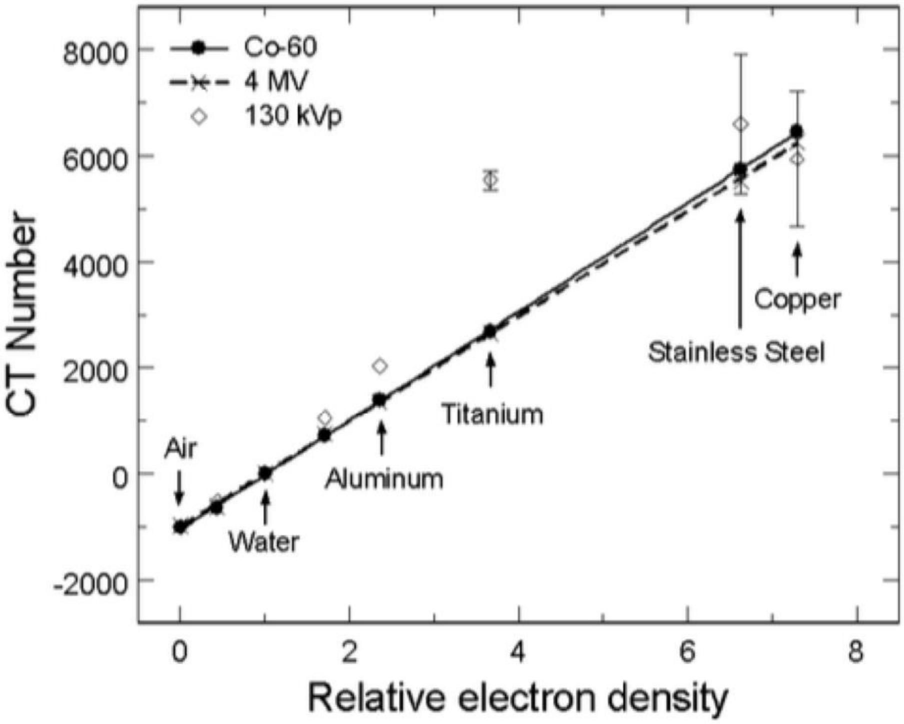

Figure 1-7: Plot showing linear relationship between the electron densities of various high-density materials and their respective CT numbers from MVCT images. Adapted from Rogers *et al.* (2005).[25]

A helical tomotherapy unit (Accuray Inc., Sunnyvale, CA) has a 6 MV linac mounted opposite to a detector array, on a ring gantry. The ring gantry assembly rotates continuously while the patient couch translates through the gantry. Work done by Yartsev *et al.* shows how this same unit can be used for the acquisition of MVCT images with the linac detuned, reducing its mean energy to 1.0 MeV.[26]

1.1.4 Iterative Reconstruction (IR) for CT Metal Artefact Reduction

High-density materials, such as metals, cause a lack of projection data due to high photon absorption, particularly of the lower energy photons in the x-ray spectrum.[27-30] This produces a corrupted sinogram, which is missing data. The common CT reconstruction technique is an analytical algorithm called filtered back-projection (FBP). FBP is not designed to account for these inconsistencies in the data. Several algorithms have been proposed to reduce these streaking artefacts caused by metal, and have had limited success.[27-31] These methods attempt to repair the corrupted sinogram data through replacing with intact data or a linear interpolation through the corrupt region.

Interestingly, iterative reconstruction (IR) algorithms have been around for many years in CT but due to the higher computational demands of IR compared to analytical methods like FBP, were abandoned when the volume of data increased. More recently, the availability of powerful computing resources has helped bring about renewed interest in IR techniques for quality improvement of CT images,[32-34] dose reduction, and artefact reduction.[35,36] IR techniques inherently perform better at metal artefact reduction than analytical techniques because IR methods approach a solution to fit the data that was measured, whereas FBP assumes the measured data is complete and exact. This assumption cannot be made when imaging in the presence of metal. However, due to limited clinical availability, IR is seldom used.

1.2 MRI Principles

Despite the widely adopted applications of CT, MRI provides much greater soft-tissue contrast. MRI allows tissues to be imaged with a wide variety of contrast mechanisms, from both endogenous tissue properties and exogenous contrast mediums. Figure 1-8 highlights the superior soft-tissue contrast of MRI over CT, using three different contrast mechanisms. The differences in CT and MR images arise from the different contrast mechanisms they use. Where CT images are based solely on electron densities, MR images are based on subtle changes in magnetic relaxation within tissues. More specifically, MRI most often relies on the signal derived from hydrogen nuclei (protons) within tissues as they interact with magnetic fields and radiofrequency (RF) pulses. The basic principles of how these interactions are used to create images are discussed in the subsequent six sections.

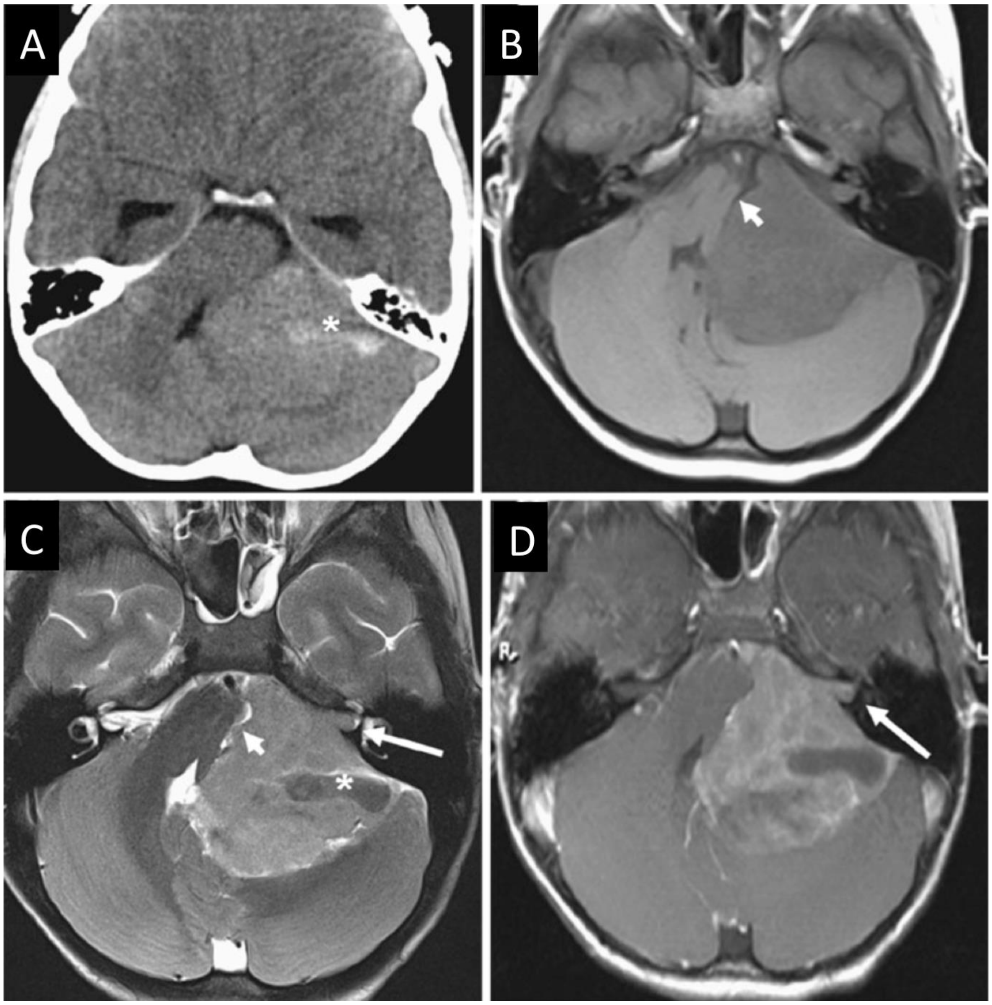

Figure 1-8: Axial images of an anaplastic medulloblastoma in A) noncontrast CT, B) T2-weighted MRI, C) T1-weighted MRI, and D) contrast-enhanced T1-weighted MRI. Adapted from Eran *et al.* (2010).[37]

1.2.1 Magnetic Moment

Hydrogen protons are frequently used as the basis for MR images because of their abundance in tissues and their strong magnetic moment. For simplicity, I will describe the motion of these magnetic moments using classical mechanics. The strong magnetic moment is due to the spin of this positively charged particle, the proton. The strength of a proton's magnetic moment is proportional to its angular momentum as it spins around an internal axis. At this level, each proton acts like a very small magnetic bar with a north and south-pole. Ordinarily, the magnetic moments of protons in tissues are oriented in random directions. The result is no net magnetization. However, when a strong external magnetic field is applied the protons will begin to precess about the direction of the applied external magnetic field in either a parallel or antiparallel state. These states only refer to the longitudinal components of a proton's magnetic moment and the relative proportion of each state is dependent upon the magnitude of the applied external magnetic field. The Larmor frequency, or in other words the frequency with which the protons precess is directly proportional to the strength of the external magnetic field according to the equation,

$$\omega = \gamma \mathrm{B}_0, \tag{1}$$

where γ is the gyromagnetic ratio, which is equal to 42.576 MHz/Tesla for hydrogen protons, and B_0 is the strength of the external magnetic field. Thus, in a 3 Tesla magnetic field the precession frequency of hydrogen protons will be $\approx$ 128 MHz.

The total magnetization from all proton magnetic moments within tissues can be represented as a simple vector that has only a net longitudinal component.

1.2.2 Radiofrequency Pulses and Magnetization

The detection of MRI signal is made possible by exploiting the resonant absorption and dissipation of energy. The resonant absorption of energy is achieved through the transmission of RF electromagnetic field pulses or *excitation pulses*. The frequency of this RF field pulse must be identical to the precession frequency of the protons, which is calculated using the Larmor formula, shown as equation 1 in section 1.2.1. The RF field causes the net magnetization to rotate into the transverse plane and away from the longitudinal direction of the main external magnetic field. The strength and duration of the RF field pulse will determine the amount of rotation, or *flip angle*, of the net magnetization.

1.2.3 Detection of MR Signal

This transverse component of the magnetic precession is responsible for the detectable signal, which is captured by the MRI receiver coils. The MRI receiver coils are essentially a pair of electrically conductive loops that are placed within close proximity to the patient and behave as the ‘antenna’ of the MRI system. A voltage is induced in the receiver coils as the protons in the patient’s tissues relax from their transverse magnetization back to their equilibrium state along the direction of the main magnetic field.

1.2.4 MR Relaxation

The equilibrium state of protons while in the main magnetic field has only a net longitudinal component. In this state, the net transverse component is equal to zero. When the RF pulse is applied, the energy added to the protons’ spin states pushes it out of equilibrium, increasing the transverse component of magnetization. When the RF pulse is stopped, their spins relax back to their equilibrium state through the gradual decay of the transverse component. MR relaxation is the combination of two different mechanisms, the recovery of the longitudinal magnetization (T_1) and the decay of the transverse magnetization (T_2) caused by the dephasing of spins. These T_1- and T_2-relaxation times differ between tissues types, both healthy and diseased. It is these differences that form the basis for contrast in MR images.

1.2.5 Image Acquisition and Spatial-encoding

As mentioned in section 1.2.2, the resonant absorption of energy is achieved through the transmission of RF pulses at a frequency that is equal to the precession frequency of the protons in the subject being imaged. When a patient is placed within the main magnetic field, every proton within the patient’s tissues that lay within the MRI’s field of view has the same precession frequency. As such, there is no spatial information about the signals being received during the protons’ relaxation.

Gradient coils are used to spatially-encode these signals through the application of time and spatially varying magnetic fields in addition to the already present static main magnetic field (Figure 1-9). The dynamic application of these spatially varying magnetic fields is made possible by three sets of gradient coils, each corresponding to one of the main orthogonal directions. Gradient coils are designed to produce a linear spatial variation of the magnetic field, which in turn creates spatial variation of resonant frequencies. Each of the magnetic field gradients is positioned such that there is no additional contribution to the main field at the isocenter (x=0, y=0, z=0). Here, the x-axis represents the left/right direction, y-axis the anterior/posterior direction, and z-axis the superior/inferior direction. Gradient coils and the magnetic field gradients they create help to facilitate the three major processes of forming an image dataset. These processes are slice selection, phase-encoding, and frequency-encoding.

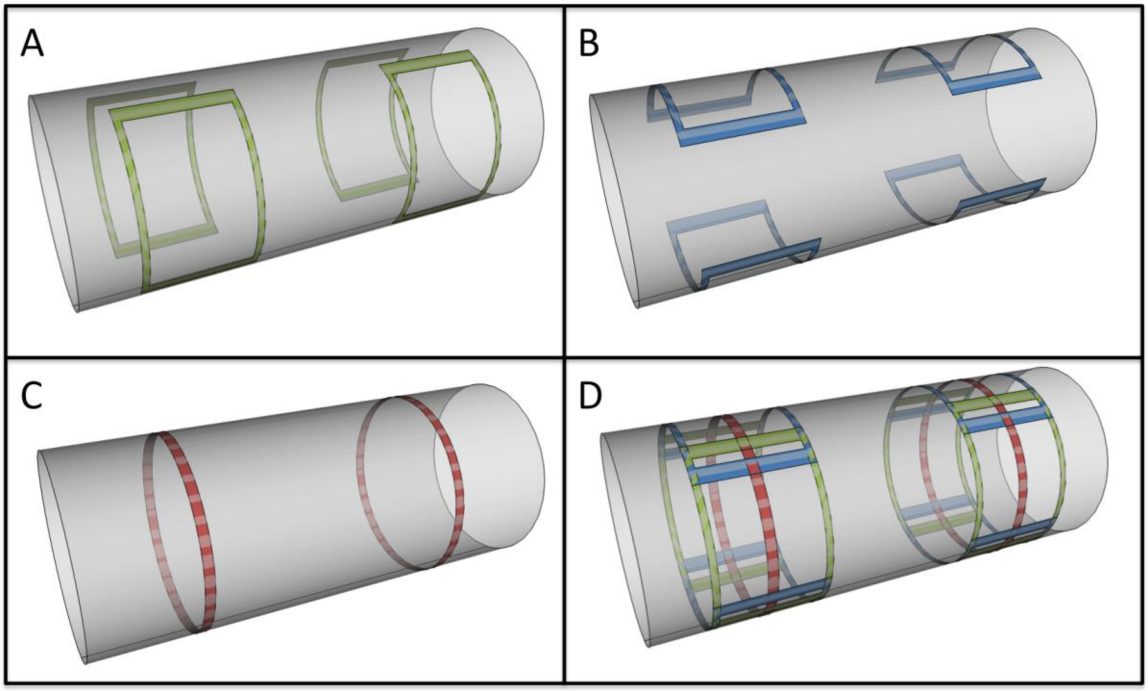

Figure 1-9: Simplified configuration of gradient coils for the three main orthogonal directions, A) x-gradient coils, B) y-gradient coils, C) z-gradient coils, and D) all three sets of coils.

Slice selection is the process of selectively exciting protons that lie within a desired slice of a sample/patient. Selective excitation is achieved by applying a gradient magnetic field orthogonal to the desired slice. At the same time, the excitation pulse is applied with a frequency that matches the precession frequency of the protons in the desired slice. The precession frequency of this slice (ω_{Slice}) is given by:

$$\omega_{Slice} = \gamma(B_0 + zG_{Slice}) \, , \tag{2}$$

where G_{Slice} is the strength of the gradient magnetic field at the position z of our slice. Within this slice, the two remaining spatial axes can be encoded by using phase-encoding and frequency-encoding.

The process of phase-encoding requires the application of a second linear gradient magnetic field along one of the two remaining directions within the slice plane after the excitation pulse. This phase-encoding gradient (G_{Phase}) is applied only briefly, causing a spatially dependent phase shift along the direction of the applied gradient. A different intensity phase-encoding gradient must be applied after each excitation pulse and a separate excitation pulse must be applied for each row of voxels in the phase-encoding direction. To ensure an adequate amount of longitudinal relaxation occurs between excitation pulses, a delay called the repetition time (TR) is included. The TR multiplied by the number of phase-encoding steps defines the total time needed to acquire an image.

The final spatial dimension is encoded by applying a third linear gradient magnetic field while acquiring data. Similar to how the slice selection gradient creates a spatially dependent variation of proton precession frequencies during excitation, the frequency-encoding gradient ($G_{Frequency}$) creates a spatially dependent variation of proton precession frequencies in the frequency-encode direction while receiving the RF signal.

A simple pulse diagram of a gradient echo sequence shows each of the above-described events in relation to each other over time (Figure 1-10). The sequence of RF excitation pulses and magnetic field gradients combine to produce an image where each voxel can be characterized by a specific phase and frequency within the selectively excited sample/patient slice.

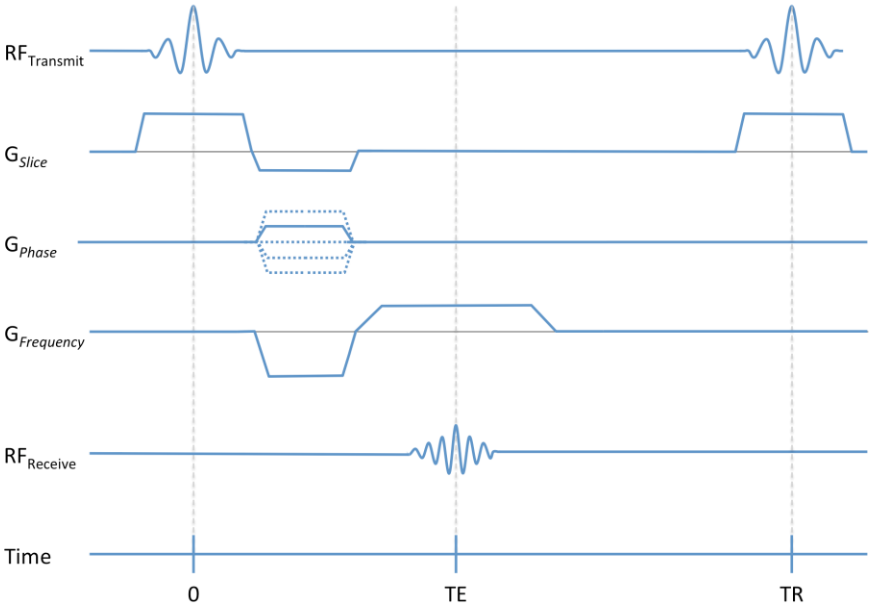

Figure 1-10: A gradient echo pulse sequence diagram. The horizontal axis shows the timing of basic hardware activity as they are incorporated into the pulse sequence.

To reconstruct a 2D image from of the selected slice, a Fourier transform is used to convert the frequency-encoded data into frequency projects. Those frequency projections are then converted into the final 2D image by applying second Fourier transform.

1.3 PET Principles

Positron emission tomography (PET) is a nuclear medicine, molecular imaging technique used to track and quantify the distribution of molecular processes in the body. This is achieved by injecting a positron-emitting radioactive tracer into a patient. Tracers are often designed to have specific biological interactions, which influence the distribution of the tracer throughout the body. For example, ^{18}F-fluorodeoxyglucose (^{18}F-FDG) is a tracer in the form of a glucose analogue. ^{18}F-FDG can be used to image the distribution of tissue metabolism throughout a patient’s body based on its correlation with glucose uptake. This tracer is most commonly used for cancer imaging. The hypermetabolic properties of cancer cells cause ^{18}F-FDG to accumulate in tumours. The positrons emitted from PET tracers annihilate with electrons within the patient’s tissues. Each of these annihilations results in the emission of two 511 keV gamma-photons in opposing directions and it is these gamma-photons that are detected by the PET scanner.[38] One of the main strengths of PET is its sensitivity. Although PET typically measures radiotracers in nanomolar concentrations, it is possible to measure radiotracers present in picomoles.[39]

A PET scanner has detector blocks that are designed to detect these 511keV photons. Each detector block consists of an inorganic scintillator crystal attached to an array of photomultiplier tubes (PMTs). Circular arrays or axially stacked rings of detector blocks within the PET scanner face inwards to surround an imaging volume (see Figure 1-11).

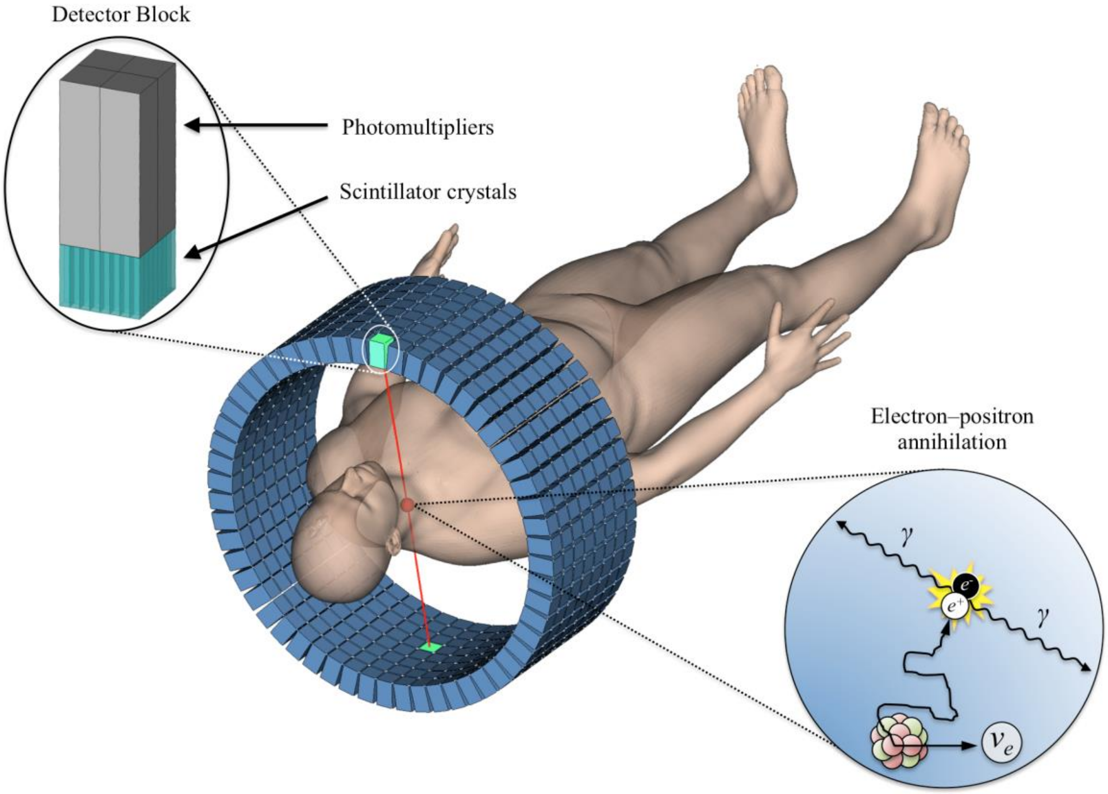

Figure 1-11: A typical arrangement of detector blocks in a PET scanner. Inset upper left corner, is an example of a detector block configuration with scintillator crystal and PMTs. Inset bottom right corner, shows the beta+ decay of a radioactive isotope, the path of the emitted positron, and its annihilation with an electron, which results in the emission of two gamma photons.

The scintillator crystal of the detector block absorbs the gamma-photons and through the photoelectric process converts them in an optical fluorescent signal. This signal can then be detected by the PMT and translated into an electrical signal. Prior to the 1990's, a commonly used scintillator was Bismuth Germanium Oxide (BGO) due to its good characteristics for 511 keV gamma-photon detection. However, the superior count rate capability of lutetium oxyorthosilicate (LSO) has made it the scintillator of choice today, despite it featuring a decay of natural ^{176}Lu itself.

A square array of PMTs is attached to the back of the scintillator crystal. A PMT is a vacuum tube, containing a photocathode, a series of dynodes, and an anode. It allows weak light signals in the ultraviolet to near-infrared range to be detected. When gamma-photons strike the scintillator crystal, all PMTs simultaneously detect the same flash of light to varying degrees, depending on their position relative to the individual event. The photons emitted from the scintillator strike the photocathode in each of the PMTs. When this happens the photocathode ejects electrons. These electrons are multiplied millions of times through series of dynodes, allowing for the detection of even individual photons. The arrangement of PMTs of the detector block in combination with accompanying circuitry, allows the system to locate what region of the scintillator absorbed the photon by detecting the relative amount of light sensed by the array.

Based on the knowledge that PET radiotracer annihilations simultaneously emit two 511 keV photons in opposite directions, a PET scanner uses information from gamma-photons detected in near time-coincidence (using a typical temporal window of 6 to 12 nanoseconds, and as low as 400 picoseconds for '*time-of-flight'* capable systems[40-42]). If two detected events are registered as coincident, it is then possible to locate the annihilation event from which they originated as lying somewhere along a line joining the detected events. This line joining detected events is called a line-of-response (LoR). When the LoR correctly represents the paths of the annihilation photons, and thus the location of the annihilation event, the detected event is called a 'true coincidence' event (see Figure 1-12). A 3D image of radiotracer distribution inside a patient can be calculated by measuring hundreds of thousands of detected events along different LoRs.

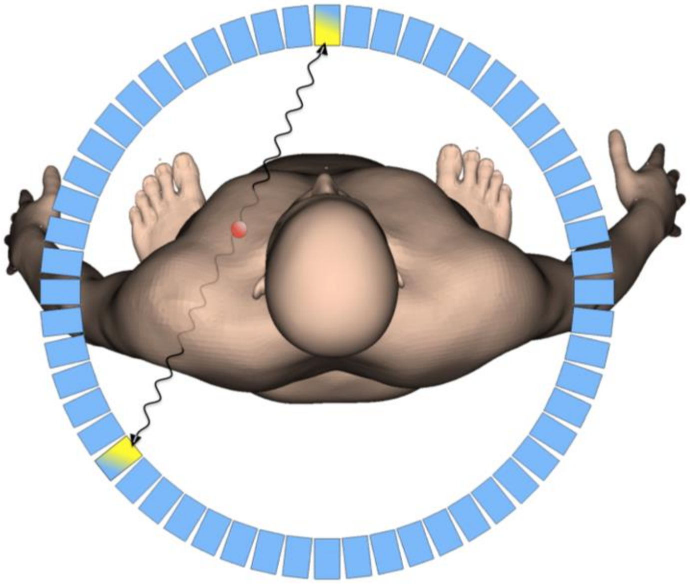

Figure 1-12: A 'true' coincidence event. The line-of-response connecting the two coincidence events correctly reflects the location of the positron annihilation.[13]

1.3.1 Quantitative Errors and Correction Techniques

Quantitative measurement of radiotracer distribution in PET imaging is not trivial, as the physical processes of photon scatter and attenuation, must be factored into the calculation of spatial location and even the detection of events. Additionally, the PET scanner has limitations in terms of photon count rate capabilities, and determining the location of detected events. Each of these processes and limitations must be accounted for during image reconstruction, and in the following sections I will discuss how this is accomplished through the use of detector normalization, and corrections for dead time, random and scattered coincidences, as well as the attenuation gamma-photons.

1.3.1.1 Normalization

The efficiency of gamma-photon conversion into an electrical signal can vary from one block detector to another. Small variations in scintillator crystal dimensions and differences in the quality of their optical coupling to the array of PMTs can cause these differences in efficiency, leading to variations in resolution and sensitivity throughout the FoV. We can account for these variations by recording the number of counts detected by each detector pair after uniform exposure to a radionuclide source, and then applying corrections to the projection data before proceeding to tomographic reconstruction. This process is called normalization.

Although all detector pairs are exposed to the same number of coincidence gamma-photons, some will record more counts than others. This can be accounted for by calculating the normalization factor (NF) for each detector pair (a, b) using,

$$NF_{(a,b)} = nCount_{(a,b)}/AvgCount, \tag{3}$$

where $nCount_{(a,b)}$ is the number of coincidence events counted by detector pair a and b, and $AvgCount$ is the average counts for all detector pairs. The number of counts for each detector pair can be corrected by entering the normalization factor for each detector pair into the following equation,

$$Corrected_{(a,b)} = pCount_{(a,b)}/NF_{(a,b)}, \tag{4}$$

where $pCount_{(a,b)}$ is the number of detected counts in a patient scan.

1.3.1.2 Dead Time

During the detection of a gamma-photon, a signal pulse with finite time duration is produced in the detector. When additional signal pulses occur prior to the first pulse finishing, those additional pulses are lost and a single distorted pulse is formed. These lost valid events are called dead time losses and to prevent the underestimation of radioactivity concentration, corrections for dead time must be applied. The majority of PET systems fit paralyzable or non-paralyzable dead time models to empirical dead time models constructed from measurements taken with various radioactivity concentrations in a range of object sizes and using different energy thresholds. Dead time corrections can be applied globally for the whole system, or to individual pairs of detector modules.

1.3.1.3 Random Coincidence

When two distinct annihilation events occur simultaneously, and a single gamma-photon from each event is detected in coincidence, an erroneous LoR is created. This type of coincidence event is called a random coincidence (see Figure 1-13). Random coincidence events degrade image contrast by adding a uniform background of counts across the PET FoV. These additional background counts skew the relationship between the quantitation of localized activity in a PET image and the actual concentration of radiotracer in the corresponding region of the patient.

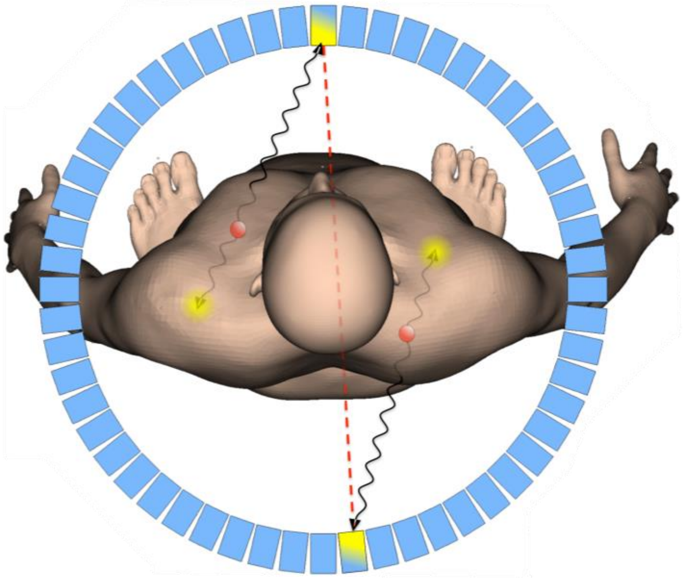

Figure 1-13: A 'random' coincidence event, resulting in a line-of-response (red dotted line) for a non-existent annihilation, while failing to account for the two actual annihilations. This false line-of-response contributes incorrect positional information to the image data.

A commonly used method to correct for random coincidences involves an additional acquisition window with a time delay. If a true coincidence event is recorded as two detection events within a discrete window of time, then the rate of random coincidences can be estimated by temporally shifting the window of time for one of the detectors in a pair. This effectively pairs gamma-photons from two distinct annihilation events, preventing any true coincidence events from being detected. The estimated rate of random coincidences can then be removed from the raw PET data that is collected.

Given that the above random coincidence rate measurement is a sample and not the actual random coincidence count occurring within the true coincidence window, subtracting this estimated value will introduce statistical noise. The amount of uncertainty remaining after this correction can be calculated by,

$$\sigma_{(Trues+Scatter)} = \sqrt{(Trues + Scatter) + (2 \times Randoms)} \tag{5}$$

where $Trues$, $Scatter$, and $Randoms$ represent the true coincidence count, the number of scattered coincidence events, and the number of random coincidence events, respectively.

1.3.1.4 Scattered Coincidence

A scattered coincidence occurs when one or both gamma-photons are redirected from their original trajectories by Compton scattering, yet are still detected in coincidence (Figure 1-14). Scattered coincidences compromise spatial resolution and quantitative accuracy, in a manner similar to that of random coincidences, and contribute to background counts that are dense towards the center of the FoV.

The topic of scattered radiation in quantitative PET imaging has been a long time focus in many publications.[43-50] As such, a great deal of research has been invested in the development of compensation strategies. Among them, the most commonly implemented today is the iterative model-based scatter correction.[51] This correction method begins by taking a measurement of the distribution of densities within the imaging subject from a preliminary reconstruction of the projection data containing both true and scattered coincidences. The PET system's computer then uses the preliminary reconstruction, the density measurements, and a photon propagation model to simulate the scatter detected, producing an estimate of the scatter distribution. This estimate can then be iteratively subtracted from the projection data.

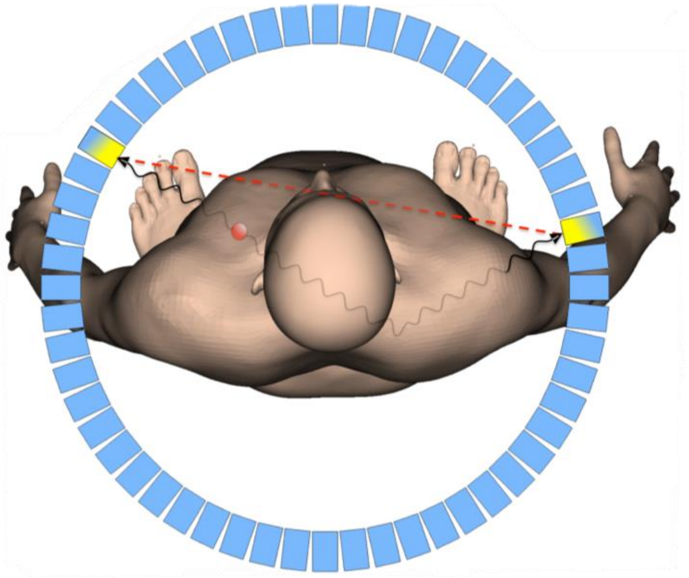

Figure 1-14: A 'scattered' coincidence event. The scattered gamma-photon provides incorrect positional information for the positron annihilation event.

1.3.1.5 Photon Attenuation

Photon attenuation is the gradual loss of photon flux through a medium. In PET reconstructions that do not account for this type of loss, there often appears to be a substantial loss of activity in the central portion of the imaging subject. Other times the effects of attenuation can be subtler and appear as more localized reductions in radiotracer activity (see Figure 1-15). Both outcomes are a crucial source of error, which negatively affect the diagnostic accuracy of the scan.

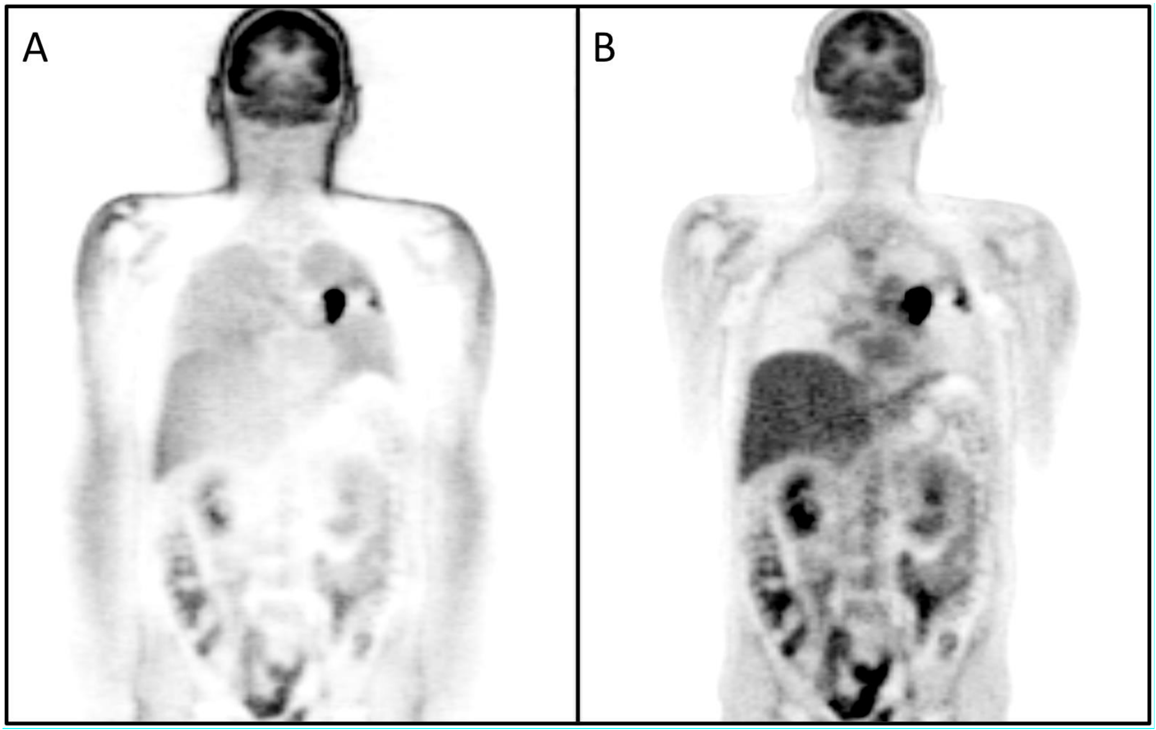

Figure 1-15: A comparison of two reconstructions of the same PET data. A) Image reconstruction without correction for photon attenuation from patient tissues, B) Image Reconstruction with CT-based attenuation correction.

Much like a scattered coincidence, Compton scatter is largely responsible for the process of photon attenuation. But unlike a scattered coincidence, one or both of the photons are lost as they get scattered away from all detector blocks. Current methods of attenuation correction in PET use an estimation of electron density distribution throughout the imaging subject to make corrections during the reconstruction process. The spatial distribution of electron densities is used to calculate a mapping of linear attenuation coefficients (μ) for 511 keV gamma-photons within the PET FoV. This is commonly called a *μ-map*. The accuracy of a μ-map is dependent on the quality of the density measurements of the imaging subject within the PET FoV, and the accuracy of the gamma-photon propagation models used.

Various techniques to estimate patient tissue densities for attenuation correction have been proposed. Broadly speaking, these can be grouped into three categories: non-transmission techniques, transmission techniques, and more recently, MRI-based strategies.

Non-transmission techniques involve the analysis of radiotracer distribution in PET projection data to derive a μ-map. First, PET projection data is used to create a simple geometric boundary around the activity distribution. Then, a uniform attenuation coefficient is contained within this boundary,[52,53] which can be created manually or through various automated processes using scattered projection data, unscattered projection data,[54,55] or both.[56] Although easily implemented, these techniques often suffer from poor contour fits, and fail to reflect the true heterogeneous distribution of densities within a patient.[57]

Photon transmission data can provide direct measurements of densities within an imaging subject. This can be achieved with an external radionuclide source, or X-ray CT. Both X-ray CT and most radionuclides transmit photons at energies other than 511 keV. As such, data from these scans must be scaled for attenuation correction of PET photons. Changes in the dominant photon interactions in different materials complicate the conversion from transmission energy data to PET μ-map. For example, Compton scatter is the dominant interaction for 511keV photons in soft-tissues, but in bone photoelectric interactions dominate at that energy. To further complicate the conversion, x-ray CT transmits a polyenergetic spectrum of photons, usually in the range of 40-140 keV. Fortunately, previous work on this problem has resulted in bilinear mapping functions to make these corrections possible and have been shown to work well for both single and polyenergetic transmission scans.[58-60]

MRI-based strategies for attenuation estimation can be divided into three categories: mapping, atlas-based, and segmentation. Approaches that use mapping attempt to convert MRI voxels to linear attenuation coefficients via some mathematical function. Despite its potential, the lack of signal from lung and bone tissues in conventional MRI pulse sequences, limit our ability to distinguish one from the other. An atlas-based approach uses previously acquired data, such as an x-ray CT, to create a model or an atlas of the spatial distribution of tissue densities. This atlas can then be registered to a patient specific MRI, which may be acquired at the same time as the PET, to create a patient specific μ-map. Although this technique can provide distinct density information for lung and bone tissues, these values are not patient specific. Additionally, an atlas may not be appropriate to use for patients who significantly deviate from the atlas' sample population. The third approach, segmentation creates a patient specific μ-map by dividing the patient's MR image into the various classifications of tissues. Each tissue class is then assigned a theoretical attenuation value. Similar to mapping approaches, segmentation cannot easily distinguish between bone and lung tissues based solely on voxel intensity. However, the current implementation on a Siemens mMR Biograph PET/MRI, which uses a 2-point Dixon sequence to map fat- and water-based tissues into a 4-class model (background, lungs, fat, and soft tissue) for whole-body scans, provide similar results to those of conventional attenuation correction with low-dose CT.[61,62] More recently, methods to better differentiate air and bone with the use of ultrashort echo time sequences (UTE), have achieved a better than 2-4% difference from CT-based μ-maps for brain imaging.[63,64]

1.4 Hybrid Imaging

Although PET provides clinicians with the ability to image specific molecular targets associated with cancer to help facilitate earlier diagnosis and improve patient management, its usefulness is limited without anatomical reference. The hybridization of PET with anatomical modalities like CT and MRI has been an important catalyst to the growth in clinical use of PET for oncology imaging. Hybrid PET/CT and PET/MRI offer better coregistration between modalities than images acquired during separate sessions, leading to decreased scans times and improved diagnostic accuracy.

1.4.1 PET/CT

The late 1990's saw the introduction of hybrid PET/CT, catalyzing the proliferation of PET as a diagnostic tool. The ability to relate specific molecular information, through the distribution of biologically active radiotracers, to detailed anatomical information, via x-ray CT, has helped to make PET/CT a powerful tool for cancer detection. Moreover, the specificity of ^{18}F-FDG PET/CT has been shown to help in the identification of non-specific benign lesions,[65,66] and its sensitivity can aid in the early detection of tumours, making early treatment possible.[67]

FDG-PET/CT has also been shown to be a useful tool in cancer staging. It was found to be more accurate than CT alone, for staging disease in the mediastinum of lung cancer patients.[68] Studies have shown FDG-PET/CT to improve the prediction of stage I and II disease over PET alone, in patients with non-small cell lung cancer (NSCLC). Additionally, hybrid PET/CT allows for better prediction of tumour size, nearby tissue involvement (T), and nearby lymph node involvement (N) in patients with lymphoma.[69]

Follow-up PET scans may help detect progressive disease or recurrence and selectively offering a PET/CT scan to patients without symptoms may allow for an effective follow-up treatment.[70]

The hybridization of PET and CT has also allowed for much faster, less noisy, and higher spatial resolution μ-maps than previously used radionuclide transmission scans. However, the use of x-ray CT results in a higher dose to the patient, due to the increased flux of photons. Compared to a typical radionuclide transmission scan, which can impart a dose of 0.20-0.26 mSv,[71] an average whole-body CT scan can deliver anywhere from 7.22-25.95 mSv, depending on the protocol used and, the patient size.[72] A standard FDG-PET imaging session can result in a whole body dose of 6.23-10.73 mSv.[72,73] Dose reduction strategies for X-ray CT, including iterative reconstruction algorithms, x-ray tubes with variable current, and models of statistical processes of x-ray measurements have been investigated by many groups to deal with the issue of patient dose.[74-79] It is also important to note that acquisition parameters can be adjusted for a ‘PET attenuation correction only’ CT to achieve doses as low as 0.5-1mSv.[80]

1.4.2 PET/MRI

Combining the molecular information of PET with the excellent soft-tissue contrast of MRI represents the merging of two very different but flexible imaging modalities. Although CT is excellent for acquiring detailed images of boney anatomy, MRI outperforms it in soft-tissue imaging. A prospective comparison in determining disease extent in CT and MR images of soft-tissue sarcomas showed that 23% of tumours found in MRI were missed in CT.[81] These findings are consistent with other studies involving soft-tissue cancer imaging.[82,83] These findings suggest that PET/MRI may be advantageous over PET/CT in some oncology screening and perhaps treatment planning applications.

At the beginning of section 1.3, I discussed the role of photomultiplier tubes (PMTs) in conventional PET and PET/CT scanners to locate the absorption of gamma-photons within the scintillator crystal. However, a significant technical hurdle in the hybridization of PET with MRI was the PMT's sensitivity to magnetic fields. Mu-metal is a metallic alloy characterized by its ability to attenuate magnetic fields. In conventional use of PMTs, mu-metal is wrapped around a PMT to shield it from low-frequency magnetic fields. Unfortunately, the multi-Tesla fields of MRI systems exceed the mu-metal's shielding ability, rendering PMTs useless.

Several designs have been proposed, to overcome this incompatibility. One design placed the PMTs and all metallic PET detecting components outside the MRI's magnetic field, and lead scintillation light to the PMTs with fiber-optic cables.[84-90] Although, the magnetic field's influence on the PMTs was effectively reduced, the design degraded performance and reduced the FoV of PET.[87] Other designs involving special magnets, such as field-cycled magnets[91] and split magnet systems[92] have also been implemented. However, these systems have limited performance, due to the weaker field strengths of these magnet designs. Some of the more widely commercialized designs have forgone the traditional PMT altogether, and replaced them with solid-state silicon photo sensors called avalanche photodiodes (APDs)[93] or another called silicon photomultipliers (SiPMs).[94] These compact photo sensors are not sensitive to magnetic fields[93,94] and are now used in preclinical,[87,96-98] and clinical hybrid PET/MRI systems.[99,100] Although insensitive to magnetic fields, both APDs and SiPMs are temperature sensitive and are designed with water cooling systems to maintain a constant temperature of 20°C and 18°C respectively.

Significant efforts have been invested in optimizing both PET and MRI hardware components for compatibility, to minimize interference between modalities in clinical systems. To prevent gradient field linearity of the MRI from being distorted, PET detection hardware is made with non-magnetic materials and designed to be gradient transparent. To prevent interference with the MRI's RF signals, all PET detector electronics are shielded from emitting their own RF signals.

To optimize MRI hardware compatibility with PET, MRI RF coils have been designed with specific geometries and materials to optimize their PET photon transparency. Additionally, rigid hardware components that have a fixed position in relation to the patient table, such as a head RF coil, a breast coil, or the patient table itself, have CT-based μ-maps to provide attenuation correction during PET reconstruction. Given that the PET/MRI can identify the position of the patient table for each scan, and these rigid components have a fixed position, relative to the patient table, their μ-maps can be registered appropriately and incorporated into the reconstruction process. PET transparency is emphasized for more flexible hardware components, which cannot be located in this manner.

1.5 Imaging for Radiotherapy Planning

Radiation therapy uses precisely targeted and controlled doses of high-energy ionizing radiation to kill cancer cells while attempting to spare normal healthy tissues. Since the late 1970's, radiotherapy planning techniques use CT image volumes of patient anatomy to define target volumes and calculate radiation doses to the tumour and surrounding tissues.[101] Since then, the incorporation of other imaging modalities such as MRI and PET has proven useful in radiotherapy planning. These modalities can provide additional information to more precisely define the locations of both tumours and vital organs.[102-104] Soft-tissue contrast in MRI is superior to that of CT. This allows a clinician to better discriminate between a target and the surrounding healthy tissue.[105,106] PET allows specific molecular characteristic of tissues to be identified, allowing a radiation oncologist to prescribe an escalated radiation dose to more aggressively growing tumours.[107,108] Combining information from multiple modalities can reduce the uncertainty of tumour location, size, and invasiveness, thus potentially improving treatment outcomes.

1.5.1 Motion Management

The image quality for all three modalities can be compromised in the presence of motion. Motion management strategies for CT, MRI, and PET have been studied extensively, and many potential solutions have been suggested.

Although respiratory motion can affect thoracic, abdominal, and pelvic tumour sites, it is most prominent and often seen with lung tumours. The challenge of imaging in the presence of respiratory motion has brought about various techniques to either mitigate or capture this motion. These techniques attempt to provide sufficiently accurate images to facilitate patient diagnosis and intervention guidance. In the case of the latter, we can look to image-guided radiation therapy (IGRT) as an example of how both clarity of the image and motion information are of great importance in the presence of respiratory motion.[109] As the technology of radiation therapy (RT) delivery systems evolve, efforts to capitalize on these improvements by maximizing target dose and minimizing collateral dose to critical structures will be accomplished through increasingly conformal planning target volumes (PTVs). To make this possible, the pre-treatment imaging used to create such conformal PTVs must also evolve to incorporate the best in tissue contrast, molecular information, and motion characterization.

Among the modalities used for pre-treatment imaging, three have garnered the interest of many working on the problem of respiratory motion in 3 dimensional (3D) imaging and motion management; they are X-ray Computed Tomography (CT), Magnetic Resonance Imaging (MRI), and the hybridization of both with Positron Emission Tomography (PET).

1.5.1.1 Motion and CT

The first technique is slow CT, where multiple respiration phases are captured for each slice.[110-112] This provides a motion averaged image volume, showing the range of tumour motion during the acquisition. One advantage to this approach is the volume distribution used to calculate the dose is similar to that of the motion that would be observed during free-breathing treatment. However, motion averaging in the image and potential deviations during treatment from the imaged motion range may increase observer errors for both target and normal organ delineations.[109]

The second technique is a breath-hold acquisition, performed at both end inhalation and end exhalation.[113] Although this technique offers significantly reduced motion blur caused by free-breathing, the scanning time required for this is often more than double. This technique is also dependent on patient compliance. Otherwise, a gated acquisition might be needed, which requires a respiratory monitoring system. It is important to note that gated free-breathing and breath-hold acquisitions do not offer identical positioning and this must be taken into account when using for treatment delivery planning.

The last (and most common) of the three techniques is four-dimensional CT (4D-CT), which can provide detailed temporal information in addition to the 3D spatial information that we get from the previously mentioned techniques.[114,114] Information about tumour range of motion, average tumour position, and tumour proximity to other organs during each phase of respiration can be obtained with 4D-CT.[116] Although this technique provides a promising solution to capturing respiratory motion in lung tumours, it is still subject to artefacts from variable breathing patterns, even with the implementation of breathing-training.[117]

1.5.1.2 Motion and MRI

As with all of the above-mentioned CT techniques, 4D-CT suffers from poor soft-tissue contrast when compared to MRI. Also, due to imaging dose, CT may not be the ideal modality for monitoring disease progression or tumour response through serial imaging.

MRI however, provides excellent anatomical imaging with superb soft-tissue contrast. Also, with no ionizing radiation exposure to the patient during scans, it comes as no surprise that it is currently used for screening, staging, and more recently both pre- and during-treatment guidance. Most respiratory motion management strategies for clinical MRI aim to correct for motion artefacts, instead of capturing motion information. In a similar manner to the previously mentioned strategies used for CT, respiratory motion in MRI can be managed with the use of various breath-hold[118-120] or gating strategies.[121,122] The remaining strategies, which aim to capture respiratory motion, have generally been accomplished by one of two methods; using rapid 3D acquisitions over time (3D+t),[123] or fast 2D acquisitions over time and repeated in adjacent slices in the third dimension (2D+t+D).[124] For the latter, each 2D image slice needs to be retrospectively assigned to the appropriate respiratory state to build each 3D image volume. This is done by using a surrogate for respiratory phase.[125-127] However, many of these techniques are limited to T1-weighted sequences, which generally have inferior tumour-tissue contrast compared to longer TR, T2-weighted and diffusion-weighted imaging.[123,125-127]

1.5.1.3 Motion and PET

The availability of radiotracers capable of targeting specific characteristics of cancer, like rapid cell proliferation and hypermetabolism, along with great sensitivity to these radiotracers in low concentrations, have made PET an important imaging tool in oncology. More importantly, its hybridization with CT has made it possible to accurately locate biochemical processes of PET tracers in relation to patient anatomy in CT images.[128] For example, the use of 18F-fluorodeoxyglucose (FDG) -PET/CT has been shown to be more accurate at staging disease, tumour size, nearby tissue invasion (T), nodal involvement (N), for patients with non-small cell lung cancer (NSCLC).[68] For this to be achieved, good spatial correlation between the two modalities must be ensured to accurately locate PET activity, and since the CT is used to calculate the attenuation map for PET, correlation is also necessary for quantitative accuracy.

More recently we have seen the hybridization of MRI with PET,[99] and since then studies have shown it to be as effective as PET/CT at identifying and staging disease, and more so in certain applications.[129,130] It has also been suggested that PET/MRI be the new standard for detecting liver metastases,[131] and with new techniques that capitalize on PET/MRI’s simultaneity, it could become a standard for motion imaging.

However, due to the low photon fluence rate of PET imaging, longer acquisition times are required. Depending on the protocol, these scan times can be on the order of minutes to hours. These longer scan times make PET images more susceptible to motion blurring artefacts, particularly in thoracic images where respiratory and cardiac motion is difficult to impossible for the patient to control. Motion blurring in PET for cancer diagnosis, staging and intervention planning can lead to quantitative inaccuracies of radiotracer concentration estimation, overestimation of lesion volume, and spatial mismatches between modalities when hybridized.[132] PET events can be linked with a timestamp when recorded in a format called list-mode. These timestamps can be used in combination with a respiratory surrogate or a hybrid modality, to sort photon detection events into separate 'bins'. Bins can then be used to include/exclude photon detection events in the image reconstruction, to correct respiratory motion blurring through techniques called 'respiratory-correlated dynamic PET' or 'gated'/'4D-PET'.

Respiratory-correlated dynamic PET requires a ^{68}Ge point source placed on the diaphragm of the patient within the FoV, PET data is acquired, and images are analysed.[133] Those with the point source at a specific position are separated to identify a specific phase. Sinograms can then be reconstructed iteratively from the separated data. Although this technique does not require any tracking hardware to monitor patient respiratory motion, the computation time required is a disadvantage.

The more commonly used gated-PET divides photon events from each phase of respiration into separate bins. These bins are independently used to reconstruct static images, representing the different phases of respiration. Although the result is a motion-free image for each respiratory phase, gated-PET only makes use of a portion of the coincidence events, causing noisy images. Increasing acquisition times or increasing radionuclide dose can improve noisy images, but neither of these is desirable. To reduce noise without increasing time or dose, several types of motion correction techniques that make use of all coincidence events, have been proposed. These include simultaneous estimation of motion and image reconstruction,[134] reconstruction using a time-varying system matrix,[135-137] event rebinning,[138-140] and summing of aligned images.[141-143]

1.6 Gaps in knowledge, challenges, questions, and hypothesis

Since the introduction of clinical hybrid PET-MRI systems, research exploring its potential applications has garnered a great deal of interest. The fusion of PET's molecular information with MRI's superb soft-tissue contrast provides excellent anatomical landmark information for target delineation for radiotherapy planning. MRI acquisitions often require the positioning of RF-coil hardware within the FoV and these components are a significant source of photon attenuation in hybrid PET-MRI systems. Current MR-hardware attenuation correction methods rely on the conversion of CT scans of the MR- hardware to attenuation maps. However, these CT scans use x-rays in the kilovoltage range and are susceptible to various types of artefacts caused by dense materials found in the hardware. Artefacts in these CT images get incorporated into the attenuation maps, leading to quantitative inaccuracies in PET data they are meant to correct. Additionally, recent developments in radiotherapy technology are allowing for more conformal planning to treat moving targets in patients. As such, imaging protocols designed to correct and characterize motion will be more commonly used in planning and the quality assurance of these protocols will be needed. Future applications of hybrid PET-MRI in radiotherapy planning will be effected by the following challenges:

1. The integration of PET imaging for adaptive radiotherapy planning strongly depends on the quantitative accuracy of target volumes. In hybrid PET-MRI this requires accurate correction for PET photon attenuation caused by the presence of MRI hardware in the PET FoV. Current kilovoltage CT-based methods of constructing MRI hardware μ-maps are prone to various artefacts caused by the dense materials in the hardware. As a result, PET volumes reconstructed with μ-maps that contain these errors will also contain inaccuracies. Hence, there is a need for a technique capable of producing artefact free images of MRI hardware for the purpose of calculating accurate μ-maps for PET.

2. In the case of lung, liver, and esophageal cancers, motion can be problematic for radiotherapy treatment planning images. Before motion correction imaging protocols can be incorporated into a radiotherapy planning workflow, quality

assurance tests should be available to confirm the protocol’s ability accurately mitigate the effects of motion or characterize the motion. Current methods used for quality assurance of CT imaging and radiotherapy to moving targets involve the use of programmable motion phantoms, such as the Quasar respiratory motion phantom (Modus Medical Devices, London, Canada) and the CIRS Dynamic Thorax Phantom (Computerized Imaging Reference Systems, Incorporated, Norfolk, USA). However, these phantoms cannot be run within the static magnetic field of an MRI, and are not designed for use with a PET tracer. Therefore, there is an unmet need for a simple quality assurance phantom, similar to that of the Quasar phantom that is compatible with MRI, PET, and CT, suitable for hybrid PET/MRI.

To address these challenges, I have posed the following research questions:

1. Can accurate μ-maps be derived from DECT and MVCT images of RF coils, for use in quantitative PET-MR imaging?

2. Can an MR-PET compatible motion phantom be designed to evaluate the accuracy and PET sensitivity of respiratory-triggered PET-MRI protocols under controlled conditions?

3. Can tumour respiratory motion be characterized using coregistered dynamic 3D MRI and PET volumes?

Therefore the work within this thesis investigates the following hypotheses:

1. *MVCT can significantly improve the accuracy of mu-maps for RF coils used for hybrid PET-MRI.*

2. *Verification of moving target accuracy in hybrid PET-MR images requires a custom PET and MRI compatible motion phantom.*

3. *Multi-phase 4D-PET-MRI can yield more information about tumour motion characteristics than single-phase respiratory-triggered PET-MRI.*

The overarching goal for this research was to further develop PET-MR imaging for applications in precision radiotherapy.

1.7 Thesis Overview

1.7.1 A Comparison of Megavoltage, Dual-energy, and Single-energy CT-based μ-maps for a 4 Channel Breast Coil in PET/MRI (Chapter 2)

Two novel CT-based methods of constructing attenuation maps of MRI hardware for PET imaging are described and compared with a previously described method by Aklan *et al* (2013).[144] Current methods of creating attenuation maps for MRI hardware, such as the one described by Aklan, use CT images derived from a single-energy spectrum of photons in the kilovoltage range. This technique is prone to artefacts caused by the interaction between highly attenuating components in the hardware and photons in this energy range. The first of our CT-based methods uses a single-energy spectrum of photons in the megavoltage range. Higher energy photons allow for better penetration through dense materials resulting in fewer image artefacts. The second of our methods uses a dual-energy spectrum approach to reconstruct virtual monoenergetic image volumes. Monoenergetic images are less susceptible to one of the sources artefact caused by the interactions of polyenergetic spectra in the kilovoltage range and highly attenuating material. Improvements in hardware imaging can increase the accuracy of corrections needed while they are in the PET field of view. With PET playing an increasingly important role in radiotherapy planning, this work represents a step towards improving the utility of hybrid PET/MRI in radiotherapy applications through more quantitatively accurate PET in the presence of MRI hardware.

1.7.2 Accuracy and sensitivity of respiratory-triggered PET-MRI evaluated using a multi-modality motion platform (Chapter 3)

This chapter describes the development and testing of a multi-modality compatible tumour respiratory motion phantom for use in the development and quality assurance of hybrid PET/MRI or PET/CT imaging protocols. The phantom was designed to be used with an MRI-compatible motion stage developed in previous work, “Design and evaluation of an MRI-compatible linear motion stage," published in *Medical physics* vol. 43 (1) pp. 62-71 (2016) by Tavallaei MA, Johnson PM, Liu J, Drangova M.[145] Testing of the completed phantom involved measurements and evaluation of currently available clinical protocols on a Siemens mMR Biograph, hybrid PET/MRI. This chapter focuses on using the phantom to test a real-time 2D balanced steady-state free precession MR sequence to characterize motion and a respiratory-triggered PROPELLER MRI protocol combined with gated PET in reproducing moving lesion-compartment geometries and tracer quantities. This work provides a necessary tool for the protocol development in chapter 4 and fulfills an unmet need for a PET/MRI/CT-compatible motion phantom that can be used for quality assurance of hybrid imaging techniques with motion correction.

1.7.3 Development and evaluation of an amplitude-based 4D-PET/MRI protocol to characterize tumour respiratory motion (Chapter 4)

In Chapter 4, an amplitude-based 4D-PET/MRI protocol is described and evaluated in the physical phantom model presented in Chapter 3. One simulated regular and two irregular respiratory motion patterns taken from real patient data where used to evaluate this protocol. The irregular respiratory patterns exhibit different combinations of the three types of breathing irregularities that may be encountered in a clinical scenario; frequency changes, amplitude changes, and baseline shifts.

1.7.4 Conclusions (Chapter 5)

The final chapter of this thesis first summarizes the main findings of the previous chapters and discusses the experimental and clinical relevance of the results. This is followed with a discussion of possible directions for future research related to these findings. Lastly, the final conclusions of this thesis are presented.

1.7.5 References

1. Hounsfield GN. Computerized transverse axial scanning (tomography): Part 1. Description of system. *Br J Radiol*. 1973;46(552):1016-1022.

2. Ambrose J. Computerized transverse axial scanning (tomography): Part 2. Clinical application*. *Br J Radiol*. 1973;46(552):1023-1047.

3. ECRI. *Healthcare Product Comparison System (HPCS), Scanning Systems, Computed Tomography, Full-Body*.; 2002.

4. Hendee WR, Ritenour ER, Hoffmann KR. *Medical Imaging Physics, Fourth Edition*. Vol 30.; 2003.

5. Boas FE, Fleischmann D. CT artifacts: causes and reduction techniques. *Imaging Med*. 2012;4(2):229-240.

6. Barrett JF, Keat N. Artifacts in CT: Recognition and Avoidance. *RadioGraphics*. 2004;24(6):1679-1691.

7. Huang J. et al. An evaluation of three commercially available metal artifact reduction methods for CT imaging. *Phys Med Biol*. 2015;60(3):1047-1067.

8. So A, Lee T-Y, Imai Y, et al. Quantitative myocardial perfusion imaging using rapid kVp switch dual-energy CT: Preliminary experience. *J Cardiovasc Comput Tomogr*. 2011;5(6):430-442.

9. Kalender WA, Perman WH, Vetter JR, Klotz E. Evaluation of a prototype dual-energy computed tomographic apparatus. I. Phantom studies. *Med Phys*. 1986;13(3):334-339.

10. Vetter JR, Perman WH, Kalender WA, Mazess RB, Holden JE. Evaluation of a prototype dual-energy computed tomographic apparatus. II. Determination of vertebral bone mineral content. *Med Phys*. 1986;13(3):340-343.

11. Flohr TG, McCollough CH, Bruder H, et al. First performance evaluation of a

dual-source CT (DSCT) system. *Eur Radiol*. 2006;16(2):256-268.

12. Petersilka M, Bruder H, Krauss B, Stierstorfer K, Flohr TG. Technical principles of dual source CT. *Eur J Radiol*. 2008;68(3):362-368.

13. Voodoo Manufacturing, Life-Size Body Model. www.thingiverse.com/thing:1615359 . Jun 10, 2016.

14. Scheffel H, Stolzmann P, Frauenfelder T, et al. Dual-energy contrast-enhanced computed tomography for the detection of urinary stone disease. *Invest Radiol*. 2007;42(12):823-829.

15. Primak AN, Fletcher JG, Vrtiska TJ, et al. Noninvasive differentiation of uric acid versus non–uric acid kidney stones using dual-energy CT. *Acad Radiol*. 2007;14(12):1441-1447.

16. Graser A, Johnson TRC, Bader M, et al. Dual energy CT characterization of urinary calculi: initial in vitro and clinical experience. *Invest Radiol*. 2008;43(2):112-119.

17. Graser A, Johnson TRC, Hecht EM, et al. Dual-energy CT in patients suspected of having renal masses: can virtual nonenhanced images replace true nonenhanced images? 1. *Radiology*. 2009;252(2):433-440.

18. Thieme SF, Becker CR, Hacker M, Nikolaou K, Reiser MF, Johnson TRC. Dual energy CT for the assessment of lung perfusion—correlation to scintigraphy. *Eur J Radiol*. 2008;68(3):369-374.

19. Thieme SF, Johnson TRC, Lee C, et al. Dual-energy CT for the assessment of contrast material distribution in the pulmonary parenchyma. *Am J Roentgenol*. 2009;193(1):144-149.

20. Holmes DR, Fletcher JG, Apel A, et al. Evaluation of non-linear blending in dual-energy computed tomography. *Eur J Radiol*. 2008;68(3):409-413.

21. Alvarez RE, Macovski A. Energy-selective reconstructions in x-ray computerised tomography. *Phys Med Biol*. 1976;21(5):733.

22. Brooks RA. A quantitative theory of the Hounsfield unit and its application to dual energy scanning. *J Comput Assist Tomogr*. 1977;1(4):487-493.

23. Bamberg F, Dierks A, Nikolaou K, Reiser MF, Becker CR, Johnson TRC. Metal artifact reduction by dual energy computed tomography using monoenergetic extrapolation. *Eur Radiol*. 2011;21(7):1424-1429.

24. Schreiner LJ, Rogers M, Salomons G, Kerr A. Metal Artifact Suppression in Megavoltage Computed Tomography. *Proc SPIE*. 5745:637.

25. Rogers M, Kerr A, Salomons G, Schreiner LJ. Quantitative Investigations of Megavoltage Computed Tomography. Flynn MJ, ed. *Proc SPIE*. 2005;5745(613):685.

26. Yartsev S, Kron T, Van Dyk J. Tomotherapy as a tool in image-guided radiation therapy (IGRT): theoretical and technological aspects. *Biomed Imaging Interv J*. 2007;3(1):e16.

27. Boas FE, Fleischmann D. Evaluation of two iterative techniques for reducing metal artifacts in computed tomography. *Radiology*. 2011;259(3):894-902.

28. Abdoli M, Ay MR, Ahmadian A, Dierckx RAJO, Zaidi H. Reduction of dental filling metallic artifacts in CT- based attenuation correction of PET data using weighted virtual sinograms optimized by a genetic algorithm. *Med Phys*. 2010;37(12):6166-6177.

29. Joemai R, de Bruin PW, Veldkamp WJH, Geleijns J. Metal artifact reduction for CT: Development, implementation, and clinical comparison of a generic and a scanner- specific technique. *Med Phys*. 2012;39(2):1125-1132.

30. Veldkamp WJH, Joemai R, van der Molen AJ, Geleijns J. Development and validation of segmentation and interpolation techniques in sinograms for metal

artifact suppression in CT. *Med Phys*. 2010;37(2):620-628.

31. Prell D, Kyriakou Y, Beister M, Kalender WA. A novel forward projection-based metal artifact reduction method for flat-detector computed tomography. *Phys Med Biol*. 2009;54(21):6575.

32. Fleischmann D, Boas FE. Computed tomography—old ideas and new technology. 2011.

33. Pan X, Sidky EY, Vannier M. Why do commercial CT scanners still employ traditional, filtered back-projection for image reconstruction? *Inverse Probl*. 2009;25(12):123009.

34. Xu F, Xu W, Jones M, et al. On the efficiency of iterative ordered subset reconstruction algorithms for acceleration on GPUs. *Comput Methods Programs Biomed*. 2010;98(3):261-270.

35. Kondo A, Hayakawa Y, Dong J, Honda A. Iterative correction applied to streak artifact reduction in an X-ray computed tomography image of the dento-alveolar region. *Oral Radiol*. 2010;26(1):61-65.

36. Dong J, Kondo A, Abe K, Hayakawa Y. Successive iterative restoration applied to streak artifact reduction in X-ray CT image of dento-alveolar region. *Int J Comput Assist Radiol Surg*. 2011;6(5):635-640.

37. Eran A, Ozturk A, Aygun N, Izbudak I. Medulloblastoma: atypical CT and MRI findings in children. *Pediatr Radiol*. 2010;40(7):1254-1262.

38. Dale L Bailey, David W Townsend PEV and MNM, Bailey DL, Townsend DW, Valk PE, Maisey MN. *Positron Emission Tomography*. Vol 51. Springer; 2005.

39. Meikle SR, Beekman FJ, Rose SE. Complementary molecular imaging technologies: High resolution SPECT, PET and MRI. *Drug Discov Today Technol*. 2006;3(2):187-194.

40. Surti S, Karp JS, Muehllehner G, Raby PS. Investigation of lanthanum scintillators for 3D PET. *IEEE Trans Nucl Sci*. 2003;50(3):348-354.

41. Karp JS, Kuhn A, Perkins AE, et al. Characterization of a time-of-flight PET scanner based on lanthanum bromide. *IEEE Nucl Sci Symp Conf Rec*. 2005;4:1919-1923.

42. Daube-Witherspoon ME, Surti S, Perkins a, et al. The imaging performance of a LaBr3-based PET scanner. *Phys Med Biol*. 2010;55(1):45-64.

43. Links JM. Scattered Photons as “Good Counts Gone Bad:” Are They Reformable or Should They Be Permanently Removed from Society? *J Nucl Med*. 1995;36(1):130-132.

44. Msaki P, Bentourkin M, Lecomte R. Scatter Degradation and Correction Models for High-Resolution PET. *J Nucl Med*. 1996;37(12):2047-2049.

45. Bailey DL, Meikle SR. A convolution-subtraction scatter correction method for 3D PET. *Phys Med Biol*. 1994;39(3):411.

46. Grootoonk S, Spinks TJ, Sashin D, Spyrou NM, Jones T. Correction for scatter in 3D brain PET using a dual energy window method. *Phys Med Biol*. 1996;41(12):2757.

47. Levin CS, Dahlbom M, Hoffman EJ. A Monte Carlo correction for the effect of Compton scattering in 3-D PET brain imaging. *IEEE Trans Nucl Sci*. 1995;42(4):1181-1185.

48. Ollinger JM. Model-based scatter correction for fully 3D PET. *Phys Med Biol*. 1996;41(1):153.

49. Watson CC, Newport D, Casey ME, Beanlands RS, Schmand M. Evaluation of simulation-based scatter correction for 3-D PET cardiac imaging. *IEEE Trans Nucl Sci*. 1997;44(1):90-97.

50. Bentourkia M, Lecomte R. Energy dependence of nonstationary scatter subtraction-restoration in high resolution PET. *IEEE Trans Med Imaging*. 1999;18(1):66-73.

51. Zaidi H. Scatter modelling and correction strategies in fully 3-D PET. *Nucl Med Commun*. 2001;22(11).

52. Macey DJ, DeNardo GL, DeNardo SJ. Comparison of three boundary detection methods for SPECT using Compton scattered photons. *J Nucl Med Off Publ Soc Nucl Med*. 1988;29(2):203-207.

53. Younes R Ben, Mas J, Bidet R. A fully automated contour detection algorithm the preliminary step for scatter and attenuation compensation in SPECT. *Eur J Nucl Med*. 1988;14(12):586-589.

54. Hebert TJ, Gopal SS, Murphy P. A fully automated optimization algorithm for determining the 3-D patient contour from photo-peak projection data in SPECT. *IEEE Trans Med Imaging*. 1995;14(1):122-131.

55. Tomitani T. An edge detection algorithm for attenuation correction in emission CT. *IEEE Trans Nucl Sci*. 1987;34(1):309-312.

56. Pan T-S, King MA, Luo D-S, Dahlberg ST, Villegas BJ. Estimation of attenuation maps from scatter and photopeak window single photon-emission computed tomographic images of technetium 99m-labeled sestamibi. *J Nucl Cardiol*. 1997;4(1):42-51.

57. Larsson SA. Gamma camera emission tomography. Development and properties of a multi-sectional emission computed tomography system. *Acta Radiol Suppl*. 1980;363:1-75.

58. Kinahan PE, Townsend DW, Beyer T, Sashin D. Attenuation correction for a combined 3D PET/CT scanner. *Med Phys*. 1998;25(10):2046-2053.

59. Burger C, Goerres G, Schoenes S, Buck A, Lonn AHR, von Schulthess GK. PET attenuation coefficients from CT images: experimental evaluation of the transformation of CT into PET 511-keV attenuation coefficients. *Eur J Nucl Med Mol Imaging*. 2002;29(7):922-927.

60. Battista JJ, Rider WD, Van Dyk J. Computed tomography for radiotherapy planning. *Int J Radiat Oncol Biol Phys*. 1980;6(1):99-107.

61. Dixon WT. Simple proton spectroscopic imaging. *Radiology*. 1984;153(1):189-194.

62. Martinez-Möller A, Souvatzoglou M, Delso G, et al. Tissue Classification as a Potential Approach for Attenuation Correction in Whole-Body PET/MRI: Evaluation with PET/CT Data. *J Nucl Med*. 2009;50(4):520-526.

63. Ladefoged CN, Benoit D, Law I, et al. Region specific optimization of continuous linear attenuation coefficients based on UTE (RESOLUTE): application to PET/MR brain imaging. *Phys Med Biol*. 2015;60(20):8047-8065.

64. Ladefoged CN, Law I, Anazodo U, et al. A multi-centre evaluation of eleven clinically feasible brain PET/MRI attenuation correction techniques using a large cohort of patients. *Neuroimage*. 2016;147(December 2016):346-359.

65. Even-Sapir E, Metser U, Mishani E, Lievshitz G, Lerman H, Leibovitch I. The detection of bone metastases in patients with high-risk prostate cancer: 99mTc-MDP Planar bone scintigraphy, single- and multi-field-of-view SPECT, 18F-fluoride PET, and 18F-fluoride PET/CT. *J Nucl Med*. 2006;47(2):287-297.

66. Even-Sapir E, Mishani E, Flusser G, Metser U. 18F-Fluoride positron emission tomography and positron emission tomography/computed tomography. *Semin Nucl Med*. 2007;37(6):462-469.

67. Signorelli M, Guerra L, Buda A, et al. Role of the integrated FDG PET/CT in the surgical management of patients with high risk clinical early stage endometrial cancer: detection of pelvic nodal metastases. *Gynecol Oncol*. 2009;115(2):231-235.

68. Wahl RL, Quint LE, Greenough RL, Meyer CR, White RI, Orringer MB. Staging of mediastinal non-small cell lung cancer with FDG PET, CT, and fusion images: preliminary prospective evaluation. *Radiology*. 1994;191(2):371-377.

69. Freudenberg LS, Antoch G, Schütt P, et al. FDG-PET/CT in re-staging of patients with lymphoma. *Eur J Nucl Med Mol Imaging*. 2004;31(3):325-329.

70. van Loon J, Grutters J, Wanders R, et al. Follow-up with 18FDG-PET-CT after radical radiotherapy with or without chemotherapy allows the detection of potentially curable progressive disease in non-small cell lung cancer patients: a prospective study. *Eur J Cancer*. 2009;45(4):588-595.

71. Wu T-H, Huang Y-H, Lee JJS, et al. Radiation exposure during transmission measurements: comparison between CT- and germanium-based techniques with a current PET scanner. *Eur J Nucl Med Mol Imaging*. 2004;31(1):38-43.

72. Huang B, Law MW-M, Khong P-L. Whole-body PET/CT scanning: estimation of radiation dose and cancer risk. *Radiology*. 2009;251(1):166-174.

73. Deloar HM, Fujiwara T, Shidahara M, et al. Estimation of absorbed dose for 2-[F-18] fluoro-2-deoxy-D-glucose using whole-body positron emission tomography and magnetic resonance imaging. *Eur J Nucl Med*. 1998;25(6):565-574.

74. Silva AC, Lawder HJ, Hara A, Kujak J, Pavlicek W. Innovations in CT dose reduction strategy: application of the adaptive statistical iterative reconstruction algorithm. *Am J Roentgenol*. 2010;194(1):191-199.

75. Hara AK, Paden RG, Silva AC, Kujak JL, Lawder HJ, Pavlicek W. Iterative reconstruction technique for reducing body radiation dose at CT: feasibility study. *Am J Roentgenol*. 2009;193(3):764-771.

76. Prakash P, Kalra MK, Kambadakone AK, et al. Reducing abdominal CT radiation dose with adaptive statistical iterative reconstruction technique. *Invest Radiol*. 2010;45(4):202-210.

77. Thibault J-B, Sauer KD, Bouman CA, Hsieh J. A three-dimensional statistical approach to improved image quality for multislice helical CT. *Med Phys*. 2007;34(11):4526-4544.

78. Lee CH, Goo JM, Ye HJ, et al. Radiation Dose Modulation Techniques in the Multidetector CT Era: From Basics to Practice 1. *Radiographics*. 2008;28(5):1451-1459.

79. Yu Z, Thibault J-B, Bouman CA, Sauer KD, Hsieh J. Fast model-based X-ray CT reconstruction using spatially nonhomogeneous ICD optimization. *IEEE Trans image Process*. 2011;20(1):161-175.

80. Case JA. Minimizing the radiation dose of CT attenuation correction while improving image quality: The case for innovation. *J Nucl Cardiol*. 2016;23(5):1080-1085.

81. Demas BE, Heelan RT, Lane J, Marcove R, Hajdu S, Brennan MF. Soft-tissue sarcomas of the extremities: comparison of MR and CT in determining the extent of disease. *Am J Roentgenol*. 1988;150(3):615-620.

82. Yuh EL, Barkovich AJ, Gupta N. Imaging of ependymomas: MRI and CT. *Child’s Nerv Syst*. 2009;25(10):1203-1213.

83. Huang S-H, Chien C-Y, Lin W-C, et al. A comparative study of fused FDG PET/MRI, PET/CT, MRI, and CT imaging for assessing surrounding tissue invasion of advanced buccal squamous cell carcinoma. *Clin Nucl Med*. 2011;36(7):518-525.

84. Shao Y, Cherry SR, Farahani K, et al. Development of a PET detector system compatible with MRI/NMR systems. *IEEE Trans Nucl Sci*. 1997;44(3):1167-1171.

85. Garlick PB, Marsden PK, Cave AC, et al. PET and NMR dual acquisition (PANDA): applications to isolated, perfused rat hearts. *NMR Biomed*. 1997;10(3):138-142.

86. Shao Y, Cherry SR, Farahani K, et al. Simultaneous PET and MR imaging. *Phys Med Biol*. 1997;42(10):1965.

87. Catana C, Wu Y, Judenhofer MS, Qi J, Pichler BJ, Cherry SR. Simultaneous acquisition of multislice PET and MR images: initial results with a MR-compatible PET scanner. *J Nucl Med*. 2006;47(12):1968-1976.

88. Raylman RR, Majewski S, Lemieux SK, et al. Simultaneous MRI and PET imaging of a rat brain. *Phys Med Biol*. 2006;51(24):6371.

89. Yamamoto S, Hatazawa J, Imaizumi M, et al. A multi-slice dual layer MR-compatible animal PET system. *IEEE Trans Nucl Sci*. 2009;56(5):2706-2713.

90. Raylman RR, Majewski S, Velan SS, et al. Simultaneous acquisition of magnetic resonance spectroscopy (MRS) data and positron emission tomography (PET) images with a prototype MR-compatible, small animal PET imager. *J Magn Reson*. 2007;186(2):305-310.

91. Gilbert KM, Handler WB, Scholl TJ, Odegaard JW, Chronik BA. Design of field-cycled magnetic resonance systems for small animal imaging. *Phys Med Biol*. 2006;51(11):2825.

92. Lucas AJ, Hawkes RC, Ansorge RE, et al. Development of a Combined microPET®-MR System. *Technol Cancer Res Treat*. 2006;5(4):337-341.

93. Grazioso R, Zhang N, Corbeil J, et al. APD-based PET detector for simultaneous PET/MR imaging. *Nucl Instruments Methods Phys Res Sect A Accel Spectrometers, Detect Assoc Equip*. 2006;569(2):301-305.

94. Buzhan P, Dolgoshein B, Filatov L, et al. Silicon photomultiplier and its possible applications. *Nucl Instruments Methods Phys Res Sect A Accel Spectrometers, Detect Assoc Equip*. 2003;504(1-3):48-52.

95. Pichler BJ, Judenhofer MS, Catana C, et al. Performance test of an LSO-APD detector in a 7-T MRI scanner for simultaneous PET/MRI. *J Nucl Med*. 2006;47(4):639-647.

96. Judenhofer MS, Catana C, Swann BK, et al. PET/MR images acquired with a compact MR-compatible PET detector in a 7-T magnet. *Radiology*. 2007;244(3):807-814.

97. Woody C, Schlyer D, Vaska P, et al. Preliminary studies of a simultaneous PET/MRI scanner based on the RatCAP small animal tomograph. *Nucl Instruments Methods Phys Res Sect A Accel Spectrometers, Detect Assoc Equip*. 2007;571(1):102-105.

98. Schulz V, Weisslerl B, Gebhardl P, et al. SiPM based preclinical PET / MR Insert for a human 3 T MR : first imaging experiments. *IEEE Nucl Sci Symp Med Imaging Conf Rec*. 2011:4467-4469.

99. Delso G, F\urst S, Jakoby B, et al. Performance measurements of the Siemens mMR integrated whole-body PET/MR scanner. *J Nucl Med*. 2011;52(12):1914-1922.

100. Levin CS, Maramraju SH, Khalighi MM, Deller TW, Delso G, Jansen F. Design features and mutual compatibility studies of the time-of-flight PET capable GE SIGNA PET/MR System. 2016.

101. Parker RP, Hobday PA, Cassell KJ. The direct use of CT numbers in radiotherapy dosage calculations for inhomogeneous media. *Phys Med Biol*. 1979;24(4):802-809.

102. Schlegel W. IF YOU CAN'T SEE IT, YOU CAN MISS IT: THE ROLE OF BIOMEDICAL IMAGING IN RADIATION ONCOLOGY. *Radiat Prot Dosimetry*. March 2010.

103. Ahn PH, Garg MK. Positron Emission Tomography/Computed Tomography for Target Delineation in Head and Neck Cancers. *Semin Nucl Med*. 2008;38(2):141-148.

104. Mak D, Corry J, Lau E, Rischin D, Hicks RJ. Role of FDG-PET/CT in staging and follow-up of head and neck squamous cell carcinoma. *Q J Nucl Med Mol imaging Off Publ Ital Assoc Nucl Med [and] Int Assoc Radiopharmacol (IAR), [and] Sect Soc of*. 2011;55(5):487-499.

105. Simpson DR, Lawson JD, Nath SK, Rose BS, Mundt AJ, Mell LK. Utilization of Advanced Imaging Technologies for Target Delineation in Radiation Oncology. *J Am Coll Radiol*. 2009;6(12):876-883.

106. Dirix P, Haustermans K, Vandecaveye V. The Value of Magnetic Resonance Imaging for Radiotherapy Planning. *Semin Radiat Oncol*. 2014;24(3):151-159.

107. Pinkawa M, Piroth MD, Holy R, et al. Dose-escalation using intensity-modulated radiotherapy for prostate cancer - evaluation of quality of life with and without 18F-choline PET-CT detected simultaneous integrated boost. *Radiat Oncol*. 2012;7(1):14.

108. De Ruysscher D, Wanders S, Minken A, et al. Effects of radiotherapy planning with a dedicated combined PET-CT-simulator of patients with non-small cell lung cancer on dose limiting normal tissues and radiation dose-escalation: A planning study. *Radiother Oncol*. 2005;77(1):5-10.

109. Keall PJ, Mageras GS, Balter JM, et al. The management of respiratory motion in radiation oncology report of AAPM Task Group 76a). *Med Phys*. 2006;33(10).

110. Lagerwaard FJ, Van Sornsen de Koste JR, Nijssen-Visser MRJ, et al. Multiple “slow” CT scans for incorporating lung tumor mobility in radiotheraphy planning. *Int J Radiat Oncol*. 2001;51(4):932-937.

111. van Sörnsen de Koste JR, Lagerwaard FJ, Schuchhard-Schipper RH, et al. Dosimetric consequences of tumor mobility in radiotherapy of stage I non-small cell lung cancer – an analysis of data generated using “slow” CT scans. *Radiother Oncol*. 2001;61(1):93-99.

112. van Sörnsen de Koste JR, Lagerwaard FJ, de Boer HC., Nijssen-Visser MR., Senan S. Are multiple CT scans required for planning curative radiotherapy in lung tumors of the lower lobe? *Int J Radiat Oncol*. 2003;55(5):1394-1399.

113. Hughes S, McClelland J, Chandler A, et al. A comparison of internal target volume definition by limited four-dimensional computed tomography, the addition of patient-specific margins, or the addition of generic margins when planning radical radiotherapy for lymph node-positive non-small cell lung. *Clin Oncol (R Coll Radiol)*. 2008;20(4):293-300.

114. Rietzel E, Pan T, Chen GTY. Four-dimensional computed tomography: Image formation and clinical protocol. *Med Phys*. 2005;32(4).

115. Rietzel E, Chen GTY, Choi NC, Willet CG. Four-dimensional image-based treatment planning: Target volume segmentation and dose calculation in the presence of respiratory motion. *Int J Radiat Oncol Biol Phys*. 2005;61(5):1535-1550.

116. Mageras GS, Pevsner A, Yorke ED, et al. Measurement of lung tumor motion using respiration-correlated CT. *Int J Radiat Oncol Biol Phys*. 2004;60(3):933-941.

117. Keall PJ, Starkschall G, Shukla H, et al. Acquiring 4D thoracic CT scans using a multislice helical method. *Phys Med Biol*. 2004;49(10):2053.

118. Paling MR, Brookeman JR. Respiration artifacts in MR imaging: reduction by breath holding. *J Comput Assist Tomogr*. 1986;10(6):1080-1082.

119. Perkins ND. Integrating cell-signalling pathways with NF-kappaB and IKK function. *Nat Rev Mol Cell Biol*. 2007.

120. Feinberg DA, Rofsky NM, Johnson G. Multiple breath-hold averaging (MBA) method for increased SNR in abdominal MRI. *Magn Reson Med*. 1995;34(6):905-909.

121. Prato FS, Nicholson RL, King M, et al. Abolition of respiratory movement markedly improved NMR images of the thorax and upper abdomen. In: *MAGNETIC RESONANCE IN MEDICINE*. Vol 1. ; 1984:227-229.

122. Runge VM, Clanton JA, Partain CL, A E James J. Respiratory gating in magnetic resonance imaging at 0.5 Tesla. *Radiology*. 1984;151(2):521-523.

123. Plathow C, Schoebinger M, Fink C, et al. Quantification of Lung Tumor Volume and Rotation at 3D Dynamic Parallel MR Imaging with View Sharing: Preliminary Results. *Radiology*. 2006;240(2):537-545.

124. von Siebenthal M, Székely G, Gamper U, Boesiger P, Lomax A, Cattin P. 4D MR imaging of respiratory organ motion and its variability. *Phys Med Biol*. 2007;52(6):1547.

125. von Siebenthal M, Cattin P, Gamper U, Lomax A, Székely G. 4D MR imaging using internal respiratory gating. In: *Medical Image Computing and Computer-Assisted Intervention--MICCAI 2005*. Springer; 2005:336-343.

126. Tokuda J, Morikawa S, Haque HA, et al. Adaptive 4D MR imaging using navigator-based respiratory signal for MRI-guided therapy. *Magn Reson Med*. 2008;59(5):1051-1061.

127. Cai J, Chang Z, Wang Z, Paul Segars W, Yin F-F. Four-dimensional magnetic resonance imaging (4D-MRI) using image-based respiratory surrogate: A feasibility study. *Med Phys*. 2011;38(12).

128. Townsend DW, Nutt R. Combined PET and X-ray CT tomograph and method for using same. December 2002.

129. Heusch P, Nensa F, Schaarschmidt B, et al. Diagnostic accuracy of whole-body PET/MRI and whole-body PET/CT for TNM staging in oncology. *Eur J Nucl Med Mol Imaging*. 2015;42(1):42-48.

130. Fraum TJ, Fowler KJ, McConathy J, et al. PET/MRI for the body imager: abdominal and pelvic oncologic applications. *Abdom Imaging*. 2015:1-18.

131. Beiderwellen K, Geraldo L, Ruhlmann V, et al. Accuracy of [18F]FDG PET/MRI for the Detection of Liver Metastases. *PLoS One*. 2015;10(9):e0137285.

132. Pevsner A, Nehmeh SA, Humm JL, Mageras GS, Erdi YE. Effect of motion on tracer activity determination in CT attenuation corrected PET images: a lung phantom study. *Med Phys*. 2005;32(7):2358-2362.

133. Nehmeh SA, Erdi YE, Rosenzweig KE, et al. Reduction of respiratory motion artifacts in PET imaging of lung cancer by respiratory correlated dynamic PET: methodology and comparison with respiratory gated PET. *J Nucl Med*. 2003;44(10):1644-1648.

134. Jacobson MW, Fessler JA. Joint estimation of image and deformation parameters in tomographic image reconstruction. In: *Statistical Signal Processing, 2003 IEEE Workshop on*. IEEE; 2003:162-165.

135. Fin L, Bailly P, Daouk J, Meyer M-E. Motion correction based on an appropriate system matrix for statistical reconstruction of respiratory-correlated PET acquisitions. *Comput Methods Programs Biomed*. 2009;96(3):e1-e9.

136. Lamare F, Carbayo MJL, Cresson T, et al. List-mode-based reconstruction for respiratory motion correction in PET using non-rigid body transformations. *Phys Med Biol*. 2007;52(17):5187.

137. Qiao F, Pan T, Clark Jr JW, Mawlawi OR. A motion-incorporated reconstruction method for gated PET studies. *Phys Med Biol*. 2006;51(15):3769.

138. Lamare F, Cresson T, Savean J, Le Rest CC, Reader AJ, Visvikis D. Respiratory motion correction for PET oncology applications using affine transformation of list mode data. *Phys Med Biol*. 2006;52(1):121.

139. Bloomfield PM, Spinks TJ, Reed J, et al. The design and implementation of a motion correction scheme for neurological PET. *Phys Med Biol*. 2003;48(8):959.

140. Fulton R, Tellmann L, Pietrzyk U, et al. Accuracy of motion correction methods for pet brain imaging. In: *Nuclear Science Symposium Conference Record, 2004 IEEE*. Vol 7. IEEE; 2004:4226-4230.

141. Bai W, Brady M. Regularized B-spline deformable registration for respiratory motion correction in PET images. *Phys Med Biol*. 2009;54(9):2719.

142. Dawood M, Lang N, Jiang X, Schafers KP. Lung motion correction on respiratory gated 3-D PET/CT images. *IEEE Trans Med Imaging*. 2006;25(4):476-485.

143. Dawood M, Buther F, Jiang X, Schafers KP. Respiratory motion correction in 3-D PET data with advanced optical flow algorithms. *IEEE Trans Med Imaging*. 2008;27(8):1164-1175.

144. Aklan B, Paulus DH, Wenkel E, et al. Toward simultaneous PET/MR breast imaging: systematic evaluation and integration of a radiofrequency breast coil. *MedPhys*. 2013;40(2):24301.

145. Tavallaei MA, Johnson PM, Liu J, Drangova M. Design and evaluation of an MRI-compatible linear motion stage. *Med Phys*. 2016;43(1):62-71.

Chapter 2

2 A Comparison of Megavoltage, Dual-energy, and Single-energy CT-based μ-maps for a 4 Channel Breast Coil in PET/MRI

Women with an increased average breast tissue density as assessed by x-ray mammography have been found to also have an increased risk for breast cancer.[1-33] This emphasizes the need for alternate imaging modalities that are not as susceptible to the attenuating effects of dense breast tissue for high-risk patients. PET/MRI combines anatomical and functional information within the same scan and could help with early detection in high-risk patients by using multispectral higher resolution MRI with higher sensitivity unispectral PET. However, the radiofrequency (RF) breast coil used for receiving signal during breast imaging with MRI attenuates the 511 keV PET photons. To correct for this, a mapping of electron densities (μ-map) of the RF breast coil must be created and incorporated into the PET reconstruction process.

This emphasizes the need for alternate imaging modalities that are not as susceptible to the attenuating effects of dense breast tissue for high-risk patients. PET/MRI combines anatomical and functional information within the same scan and could help with early detection in high-risk patients by using multispectral higher resolution MRI with higher sensitivity unispectral PET. However, the radiofrequency (RF) breast coil used for receiving signal during breast imaging with MRI attenuates the 511 keV PET photons. To correct for this, a mapping of electron densities (μ-map) of the RF breast coil must be created and incorporated into the PET reconstruction process.

Previous work to correct MR hardware attenuation in PET has been primarily based on CT imaging in the 50-100 kV range.[4-8] These methods are capable of producing high resolution images based on the electron densities of the hardware materials, which are then converted into mappings of narrow beam attenuation coefficients (NBACs). However, imaging metal components of hardware in the kV range often results in metal artifacts.[9] These along with under sampling artifacts can compromise the accuracy of the resulting μ-map and PET reconstruction. To reduce the appearance of such metal artifacts, some have used lower resolution ^{68}Ge transmission scans as a reference to the CT,[4] while others have used a threshold of NBACs in the CT-derived μ-map.[5,8] In the absence of a ^{68}Ge transmission scanner and in the interest of mapping all hardware components without artifacts, these methods are not accessible to most users.

Work has also been done with imaging materials that have high atomic numbers using dual-energy CT (DECT) or a cobalt source. It has been shown that beam-hardening artifacts, resulting from high-density material attenuating low energy photons in a polychromatic x-ray beam, can be reduced by using virtual monochromatic image reconstruction from DECT.[10-12] It has also been shown that the higher energy photons (1.25 MeV) are not susceptible to photoelectric effect but instead fall in the range for Compton scattering, providing images that are free from the artifacts produced in the kV energy range.[13] Further that the megavoltage CT (MVCT) method produces a linear relationship between the Hounsfield values of the imaging volumes and the density of materials in those volumes.[14]

Here, I propose either of two methods by which measurements of MRI hardware attenuation can be acquired using a virtual monochromatic image calculated from a DECT, or by using a 6 MV linear accelerator that has been detuned for imaging with a mean photon energy of 1.0 MV. Either of these measurements (DECT or MVCT) can be converted into a mapping of 511 keV NBACs for use in PET/MRI. I then investigate the performance of these methods against a previously proposed method using single energy CT (SECT).

2.1 Materials and Methods

2.1.1 Hybrid PET-MRI System

All imaging was performed on a Biograph mMR whole-body hybrid PET/MRI scanner. (Siemens Healthcare, Erlangen, Germany).[15] The integrated PET detector assembly is located between the RF and gradient coils. It is made up of 448 detector blocks (arranged into 8 rings of 56) 59.4 cm in diameter, 25.8 cm in length, and shares the same isocenter as the magnet system. Each detector block is composed of an 8×8 array of lutetium oxyorthosilicate (LSO) crystals fixed to a 3×3 array of water-cooled Avalanche photodiodes (APDs). The magnet system of the mMR is a 3 Tesla superconducting magnet with a 60 cm bore and 199 cm from front cover to back (actual magnet length is 163 cm). The whole-body gradient coil system has a maximum strength of 45 mT/m and slew rate of 200 T/m/s. In addition to the integrated RF body coil, there are various other RF coils provided with the mMR that have been designed for simultaneous acquisition with PET.

RF coils that do not have a fixed position in relation to the patient table are designed to be nearly PET transparent by optimizing geometries and materials. For RF coils that have a rigid construction and are fixed to the patient table, μ-maps are created and incorporated into the reconstruction process. In this work, I evaluate and compare three μ-map construction methods for a dedicated MR breast coil (rigid and fixed) during simultaneous acquisition of PET and MRI.

2.1.2 Four-channel RF Breast Coil

The breast coil used in this study was the MR-BI320-PA (Noras MRI Products GmbH, Würzburg, Germany) (Figure 2-1).[5] It has a two-channel patient pad coil, on which the patient lies prone. The padding of the pad coil is made of polyethylene foam with a polyurethane “skinfoam” coating. This pad coil lies directly on top of the all fiberglass frame, which also contains a two-channel insert plate coil. The plate coil locks into the base of the frame at bed level. The pad coil and plate coil form a high resolution, 4-channel phased array configuration, allowing the use of integrated parallel acquisition technique (iPAT) in the anterior–posterior and left–right directions with an acceleration factor of R = 2. The design of the frame has open sides to allow insertion of the breast immobilization and biopsy system, as well as simultaneous basic imaging of both breasts in all directions. The spine coil is removed from the patient table and the breast coil is held in position on the scanner bed using a polycarbonate fixation plate, which was fabricated in-house.

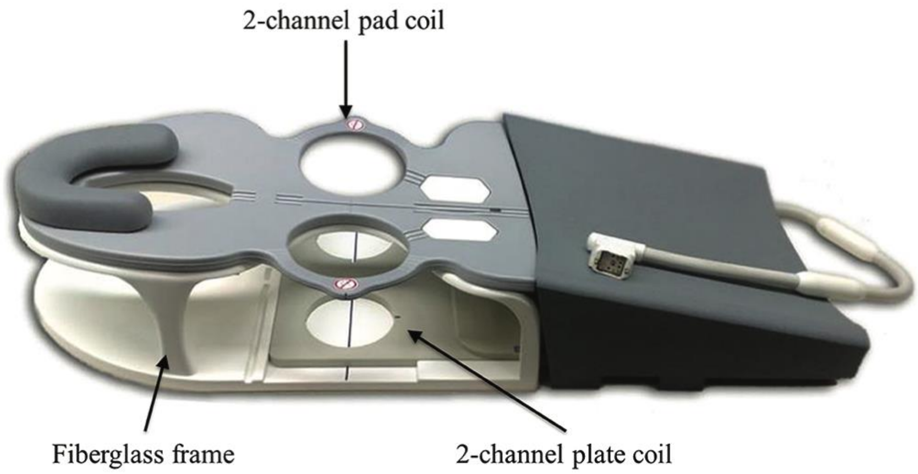

Figure 2-1: The MR-BI320-PA four-channel breast coil assembly with 2-channel pad coil on top and 2-channel insert plate coil, located in the lower part of the all fiberglass frame.

2.1.3 Breast Phantoms

To quantitatively and qualitatively evaluate the performance of each hardware μ-map construction method, a PET/MR breast phantom was fabricated. Previous work with the MR-BI320-PA four-channel breast coil has shown that it performed well in both an MR-only breast phantom and breast cancer patient imaging, providing good MR image quality.[5] In our study, I are primarily interested in evaluating μ-map performances in AC-PET reconstructions; therefore our phantom was designed with mainly PET in mind. The phantom consists of two tapered cylindrical compartments made of polypropylene. Each compartment of 946 ml can be filled with liquid solutions of MR-phantom doping agents and radiotracer to be imaged with both PET and MRI simultaneously.

A breast phantom fixture was designed and made from polystyrene rigid foam to position each breast phantom cylinder within the four-channel breast coil, to provide specific and repeatable positioning with minimal PET attenuation: Figure 2-2(A). To ensure identical positioning of the breast phantom on the patient table in the absence of the breast coil, a polystyrene rigid foam replica of the breast coil frame base and insert coil assembly was also designed and fabricated: Figure 2-2(B). Experimental setup including the breast coil is shown in Figure 2-2(A) and without the breast coil in Figure 2-2(B) for our control reference.

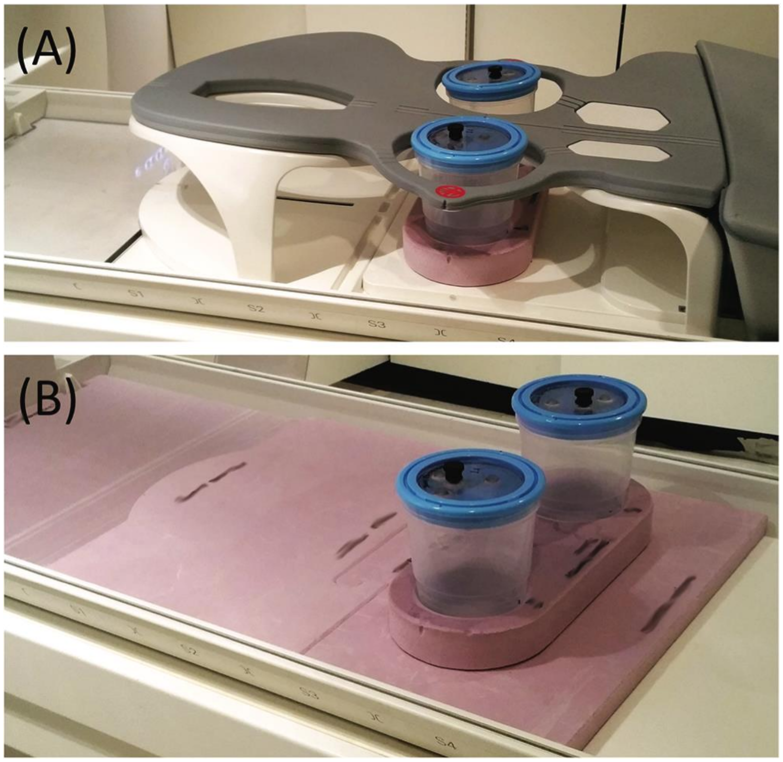

Figure 2-2: Experimental setups. (A) Setup for acquisition in the presence of the RF breast coil with two breast phantoms positioned within the coil using a polystyrene rigid foam fixture made in- house. (B) Setup for acquisition without the breast coil present. A replica of the breast coil base was made to position the breast phantoms identical to their position within the breast coil.

2.1.4 Attenuation Correction

In a clinical PET/MR breast scan, PET photons are attenuated by materials along the way to detectors. These materials include the various components of MR hardware within the field of view (FoV), including the accessory breast coil and patient table, in addition to the patient themselves. To ensure quantitative accuracy of PET images, all attenuating materials within the FoV must be accounted for, and corrected. Currently, MR hardware attenuation is corrected with μ-maps created from CT scans, which map the spatial distribution of different hardware materials and their respective NBACs. I evaluated the performance of three CT-based models for MR hardware µ-map construction: (1) SECT, (2) DECT, and (3) MVCT. All CT scans were acquired with the four-channel breast coil, including the frame, the pad coil, and the insert coil, as well as the fixation plate present. The patient table of each CT scanner was removed from all images by manually cropping volumes with 3D Slicer's Crop Volume module.[16] For each of the three breast coil µ-maps, PET reconstructions were performed offline using Siemens' PET reconstruction software, e7 tools (Siemens Molecular Imaging, Knoxville, USA). Attenuation correction of the PET/MR patient table is automatically applied during the PET reconstruction process, using a CT-based µ-map that is provided with the PET/MR system.

2.1.4.1 SECT-based Model

The SECT scan was performed on a Philips Brilliance CT Big Bore (Philips Healthcare, Cleveland, OH). The system used a peak tube voltage of 120 kVp, a tube current of 379 mA, and a calculated effective energy of 76 keV. The reconstructed image volume had voxel dimensions of $1.2\times1.2\times1.0\ \text{mm}^3$, and a matrix size of 512×512×892. A 2 mm Gaussian filter was applied to the CT image volume and a bilinear function was used to convert Hounsfield unit (HU) values into attenuation coefficients for 511 keV photons, using code written in house with Matlab v9.0 (The MathWorks, MA USA).[17] The bilinear function is based on NBACs for H_2O and cortical bone, calculated from tables published by Hubbell and Seltzer.[18] The values used for the above-mentioned conversion for an effective energy of 76 keV were $0.1868\ \text{cm}^{-1}$ and $0.4468\ \text{cm}^{-1}$ for H_2O and cortical bone, respectively. To match the spatial resolution required for the hardware µ-map, our SECT-based µ-map was resampled using 3D Slicer's Resample Image (BRAINS) module.[16] To reduce the effects of image artifacts in the µ-map due to high atomic number components, such as metal in the electronics, a threshold was applied to the NBACs between 0.02 and $0.12\ \text{cm}^{-1}$ for 511 keV photons, as proposed by Aklan *et al* 2013.[5,7,8]

2.1.4.2 DECT-based Model

A DECT scan of the breast coil assembly was acquired on a GE Healthcare Discovery CT750 HD scanner (GE Healthcare, Waukesha, WI, USA).[11] This system uses a single tube that is capable of rapidly switching between two tube potentials (80 kVp and 140 kVp) every 0.2 milliseconds. A simulated monochromatic image volume at 100 keV was calculated from the two sets of SECT images to reduce beam-hardening artifact from the metal components of the RF coil. This was accomplished using a method described by So *et al* 2011.[11] The simulated monochromatic image volume had voxel dimensions of $0.98\times0.98\times5.0\ \text{mm}^3$, and a matrix size of 512×512×360. A 2 mm Gaussian filter was applied to the µ-map and, similarly to the method used for the SECT-based µ-map, a bilinear function was used to convert HU values into attenuation coefficients for 511 keV photons, using code written in house with Matlab v9.0 (The MathWorks, MA USA).[17] The values used for this conversion at 100 keV were $0.1707\ \text{cm}^{-1}$ and $0.3562\ \text{cm}^{-1}$ for H_2O and cortical bone, respectively. The DECT-based µ-map was resampled to match the spatial resolution required for the hardware µ-map, using 3D Slicer's Resample Image (BRAINS) module,1[6] and the same NBACs threshold as used for the SECT maps was applied (between 0.02 and $0.12\ \text{cm}^{-1}$) to reduce the effects of noise and any remaining metal artifacts in the image.[5,7,8]

2.1.4.3 MVCT-based Model

MVCT images were acquired on a TomoTherapy Hi-Art linear accelerator (TomoTherapy, Madison, WI, USA).[19] The Hi-Art has a 6 MV linear accelerator mounted on a CT type ring gantry, which also allows the acquisition of MVCT images using the same radiation source while detuned to an average energy of 1.0 MV. Before acquiring MVCT images of the breast coil, a calibration scan was performed to calculate the relative electron density to HU value curve for the MVCT beam energies used on the Hi-Art. A cylindrical solid water phantom with holes for placing plugs for CT density tests called a 'cheese' phantom (Gammex RMI, Middelton, WI, USA) was used. Three plugs were made of three different materials with high atomic numbers, similar to components found in the breast coil. The materials used were aluminum (6061 T6), copper (C110), and stainless steel (304). The plugs were placed in the cheese phantom along with several other plugs of varying densities (Figure 2-3) and MVCT images were taken of the phantom. These images were then used to plot a linear relationship between the relative electron density of the materials and their corresponding Hounsfield values. The dimensions of the breast coil were greater than the High-Art's FoV of 40 cm, therefore two separate images had to be taken. One image was taken with the breast coil positioned slightly to the right of the patient table and then another with it positioned slightly to the left. Each of the reconstructed image volumes had voxel dimensions of 0.763×0.763×4.0 mm^3, and a matrix size of 512×512×245. Translation of the images into their appropriate overlapping positions was performed manually using 3D Slicer.[16] Fusion of the images was performed in Matlab with in-house code. The resulting image volume was then translated into the required position relative to the bed with 3D Slicer's registration module.[16] The relative electron densities of the breast coil materials were calculated from the HU values obtained in the MV image volume and the newly calibrated relative electron density curve calculated from the calibration scan. NBACs were then calculated for 511 keV photons from the relative electron density map, to create the MVCT-based μ-map. A 2 mm Gaussian filter was applied to the μ-map and it was resampled to match the spatial resolution required for the hardware μ-map.

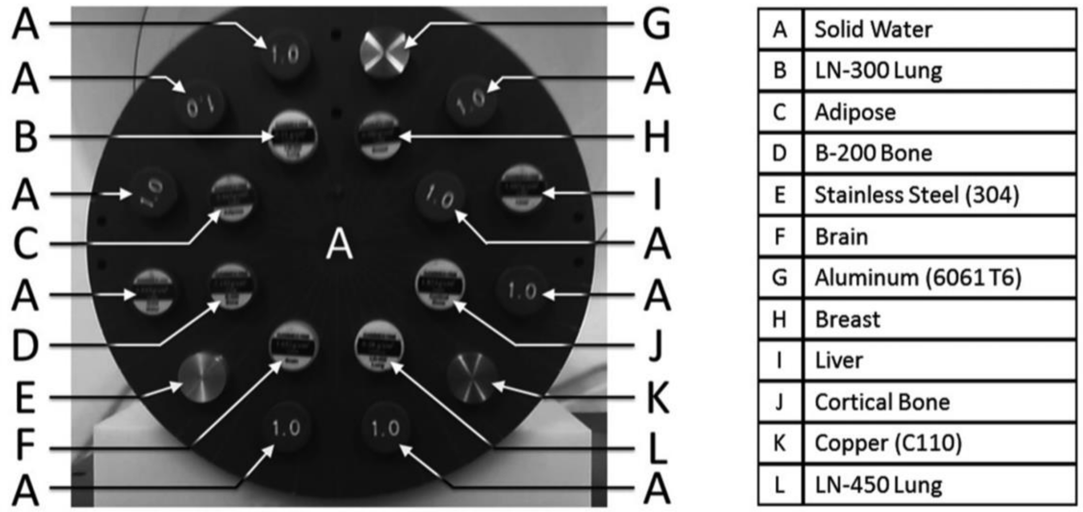

A	Solid Water
B	LN-300 Lung
C	Adipose
D	B-200 Bone
E	Stainless Steel (304)
F	Brain
G	Aluminum (6061 T6)
H	Breast
I	Liver
J	Cortical Bone
K	Copper (C110)
L	LN-450 Lung

Figure 2-3: Cylindrical solid water 'cheese' phantom (Gammex RMI, Middleton, WI, USA) with eight tissue-simulating plugs and three plugs made in-house: A) aluminum, B) copper, and C) stainless steel.

2.1.5 PET Acquisition

Two separate PET datasets were acquired to evaluate and compare the performance of the three different CT-based µ-maps: 1) With the breast coil, 2) Without the breast coil (used as reference standard). PET data from the second acquisition was corrected for physical decay.

A fixture made of polystyrene rigid foam was used in the first PET acquisition to achieve identical positioning of the breast phantoms to the second set of acquisitions with the breast coil in place. For both acquisitions, each breast phantom contained distilled water with approximately 27 kBq/L of ^{18}F. The breast phantoms were then placed in the same table location (with and without breast coil) and positioned at the isocenter of the PET FoV where emission data was collected for 40 minutes.

All PET reconstructions were performed using the Ordinary-Poisson Ordered Subsets Expectation Maximization (3D-OP-OSEM) algorithm[20] (3 iterations, 21 subsets, and 2 mm Gaussian filter). The resulting image volumes had: matrix size = 172×172, slices = 127, and voxel size = 4.0×4.0×2.0 mm^3. The manufacturer's reconstruction software provided scatter correction for all PET image reconstructions.

Attenuation of the breast coil and breast phantoms was corrected with each of the three CT-based µ-maps in separate reconstructions (Table 2-1). Five different reconstruction scenarios were carried out: 1) the acquisition in the presence of the breast coil, but without correcting for the breast coil's attenuation (PET_NAC). This reconstruction was used to measure the effects of the coil's attenuation. Using the same emission data from this first acquisition, the breast coil attenuation was corrected using the: 2) SECT-based µ-map (BC_AC_{SECT}) for the reconstruction PET_SECT, 3) DECT-based µ-map (BC_AC_{DECT}) for PET_DECT, and 4) MVCT-based µ-map (BC_AC_{MVCT}) for PET_MVCT. The second acquisition was in the absence of the breast coil where no µ-map was required for the breast coil (N/A). This reconstruction was used as our reference standard (PET_REF).

After each reconstruction, µ-maps for the patient table, breast coil, and phantom were visually examined for alignment (Figure 2-4).

Table 2-1: Summary of reconstruction scenarios carried out to evaluate both the attenuation of the breast coil and the three proposed CT-based methods to correct for MR hardware attenuation.

MR Hardware Setup	Attenuation Correction	PET Reconstruction
With Breast Coil	NAC	PET_NAC
	BC_AC$_{SECT}$	PET_SECT
	BC_AC$_{DECT}$	PET_DECT
	BC_AC$_{MVCT}$	PET_MVCT
No Breast Coil	N/A (reference standard)	PET_REF

Figure 2-4: Axial, coronal, and sagittal views of a µ-map composed of manufacturer's table µ-map, the SECT-based breast coil µ-map, and the phantom µ-map fused into a single volume.

Total true counts for both the acquisitions with the breast coil and without the breast coil were used to determine the total counts lost in the presence of the breast coil.

Relative differences of activity between the reference standard acquisition without the breast coil and each of the four reconstructions with the breast coil present were calculated. These images were used to evaluate the effect of the breast coil's presence on PET signal and the accuracy of each AC method. Five cylindrical regions of interest (ROIs), shown in Figure 2-5(A)-(B) were assigned within the breast phantom for each of the five reconstructions (PET_REF, PET_NAC, PET_SECT, PET_DECT, and PET_MVCT). The mean and standard deviation of all ROIs across the included transverse slices (slice 49 to 75) were calculated for each reconstruction and reported in terms of their percent difference from the reference standard.

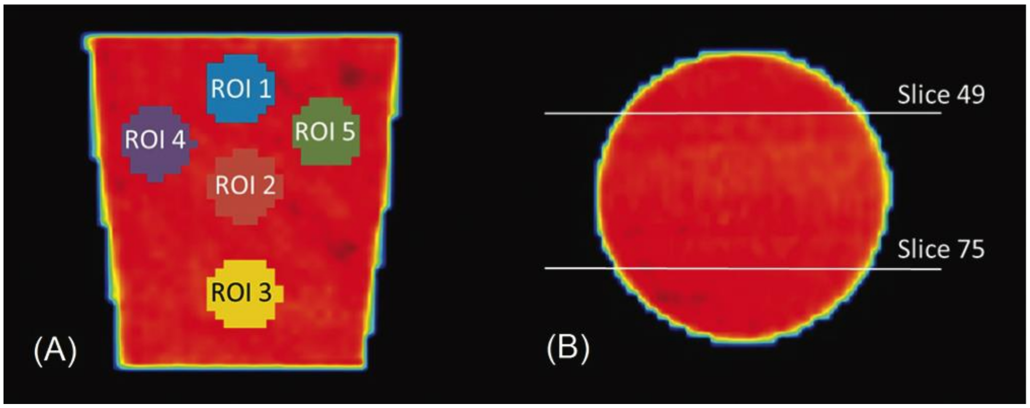

Figure 2-5: ROIs used to calculate relative percent difference images. (A) Axial view of breast phantom with ROIs. (B) Coronal view of breast phantom showing the range of transverse slices (49 – 75) used for plotting each ROI.

2.2 Results

Total true counts without the breast coil present were 3.33E+09 and in the presence of the breast coil was 3.002E+09. This made for a total loss of 9.9% from the breast coil attenuating PET photons.

Evidence of photon attenuation from the presence of the breast coil can be seen in a comparison of the PET_REF and PET_NAC reconstructions (Figure 2-6(A) and (B)), particularly in the lower-right region of the axial view and the left side of the sagittal view. This can also be observed in the relative difference image (Figure 2-7(A)). The reconstruction corrected with the BC_AC$_{SECT}$ μ-map (Figure 2-6(C)) shows an improvement of the lost signal in the lower-right region of the axial view but also shows some overcorrection in the left sides of the coronal and sagittal views. The reconstruction performed with the DECT-based AC (Figure 2-6(D)) shows less of the overcorrection observed in the Figure 2-6(C). Better still, the MVCT-based AC reconstruction (Figure 2-6(E)) bares the closest resemblance to the reference standard (Figure 2-6(A)), with most of the areas of lost activity recovered and regions of overcorrection reduced.

The relative difference images confirm the observations made in each of the PET reconstructions, with overall improvement in the amount of activity recovered with each of the three different µ-maps (Figure 2-7(B)-(D)) over the image without coil AC (Figure 2-7(A)). Common amongst all three AC reconstructions (Figure 2-6(C)-(E)) is overcorrection in the lower region of the breast phantom. This coincides with the area that showed the greatest decrease in activity (Figure 2-6(B)), due to its proximity to the breast coil's most attenuating components.

This is also seen in plot for the relative percent difference of ROIs between PET_REF and PET_NAC (Figure 2-8(C)). ROI 3 is positioned in the lower portion of the breast phantom (Figure 2-8(A)), and the attenuating effects of the breast coil are greater there than in the ROIs positioned higher in the phantom (ROI 1, ROI 2, ROI 4, ROI 5). The overcorrection of this lower region can also be seen in each of the plots for the three CT-based reconstructions (Figure 2-8(D)-(F)). The ROI analysis also showed mean percent differences from the reference standard to be approximately -1% to -9% without correcting for the attenuation caused by the presence of the breast coil (

Table 2-2). Correcting for this attenuation showed approximate values of -2% to 7%, -3% to 6%, and -3% to 5% difference from the reference standard for the SECT-based, DECT-based, and MVCT-based corrections, respectively (

Table 2-2).

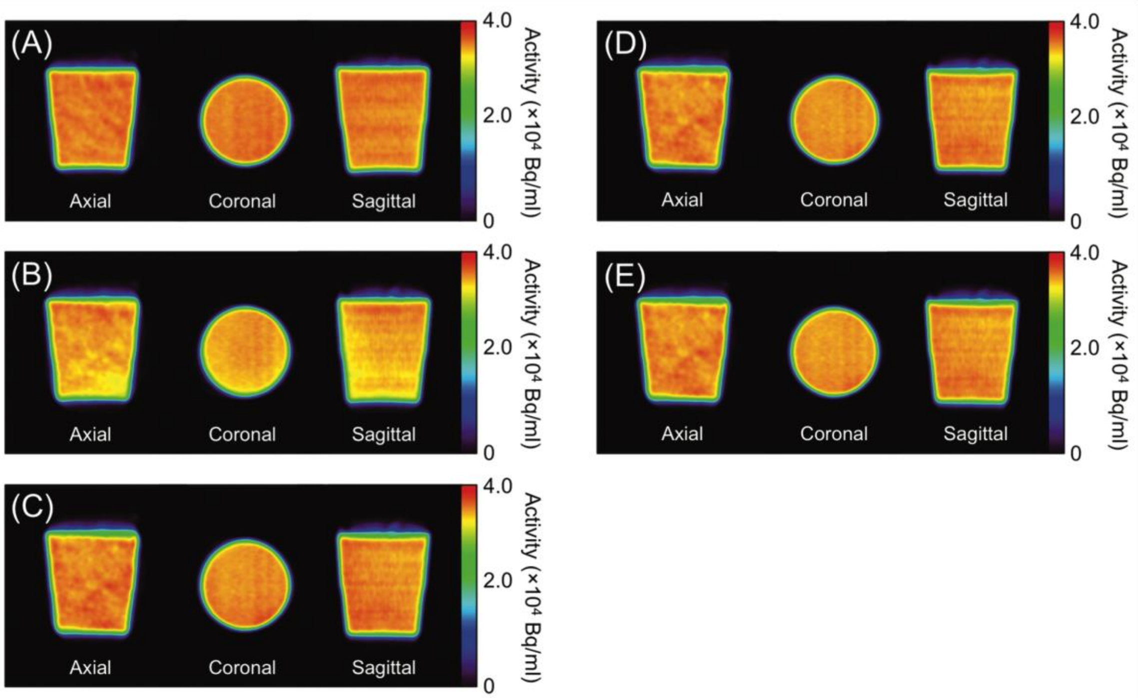

Figure 2-6: Breast phantom PET images in axial, coronal, and sagittal views for each reconstruction scenario. (A) Breast phantom only (PET_REF). (B) Breast phantom and breast coil without coil AC (PET_NAC). (C) Breast phantom with breast coil and SECT-based coil AC (PET_SECT). (D) Breast phantom with breast coil and DECT-based coil AC (PET_DECT). (E) Breast phantom with breast coil and MVCT-based coil AC.

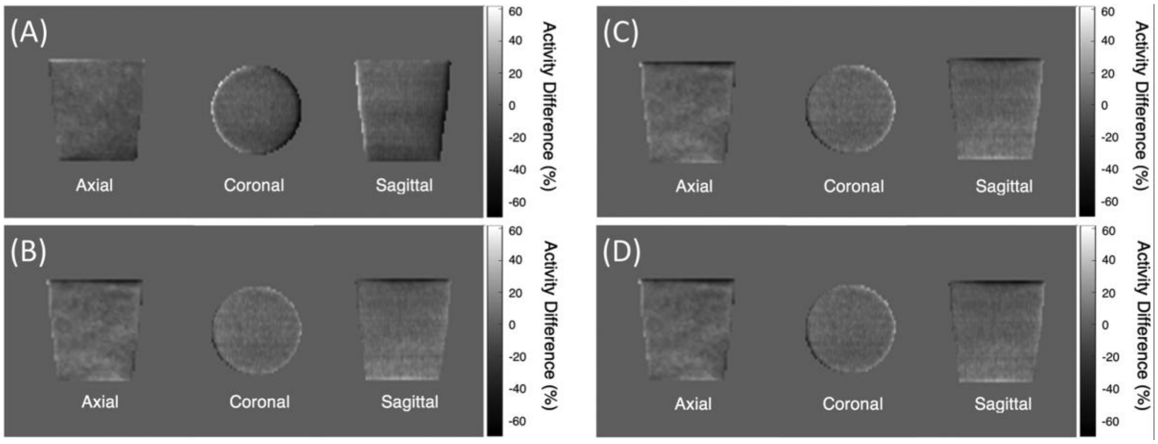

Figure 2-7: Relative difference of PET images measured in percent. (A) Relative difference between the reference standard (PET_REF) and with the breast coil but without coil AC (PET_NAC). (B) Relative difference between PET_REF and with breast coil and SECT-based AC. (C) Relative difference between PET_REF and with breast coil and DECT-based AC (PET_DECT). (D) Relative difference between PET_REF and with breast coil and MVCT-based AC (PET_MVCT).

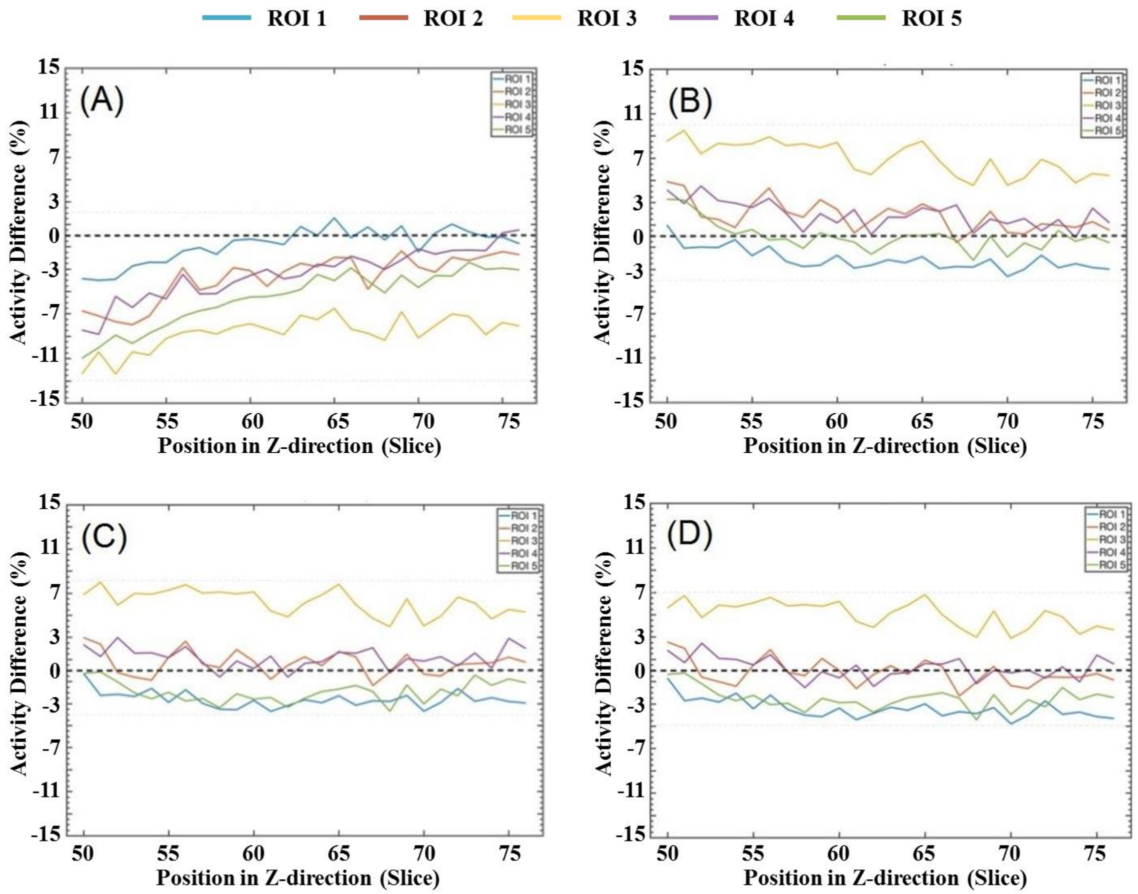

Figure 2-8: ROI comparison of relative percent difference images. Plots show the relative percent difference between mean ROI values for PET_REF vs. (A) PET_NAC, (B) PET_SECT, (C) PET_DECT, and (D) PET_MVCT.

Table 2-2: Mean and standard deviation of the percent activity difference calculated between the reference standard (PET_REF) and each of the four AC scenarios (PET_NAC, PET_SECT, PET_DECT, and PET_MVCT) performed on PET data collected in the presence of the breast coil.

	PET_NAC		PET_SECT		PET_DECT		PET_MVCT	
	Mean	SD	Mean	SD	Mean	SD	Mean	SD
ROI 1	-0.85	1.54	-2.10	1.01	-2.62	0.74	-3.41	0.87
ROI 2	-3.76	2.05	1.81	1.37	0.68	1.09	-0.19	1.16
ROI 3	-8.71	1.49	7.02	1.49	6.20	1.15	5.04	1.16
ROI 4	-3.44	2.32	1.95	1.19	1.18	0.94	0.25	0.98
ROI 5	-5.55	2.46	-0.04	1.29	-1.93	0.95	-2.52	0.96

2.3 Discussion

Both PET and MRI have been used extensively in oncology imaging due to the advantages of excellent specificity and sensitivity of PET and improved soft-tissue contrast of MRI over x-ray images. For this reason, hybrid PET/MRI shows great promise as a tool for early cancer detection in high-risk patients. Ensuring compatibility of MRI hardware, such as RF coils, with PET continues to be an active area of research and in this study I describe two CT-based μ-map construction methods and compare their performance with a method described in Aklan *et al.* (2013).[5] It was shown that both the DECT and MVCT-based μ-maps of the RF breast coil, when used during PET reconstruction, were capable of correcting for the breast coil's attenuation of PET photons. Both the DECT and MVCT-based methods performed comparably to the SECT-based method in recovering activity in the breast phantom, while showing less overcorrection in the more attenuated regions. This is clear when comparing the plotted values of ROI 3 for each of the percent difference plots in Figure 2-8. Similar differences between ROI regions are observed in Aklan *et al.* (2013).[5] Overcorrection or undercorrection is due to the combination of scatter correction and attenuation correction. Theoretically, if all scattered and random events are corrected for, then one should be able to reconstruct a (relative) quantitatively accurate reconstruction using narrow-beam attenuation coefficients.

However, if the projection data still contains counts that are not “trues”, using narrow-beam attenuation coefficients will over-correct, resulting in a reconstruction that has an increased count density in the middle compared with the perimeter. Conversely, if the provided scatter correction removes too many counts, the result is a photopenic effect.

The improvements observed in the DECT and MVCT-based correction methods were due to the reduction of metal artefacts in the CT images from which the µ-maps were derived, resulting in more accurate attenuation coefficients in the highly attenuation materials (Figure 2-9(A)-(F)). Although the virtual monochromatic images reconstructed from the DECT images showed a noticeable improvement over the SECT images, metal artifacts remained. This is due to projection truncation and/or photon starvation at lower energies of the two spectra. As a result, a similar set of thresholds were applied to the 511 keV NBACs of the DECT-based µ-map as were applied to the SECT-based µ-map in an attempt to reduce the effects of any remaining artefacts. However, the MVCT images did not contain any visible metal artefacts leading to an artefact-free µ-map. No thresholds were applied to the MVCT-based µ-map, given the significant reduction of visible artefacts.

Previous work by Aklan *et al.* (2013) on CT-based µ-map construction for MR hardware AC has shown that pre-acquired SECT-based µ-maps of the same breast coil used in this study allowed for AC of RF coil hardware components in PET data. Their phantom data shows an 11% loss in total true counts in the presence of the coil. ROI analysis showed the variation of mean values for relative difference images to go from 4%-16% to -4%-4%, for non-AC and AC images, respectively.[5] The feasibility of their approach to RF coil AC is also demonstrated with the PET/MR data of two breast cancer patients.[5] This SECT-based technique to RF coil AC has been similarly applied to other MR hardware components.[5,8,21,22] In our study, a breast phantom different from the one in Aklan *et al.* (2013) was used. As a result some of the PET activity values for our replication of this technique were different. However, using the same PET data for each of the AC techniques in this study limits the introduction of other variables that might contribute to the difference seen between techniques. Our results suggest that DECT and

MVCT-based μ-maps can provide improved quantitative accuracy in the more attenuated regions of PET data, which may otherwise see overcorrection with a SECT-based μ-map. This is due to metal artefact being less prominent in these two imaging techniques.

While the phantom used does not exhibit the same geometries as a patient, it was still able to provide a controlled model with which the various AC techniques could be evaluated and compared. Future work with a more biologically accurate phantom and/or patient data should be done to validate our DECT-based and MVCT-based RF coil AC techniques further.

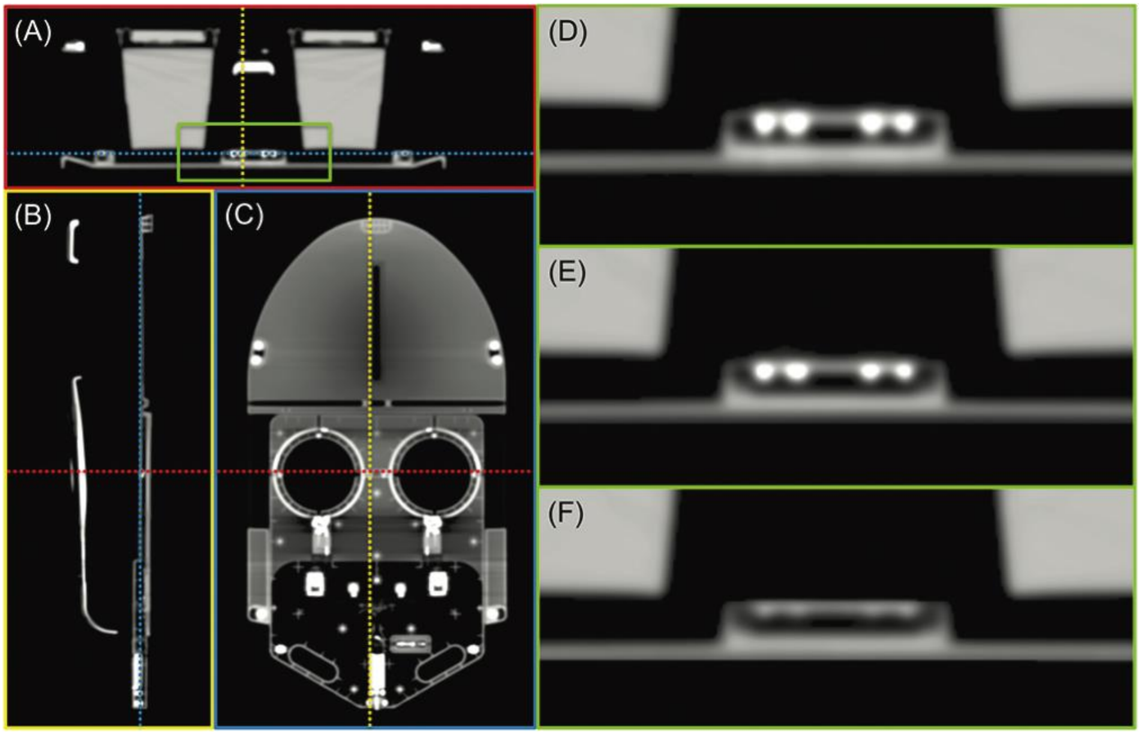

Figure 2-9: A comparison of high-density components in three different μ-maps. The SECT-based μ-map is shown in (A) Axial, (B) Sagittal, and (C) Coronal views. Dotted lines represent intersecting planes shown in frames outlined in matching color. A close-up of high density components in the breast coil (green rectangle in frame A) are shown in the (D) SECT-based μ-map, (E) the DECT-based μ-map, and (F) the MVCT-based μ-map.

2.4 Conclusions

The proposed DECT and MVCT-based μ-map construction techniques have been evaluated and compared with a previously used SECT-based technique in a breast phantom model. Both techniques provide a feasible approach to MR hardware AC for PET, while showing less overcorrection in the more highly attenuated regions of the phantom, than what was seen with the PET images corrected with the SECT-based μ-map. The DECT and MVCT images, from which the μ-maps were calculated, showed less metal artifact than the SECT images. Furthermore, the μ-map derived from the MVCT did not require any additional processing, whereas both the SECT and DECT-based μ-maps required the application of thresholds to mitigate the effects of metal artifacts. The application of our DECT-based and MVCT-based RF coil AC techniques for other system hardware components could also be of value in trying to improve the integration of MR imaging with quantitatively accurate PET.

2.5 References

1. Boyd NF, Byng JW, Jong RA, et al. Quantitative Classification of Mammographic Densities and Breast Cancer Risk: Results From the Canadian National Breast Screening Study. *J Natl Cancer Inst*. 1995;87(9):670-675.

2. Boyd NF, Guo H, Martin LJ, et al. Mammographic Density and the Risk and Detection of Breast Cancer. *N Engl J Med*. 2007;356(3):227-236.

3. Mandelson MT, Oestreicher N, Porter PL, et al. Breast density as a predictor of mammographic detection: comparison of interval- and screen-detected cancers. *J Natl Cancer Inst*. 2000;92(13):1081.

4. Delso G, Martinez-Moller A, Bundschuh RA, et al. Evaluation of the attenuation properties of MR equipment for its use in a whole-body PET/MR scanner. *Phys Med Biol*. 2010;55(15):4361-4374.

5. Aklan B, Paulus DH, Wenkel E, et al. Toward simultaneous PET/MR breast imaging: systematic evaluation and integration of a radiofrequency breast coil.

MedPhys. 2013;40(2):24301.

6. Kartmann R, Paulus DH, Braun H, et al. Integrated PET/MR imaging: Automatic attenuation correction of flexible RF coils. *MedPhys*. 2013;40(8):82301.

7. Eldib M, Bini J, Calcagno C, Robson PM, Mani V, Fayad ZA. Attenuation Correction for Flexible Magnetic Resonance Coils in Combined Magnetic Resonance/Positron Emission Tomography Imaging. *Invest Radiol*. 2014;49(2):63-69.

8. Fayad ME and JB and PMR and CC and DDF and CT and ZA. Markerless attenuation correction for carotid MRI surface receiver coils in combined PET/MR imaging. *Phys Med Biol*. 2015;60(12):4705.

9. Barrett JF, Keat N. Artifacts in CT: Recognition and Avoidance. *RadioGraphics*. 2004;24(6):1679-1691.

10. So A, Hsieh J, Imai Y, et al. Prospectively ECG-triggered rapid kV-switching dual-energy CT for quantitative imaging of myocardial perfusion. *JACC Cardiovasc Imaging*. 2012;5(8):829-836.

11. So A, Lee T-Y, Imai Y, et al. Quantitative myocardial perfusion imaging using rapid kVp switch dual-energy CT: Preliminary experience. *J Cardiovasc Comput Tomogr*. 2011;5(6):430-442.

12. So A, Hsieh J, Narayanan S, et al. Dual-energy CT and its potential use for quantitative myocardial CT perfusion. *J Cardiovasc Comput Tomogr*. 2012;6(5):308-317.

13. Schreiner LJ, Rogers M, Salomons G, Kerr A. Metal Artifact Suppression in Megavoltage Computed Tomography. *Proc SPIE*. 5745:637.

14. Rogers M, Kerr A, Salomons G, Schreiner LJ. Quantitative Investigations of Megavoltage Computed Tomography. Flynn MJ, ed. *Proc SPIE*. 2005;5745(613):685.

15. Delso G, F\urst S, Jakoby B, et al. Performance measurements of the Siemens mMR integrated whole-body PET/MR scanner. *J Nucl Med*. 2011;52(12):1914-1922.

16. Fedorov A, Beichel R, Kalpathy-Cramer J, et al. 3D Slicer as an Image Computing Platform for the Quantitative Imaging Network. *Magn Reson Imaging*. 2012;30(9):1323-1341.

17. Carney JPJ, Townsend DW, Rappoport V, Bendriem B. Method for transforming CT images for attenuation correction in PET/CT imaging. *Med Phys*. 2006;33(4).

18. Hubbell JH, Seltzer SM. *Tables of X-Ray Mass Attenuation Coefficients and Mass Energy-Absorption Coefficients 1 keV to 20 MeV for Elements Z= 1 to 92 and 48 Additional Substances of Dosimetric Interest*. National Inst. of Standards and Technology-PL, Gaithersburg, MD (United States). Ionizing Radiation Div.; 1995.

19. Yartsev S, Kron T, Van Dyk J. Tomotherapy as a tool in image-guided radiation therapy (IGRT): theoretical and technological aspects. *Biomed Imaging Interv J*. 2007;3(1):e16.

20. Comtat C, Bataille F, Michel C, et al. OSEM-3D reconstruction strategies for the ECAT HRRT. In: *Nuclear Science Symposium Conference Record, 2004 IEEE*. Vol 6. ; 2004:3492-3496.

21. Quick DHP and LT and HH. Towards improved hardware component attenuation correction in PET/MR hybrid imaging. *Phys Med Biol*. 2013;58(22):8021.

22. Oehmigen M, Lindemann ME, Lanz T, Kinner S, Quick HH. Integrated PET/MR breast cancer imaging: Attenuation correction and implementation of a 16-channel RF coil. *Med Phys*. 2016;43(8):4808-4820.

Chapter 3

3 Accuracy and Sensitivity of Respiratory-Triggered PET-MRI Evaluated Using a Multi-modality Motion Platform

The challenge of imaging in the presence of respiratory motion has necessitated various techniques to either mitigate the effects of[1-3] or measure motion.[4-6] These techniques are designed to facilitate patient diagnosis[7,8] and in some cases intervention guidance.[4-6] In the case of the latter, image-guided radiation therapy (IGRT) is an example of how both image accuracy and motion information are of great importance in the presence of respiratory motion.[9] As radiation therapy (RT) delivery systems evolve technologically, efforts to capitalize on these improvements by maximizing target dose and minimizing collateral dose to critical structures will be accomplished through increased planning target volume (PTV) conformality. To make this possible, the pre-treatment imaging must also evolve to incorporate optimal tissue contrast, molecular information, and motion characterization.

Although commonly used for RT planning, x-ray computed tomography (CT) suffers from poor soft-tissue contrast when compared to magnetic resonance imaging (MRI). MRI on the other hand provides superb soft-tissue contrast, but unlike CT, is unable to measure electron density directly; tissue electron density is required to calculate RT plans and for attenuation correction in molecular imaging (e.g. positron emission tomography (PET)).

Increased radiation dose to biologically active subregions of a tumour volume can be used to improve treatment outcomes. Positron Emission Tomography (PET) imaging of tumours can help provide the necessary target localization,[10] when combined with the appropriate anatomical reference image. Hybrid PET-MRI systems are becoming clinically available and allow molecular information from PET and anatomical information from MRI to be acquired in a single session.[11-13] Additionally, the true simultaneity of this hybrid system allows for better spatial correlation of the modalities than hybrid serial PET/CT systems.[14]

Currently, most imaging protocols require the patient to hold their breath during acquisition when respiratory motion is a concern. However, breath holds engage different muscles than free breathing, potentially resulting in a different tumour position than what would occur during a free breathing treatment delivery. If we are to use the additional information that can be provided by MRI and PET for the purposes of RT planning, patients will need to be free breathing during image acquisition.

MR imaging protocols to visualize lung tumours commonly include a free breathing acquisition, using a steady state gradient echo sequence (e.g. fast imaging with balanced steady state free precession (TrueFISP)) to visualize the extent of tumour motion, followed by the acquisition of a respiratory-triggered T2-weighted turbo spin echo (TSE) sequence (e.g. the periodically rotated overlapping parallel lines with enhanced reconstruction (PROPELLER) technique)[15] obtained at end exhalation to characterize tumour size and location. On a hybrid PET-MRI scanner, metabolic information about lung lesions can be acquired simultaneously with 18F-FDG PET. While these methods are commercially available, their accuracy – specifically related to the ability to minimize motion artefact – is not routinely verified, likely since no quality assurance phantom that verifies the accuracy of respiratory-triggered PET/MRI currently exists. The aim of this study is to evaluate the accuracy and PET sensitivity of respiratory-triggered PET-MRI protocols under controlled conditions. The effects of motion magnitude on accuracy and sensitivity are evaluated for a range of motion amplitudes and tumour sizes using a programmable PET-MR-CT compatible respiratory motion phantom with known tumour geometries and PET-tracer activity concentrations. This evaluation can serve as a platform for developing routine quality assurance procedures.

3.1 Materials and Methods

3.1.1 Phantom Design

A phantom was created to represent an average human torso with air cavities representing the lungs. The phantom (shown in Figure 3-1) is made up of five compartments, all of which are made of acrylic. The main torso compartment is a closed cylinder 285 mm long with an internal oval cross-section measuring 292 mm wide by 240.5 mm high. Contained within the torso compartment are three smaller cylinders running the full length of the torso – two 89 mm wide by 125.5 mm high compartments represent the lungs and a 32.3 mm wide by 23.6 mm high compartment can accommodate spine mimicking material. A 77 mm diameter opening in the superior end of the torso compartment allows it to be filled and emptied; a 10.7 mm diameter hole in the same end is used to fill/empty the spinal compartment. The two lung compartments are open at the inferior end of the torso to allow a lesion-mimicking compartments to move freely inside while attached to the MRI compatible motion stage.[16] Lesions were simulated with acrylic spheres affixed to acrylic stems. While various lesion sizes and shapes can be fabricated, I evaluated four "lesions" – 28 mm, 22 mm, 17 mm, and 10 mm internal diameters, similar to existing NEMA image quality phantoms.[17] The phantom design enables the non-lung cavities to be filled with liquids with varying x-ray/gamma attenuation, MRI properties, and radioactive PET tracers.

The phantom is designed for use in combination with the MRI compatible motion stage (section 3.1.2). The stem of each lesion compartment is attached to the motion stage with polystyrene extensions thereby allowing the lesion compartments to reach into the lung compartment of the torso phantom.

3.1.2 Motion Stage

An MRI compatible motion stage (MR_1A_XRV2, Vital Biomedical Technologies, London, Canada) was used to provide superior-inferior (S/I) motion mimicking a respiratory profile. The motion stage, which has been described in detail by Tavallaei *et al* (2016), is fabricated of non-magnetic materials and comprises a 95-mm long carriage driven along a precisely machined lead screw (50 mm range) by an ultrasonic motor (USR60-NM, Fukoku-Shinsei). The motor is controlled by a custom-designed embedded system,[18] enabling motion to fixed positions as well as continuous dynamic motion, *e.g.* simulating respiration. The stage is capable of reaching fixed positions with an accuracy of 0.1 mm with a normalized RMSE below 3% and has been demonstrated to have a negligible effect on the magnetic field.

3.1.3 Experimental Setup

To enable evaluation of simultaneous PET and MRI, the compartments of the torso phantom and lesion compartments were filled with aqueous solutions that mimic a typically injected dose for total body studies and their resulting background and metabolically active lesion uptakes. Specifically, the torso compartment was filled with 4.27 $kBqmL^{-1}$ of aqueous ^{18}F solution and each lesion compartment was filled with 17 $kBqmL^{-1}$ of ^{18}F solution; the activity levels were selected in accordance with section 7 of the NEMA NU2-2007 protocol describing a method to fill an image quality phantom.[17] To reduce the T1 relaxation time of the aqueous solution, 0.03 gL^{-1} of $MnCl_2 \cdot 4H2O$ was added,[19] along with 4 gL^{-1} of NaCl to reduce dielectric-effect artefacts.

The filled torso phantom was placed at the isocentre of a 3T PET-MRI system (Biograph mMR, Siemens Medical Solutions, Erlangen, Germany). A radiofrequency body coil was used to transmit and two six-element flexible Body Matrix coils and matching elements of the built-in spine-array coil were used as the receiving coil elements. To enable respiratory triggering/gating of the MRI/PET acquisitions, a respiratory bellows was attached to a foam sponge mounted in line with the carriage of the motion stage – compression of the sponge as the carriage moves mimics the *in vivo* situation.

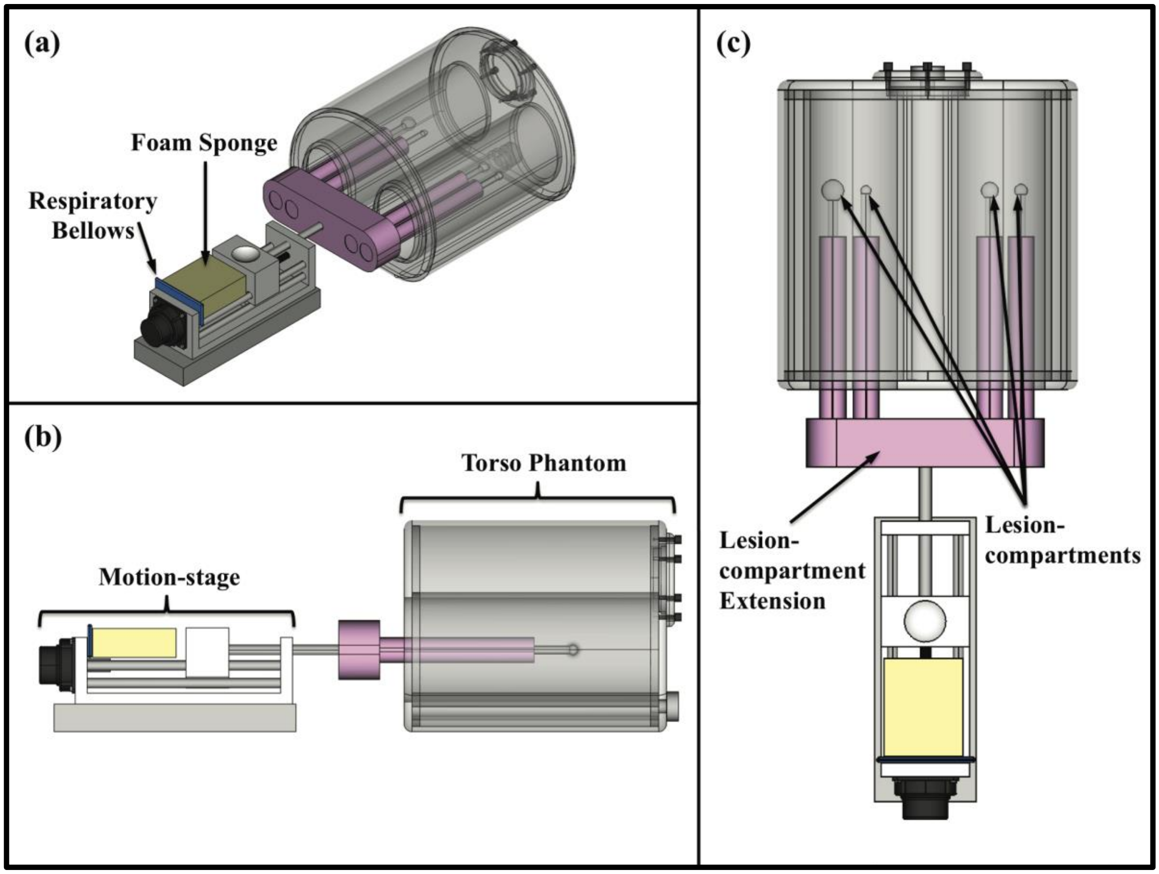

Figure 3-1: Perspective (a), side (b), and top (c) views of the experimental setup. The respiratory bellows and a foam block were attached adjacent the motion stage carriage to provide a trigger for the MRI scans. In the configuration shown four lesion compartments were imaged simultaneously as they underwent S/I motion. All materials are MRI compatible.

3.1.3.1 Motion Profiles

The motion stage was programmed to undergo simulated respiratory motion profiles with a period of 3.4 seconds, representing a breathing rate of ~18 breaths per minute. The profiles were calculated from a modified sine wave, where one third of the period was suspended. (i.e. for a sine of amplitude 1.0 cm, the peak-to-peak excursion was 1.5 cm, with a simulated end exhalation position of -0.5 cm for a duration of 1.13 s). They were defined by:

$$y = \begin{cases} -\frac{A}{2}, & if\ \frac{7T}{12} < t < \frac{11T}{12} \\ A \cdot sin\left(\frac{2\pi t}{T}\right), & otherwise\ , \end{cases} \tag{6}$$

where the position y at time t is a function of the set amplitude A and period T. Two motion profiles – with amplitudes of 1 and 2 cm (peak-to-peak extent of 1.5 and 3 cm, respectively) were evaluated (Figure 3-2). To determine the effect of motion, the lesion compartments were also scanned while static.

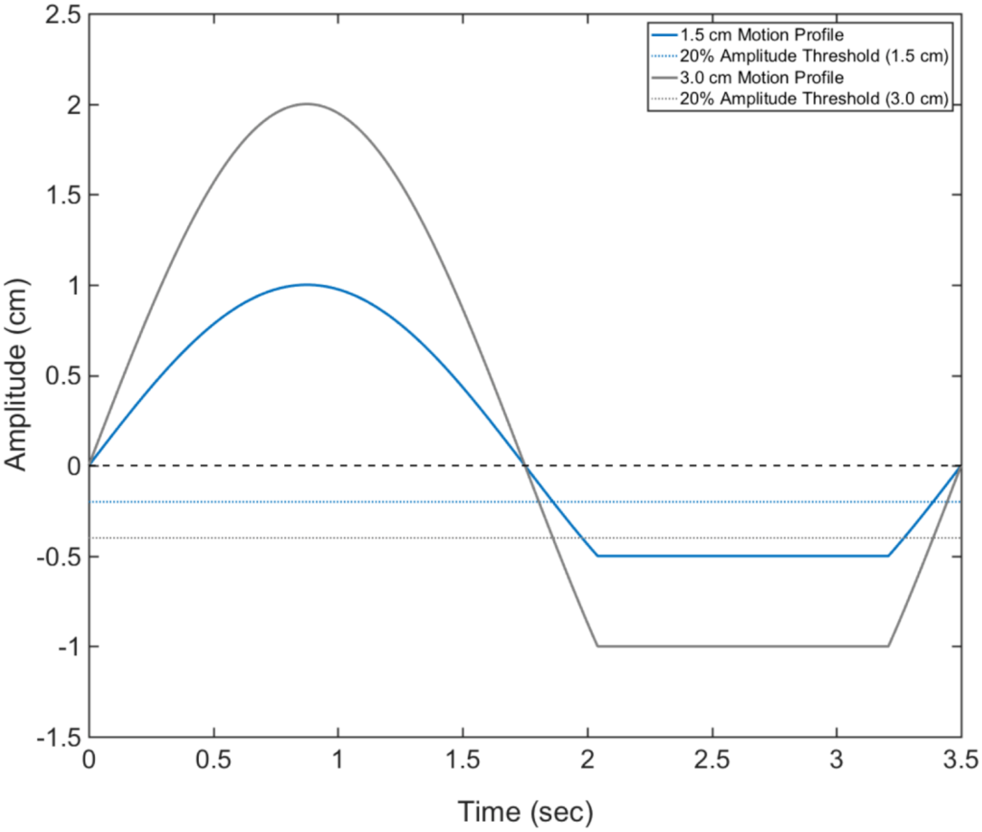

Figure 3-2: Simulated breathing waveforms for 1.5 cm peak-to-peak motion and 3.0 cm peak-to-peak motion.

3.1.4 Imaging

3.1.4.1 MR Imaging

MR images were first acquired for use in attenuation correction of the PET images; maps were acquired with the phantom static and in a simulated breath-hold position to match the motion profile respiratory-trigger positions. Specifically, a 2-compartment-mode Magnetic Resonance Attenuation Correction (MRAC) map designed for phantoms, was used to correct for the water component of the phantom.[20] This map was derived from a T1-weighted two-point Dixon 3D volumetric interpolated breath-hold examination (VIBE) sequence.[21] It was acquired with the following parameters: repetition time (TR) = 4.13 ms, echo times (TE) = 1.23 and 2.46 ms, integrated Parallel Acquisition Technique (iPAT) – GeneRalized Autocalibrating Partially Parallel Acquisitions (GRAPPA) R factor = 2, number of averages (NA) = 1, flip angle (FA) = 10°, matrix size = 192 × 126, slices = 128, voxel size = 2.6 × 2.6 × 3.12 mm^3, and acquisition time (TA) = 0:21 min.

Two pulse sequences, commonly used for RT-diagnosis and planning[22-24] were evaluated. First, the respiratory-triggered T2-weighted turbo spin echo sequence (BLADE) was used to acquire images of the static and moving tumour phantom. Respiratory triggering was provided by the bellows, which was affixed to the motion stage. The TR value was set automatically according to the period of the respiratory cycle (3406 ms) and trigger threshold was set to 20% of tidal volume above the baseline during the exhale position. Image volumes of the torso phantom were acquired in a coronal plane containing all four lesion compartments with the following parameters: TE = 105 ms, GRAPPA with R = 2, NA = 1, FA = 128°, echo train length = 30, matrix = 256 × 256, number of blades = 24, slices = 5, voxel size = 1.3 × 1.3 × 6.0 mm^3, bandwidth (BW) = 781 Hz/pixel, TA = 0:20/0:32 min. Respiratory-triggered images were acquired while the phantom was static and while the lesion compartments were moving with motion extent of 1.5 (RT_1.5) and 3 cm (RT_3.0).

Dynamic images of the moving lesion compartments were also acquired in the coronal orientation using the real-time balanced steady-state free precession sequence (TrueFISP).[25] The scan parameters were: TR/TE = 117.11/1.04 ms, GRAPPA with R =

2, NA = 1, FA = 10°, matrix = 96 × 128, slices = 1, voxel size = 3.1 × 2.5 × 6.0 mm^3, BW = 1002 Hz/pixel. A total of 51 images were captured over an acquisition time of 0:29 min, with a frame rate of ~1.76 frames/s, corresponding to 6 frames in a 3.5 s respiratory cycle. These images were used to evaluate the ability to visualize tumour motion using the commonly employed TrueFISP approach.

3.1.4.2 PET Imaging

List-mode PET data were acquired at a single bed position for 10 minutes. Count rates and total number of counts for the three acquisitions were: static – 19,545 cps/11,727,255; 1.5 cm motion – 15,354 cps/9,212,460; and 3 cm motion – 15,530 cps/9,318,175. While the MRI acquisition times varied for different motion profiles and pulse sequences, a fixed acquisition time was used for the PET scans in order to ensure the observed differences were a reflection of motion characteristics and not scan duration. PET data were binned according to respiration phase, to match the respiratory-triggered MR acquisition, then reconstructed using the ordinary Poisson ordered subsets expectation maximization (3D-OP-OSEM) algorithm[26] (3 iterations, 21 subsets, and 2 mm Gaussian filter). Attenuation correction of PET data acquired without phantom motion was performed with the static MRAC map. Attenuation correction of gated PET data was performed with MRAC maps in a simulated breath-hold position to match the respiratory-trigger positions. The resulting image volumes had: matrix size = 256 × 256, slices = 127, and voxel size = 1.4 × 1.4 × 2.0 mm^3. All acquisitions and phantom motion magnitudes are summarized in Table 3-1.

Table 3-1: Summary of imaging and motion magnitudes evaluated

Phantom Motion (S/I)	MRI Sequence	List-mode PET Duration
Static	MRAC (2-comp.) T2 BLADE-TSE (resp. trig.)	(10 min)
1.5 cm, 3.0 cm	MRAC (2-comp.) T2 BLADE-TSE (resp. trig.) Real time TrueFISP	(10 min)

3.1.5 Data Analysis

3.1.5.1 MR Image Analysis

Displacement of sphere centroids in coronal real-time TrueFISP images were calculated and compared with expected values calculated from equation 1. A binary mask of each real-time image was created by assigning voxels with values less than 25% of the maximum to zero and all others to one. Each centroid coordinate was calculated according to the following:

$$c_a = \sum_{i=1}^{n} w_i c_i / \sum_{i=1}^{n} w_i, \tag{2}$$

where c_a is the calculated x, y, or z-coordinate for the centroid; w_i represents the voxel intensity of the i-th of n voxels in the VOI, and c_i is the x, y, or z-coordinate of the i-th voxel. Actual and expected displacement values were plotted over time and Pearson correlation coefficients were calculated for each motion profile.

Lesion compartment dimensions were measured manually, using digital callipers in 3D Slicer,[27] from each BLADE-TSE image. Measurements were made in the direction of motion and orthogonal to the direction of motion (left/right). These measurements were then compared against the known dimensions of the spheres as a measure of geometric accuracy of the images constructed from the respiratory-triggered BLADE-TSE technique.

3.1.5.2 PET Image Analysis

Lesion compartment volumes in PET images were segmented using the method of Erdi *et al*. In this method, the upper threshold value was set to the maximum voxel value within the volume of interest (VOI) and the lower threshold value was set according to a calculation based on the source-to-background ratio and the expected lesion volume.[28] Mean voxel value and standard deviation, maximum voxel values, and volumetric measurements were calculated with the ‘Label Statistics’ module in 3D Slicer.[27]

Contrast-to-noise ratios (CNR) were calculated using the segmented VOI described above. A spherical VOI, identical in size to each lesion compartment VOI, was placed within the main torso compartment of the phantom to provide a background (BG) measurement. CNR was calculated as follows:

$$CNR = (\bar{s}_{VOI} - \bar{s}_{BG})/\sigma_{BG} \quad , \tag{3}$$

3.1.5.3 PET-MRI Alignment Analysis

Lastly, alignment of sphere compartments between each modality was evaluated. This was achieved through visual inspection of independent and fused coronal images of the PET, respiratory-triggered BLADE-TSE images.

3.2 Results

PET-MRI images were acquired successfully using the developed MRI-compatible respiratory motion phantom. Centroid displacement over time calculated from real-time TrueFISP images shows excellent correlation with the expected displacement values (Figure 3-3). Lesion compartment size shows very little effect on these measurements, with Pearson correlation coefficients being 0.998 and 0.994 for 28 and 10 mm diameter spheres during 1.5 cm of motion and 0.999 and 0.997 for 28 and 10mm diameter spheres during 3.0 cm of motion.

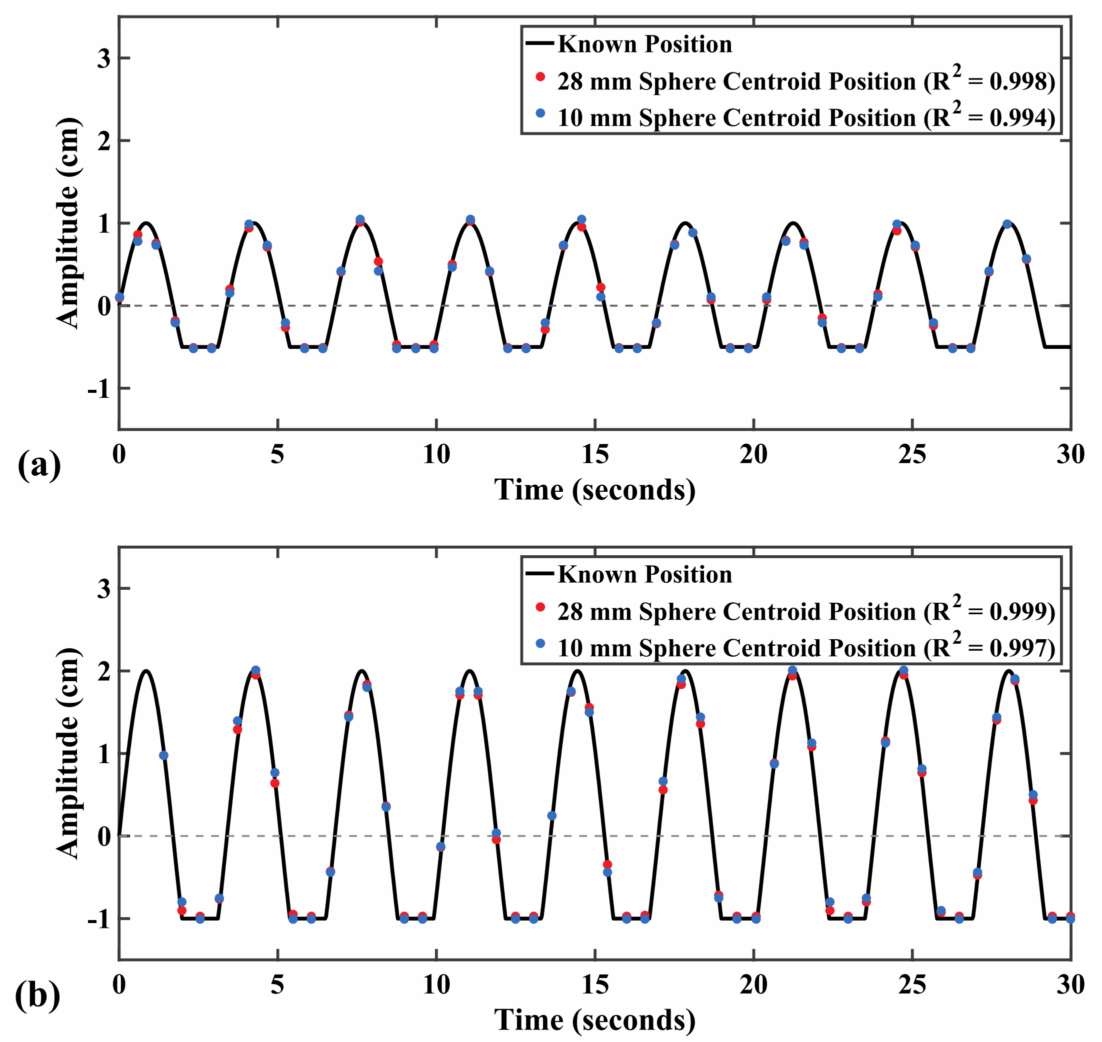

Figure 3-3: Comparison of expected and measured centroid displacements for 28 and 10 mm diameter lesion compartment during a) 1.5 cm peak-to-peak motion; and b) 3.0 cm peak-to-peak motion in real-time TrueFISP MR images.

3.2.1 Motion-induced MRI Errors

Measurements of lesion compartments taken orthogonal to the direction of motion or left/right (L/R) and in the direction of motion (S/I) are presented in Table 3-2.

Table 3-2: Sphere diameter measurements in respiratory-triggered BLADE-TSE images. Measurements were taken in the direction of motion (S/I) and orthogonal to direction of motion (L/R) in static images and in images acquired during 1.5 cm and 3.0 cm of motion.

Sphere Diameter (mm)	Motion Extent (cm)	L/R	S/I
28	Static	28.8	28.8
	1.5	28.8	31.3
	3.0	28.8	33.9
22	Static	22.6	22.6
	1.5	22.5	26.3
	3.0	22.5	27.5
17	Static	17.5	17.5
	1.5	17.5	20.0
	3.0	17.5	21.3
10	Static	10.0	10.1
	1.5	10.0	11.2
	3.0	10.0	12.5

3.2.2 Motion-induced PET Errors

Figure 3-4 compares the mean voxel intensity with standard deviations, maximum voxel intensity, contrast-to-noise ratio, and volumetric measurements of each segmented lesion sphere in PET volumes under both static and triggered conditions. Both of the respiratory-triggered acquisitions should ideally be similar to the reference standard acquisition *(static)*. The RT_1.5 and RT_3.0 acquisitions show lower mean voxel values compared to the static acquisition, with mean values being 6.3%-32.3% and 19.2%-30.4% lower for 1.5 and 3.0 cm of motion respectively. Maximum values are 2.9%-13.77% and 19.8%-34.9% lower for 1.5 and 3.0 cm of motion respectively. Contrast-to-noise values are also lower in both RT_1.5 and RT_3.0 compared to static, with RT_1.5 being lower by 0.1%-3.4% and RT_3.0 by 22.1%-36.2%. An increase in volumetric measurements of lesion-compartments in the respiratory-triggered acquisitions can be seen when compared to the static acquisition. Volumetric increases are between 4.6 and 14.1% for the three largest lesion-compartments and 60.7% for the 10 mm lesion-compartment in the RT_1.5 image. However, in terms of difference from the known volumes, volumes for the three largest lesion-compartments are within 2% for static, 12% for RT_1.5, and 18% for RT_3.0. The 10 mm lesion-compartment measurement is within 11% of the known volume in the static image and 123% for RT_1.5. An appropriate volume could not be measured for the 10 mm lesion-compartment in the RT_3.0 image due to severe smearing of the activity.

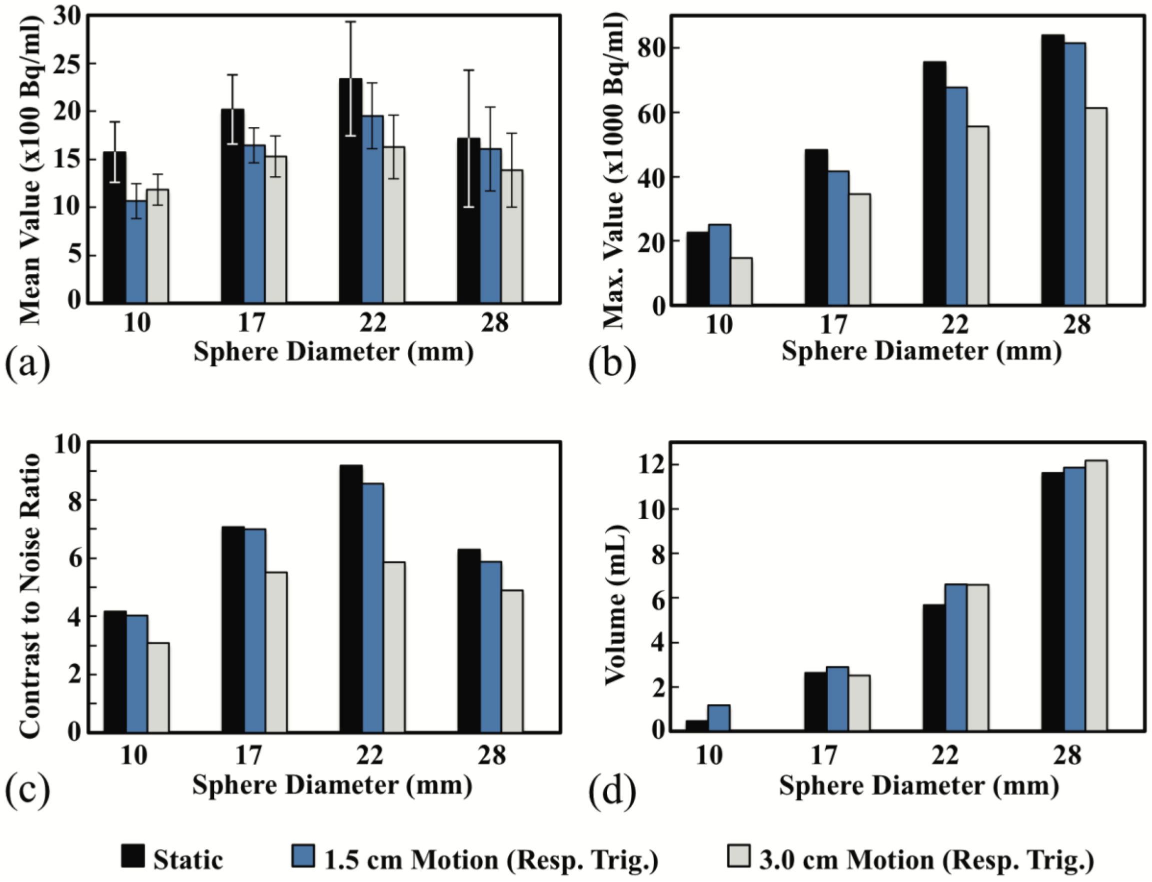

Figure 3-4: (a) Mean voxel intensity of each sphere diameter in PET images during static, 1.5 cm, and 3.0 cm (S/I) motion. Error bars represent the standard deviations over voxels in VOI. (b) Maximum voxel intensity within in each sphere during each of the three cases. (c) Contrast-to-Noise ratios for each of sphere and motion magnitudes. (d) Segmented volumes for each sphere diameter and motion.

3.2.3 PET-MRI Alignment Errors

Coronal images of PET, MRI, and fused volumes for each motion magnitude are shown in Figure 3-5. Upon visual inspection of the PET images for (a) static, (d) RT_1.5, and (g) RT_3.0 motion magnitudes; there is a noticeable amount of additional noise in both gated PET images when compared to the static acquisition, which is particularly noticeable around the edges of the lesion-compartments. This is expected, given the large number of counts outside of the gating windows not included in the reconstructions. The RT_3.0 PET image contains residual motion of the spheres, resulting in the appearance of the spheres in (g) being slightly elongated in comparison to the static image in (a). Respiratory-triggered BLADE-TSE acquisitions performed well at correcting for motion during both the (e) RT_1.5 and (h) RT_3.0 acquisitions, with only slight residual motion in the form of ghosting being noticeable on the inferior side of the sphere in the RT_3.0. All three fused image volumes, (c) static, (f) RT_1.5, and (i) RT_3.0 show good alignment between modalities.

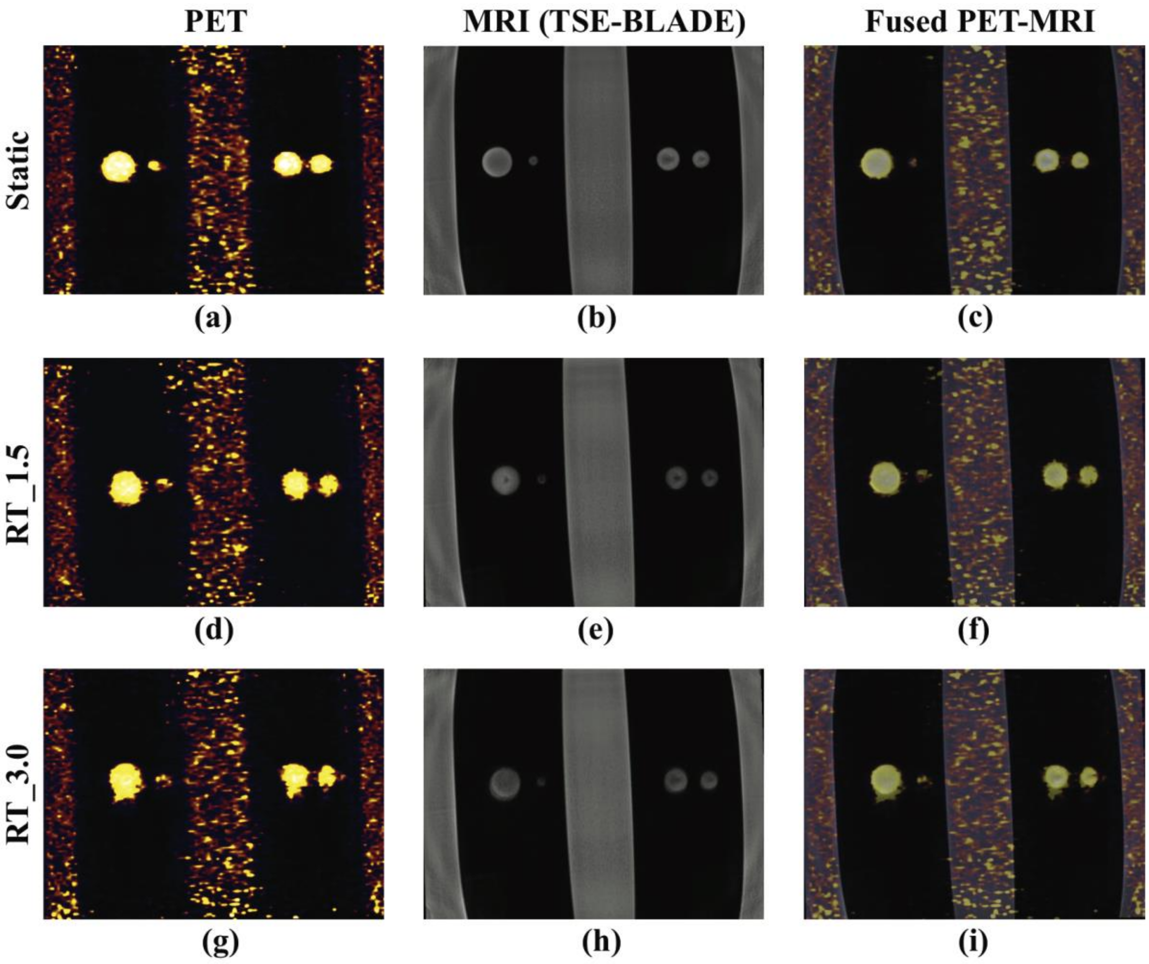

Figure 3-5: Coronal images of (a) PET, (b) MRI, and (c) fused PET-MR of the phantom without motion (static) are shown above. Similarly, coronal images taken from a gated PET with respiratory-triggered BLADE-TSE MRI acquisition during simulated respiratory motion of the lesion compartments with a magnitude of 1.5 cm in the S/I direction are shown in (d) and (e) respectively, and for 3.0 cm of S/I motion are shown in (g) and (h). Fused image of (d) and (e) is shown in (f), and fusion of (g) and (h) can be seen (i).

3.3 Discussion

Centroid measurements of lesion compartments in the real-time TrueFISP images show excellent correlation with the expected motion profile values. The accuracy of the calculated motion profiles suggest dynamic MR protocols like the one used in this study may prove useful in probability distribution function (PDF) based radiotherapy treatment planning. Previous work done with a similar protocol, using a 10 frame/second over 5 minute acquisition time, found that increasing frame rate improves accuracy but has less of an effect on reproducibility of the PDF.[29]

The evaluated respiratory-triggered MRI technique worked well for correcting the motion of our multi-modality respiratory motion torso phantom and showed little geometric distortion of the moving lesion-compartments in terms of deviation from known diameters in both the direction of motion and orthogonally. Given a 20% trigger threshold, the maximum expected motion artefact included in the images is 3 mm for the 1.5 cm motion profile and 6 mm for the 3.0 cm motion profile. Measurement increases in the direction of motion are between 1.2 and 3.8 mm for 1.5 cm of motion and 2.5 to 5.1 mm for 3.0 cm of motion. After accounting for partial volume effect (PVE) from image sampling, these are within the maximum expected motion artefact values. The gated PET technique was also effective at reducing the effects of motion in the phantom, although smearing of PET activity due to motion captured within the gating window resulted in reduced mean and maximum voxel values for segmented lesion-compartment volumes. Also, differences in measured mean and maximum values between the different sized lesion-compartments are likely the result of PVE. It has been shown that PVE is strongly dependant on volume size such that smaller volumes show greater underestimation of activity.[30] Lower calculated CNR values are a result of the lower mean values for all lesion compartments and similarly the different CNR values between different sized lesion-compartments are the result of PVE on mean values. Volumetric measurement increases are likely due to residual smearing of PET activity during gating window as well, however the segmentation technique failed to define an appropriate volume in the RT_3.0 PET image for the 10 mm lesion-compartment due to severe smearing of activity.

The breath-hold MRAC acquisitions resulted in the expected μ-maps and were used for correction of PET images for this study. Although it would be ideal to correct the PET with a gated MRAC, the only currently available MR-based attenuation correction technique does not have motion correction capability. On the other hand, performing MRAC images in the presence of motion causes phase encoding artefacts in the anterior-posterior and in the S/I direction. The process of converting the MR image to an attenuation map incorporated these artefacts into the map, resulting in an overcorrection of attenuation during the PET reconstruction. Although these results were not included, the PET images corrected with MRAC images acquired during phantom motion (as opposed to the ‘simulated breath-hold’ MRACs used in this study) also possessed unwarranted artefacts that resulted in artificially elevated CNR for the larger motion profile acquisitions, and artificially elevated mean SUVs. This suggests that motion correction strategies are required for accurate MRAC acquisition, especially when a patient is unable to hold his or her breath.

Recently, Fürst *et al* evaluated different motion-correction strategies for an integrated PET-MRI system, wherein they acquired the patient respiratory signal through five different methods to retrospectively gate data.[31] From the 14 patient dataset, which included lesions in the breast, liver, and pancreas, with additional lungs, lymph node, esophagus, and small intestine lesions, it was found that respiratory traces acquired through PET data, MR-derived signals, or external sensor (including respiratory bellows), were all comparable. The use of bellows in our experimental setup was effective at extracting the phantom motion profiles and appeared to sufficiently replicate a clinical scenario. Respiratory gating has also been found to provide accurate compensation for imaging liver lesions during free-breathing, in a six patient study using PET-MRI.[32] Evaluating the performance of similar techniques in a repeatable model, such as an imaging phantom, brings additional value in terms of known motion profiles, geometries, and tracer or doping quantities.

Standard protocols and parameters were chosen to evaluate the feasibility of using hybrid PET-MRI for lung radiotherapy applications, as it currently exists. Several techniques have been proposed to correct for motion in PET-MRI that include respiration-phase appropriate MRAC maps and show more promise for applications in radiotherapy planning including motion management,[33-35] but all use the standard breath-hold Dixon sequence attenuation correction. Some patients may find breath-hold protocols challenging and any mismatches between the target respiration-phase in PET and the acquired MRAC will remain uncorrected after the motion correction technique has been applied.

While our phantom does not fully replicate the complexity of anatomy or respiratory motion in patients with lung cancer, it does provide a controlled model that can provide user defined motion profiles with known geometries, contrasts, and activity levels and provides a means for developing routine quality assurance of current clinical PET/MR protocols that account for respiratory motion. The phantom designed for this study could also be extended to other purposes such as future protocol development in hybrid modalities including PET, MRI, and CT. Although the MRAC acquired in this study does not account for the acrylic components of the phantom, all scans were acquired under this same condition. The PET signal lost through the attenuating properties of the phantom materials did not appear to hinder the phantom's ability to demonstrate the desired scanning scenarios, nor their effects on the evaluated protocols.

3.4 Conclusions

Hybrid PET-MRI offers the potential for superb soft-tissue contrast with relevant molecular information for radiotherapy planning in thoracic cases that require motion management. Both the respiratory triggered MRI and gated PET acquisitions evaluated in this study performed well under the prescribed conditions. The simultaneous acquisition of both the triggered MRI and trigger-based gated PET allows for excellent co-registration. However, the current breath-hold protocol used for acquiring and calculating MR-based MRAC maps may still pose a challenge for non-compliant patients. In addition, the phantom developed for this study provided a good model for evaluating the respiratory-triggered PET-MRI protocols (BLADE-TSE and gated PET) and real-time TrueFISP imaging with the given respiratory motion profiles.

3.5 References

1. Nehmeh SA, Erdi YE. Respiratory motion in positron emission tomography/computed tomography: a review. *Semin Nucl Med*. 2008;38(3):167-176.

2. Pépin A, Daouk J, Bailly P, Hapdey S, Meyer M-E. Management of respiratory motion in PET/computed tomography: the state of the art. *Nucl Med Commun*. 2014;35(2):113-122.

3. Catana C. Motion correction options in PET/MRI. *Semin Nucl Med*. 2015;45(3):212-223.

4. Kruis MF, van de Kamer JB, Belderbos JSA, Sonke J-J, van Herk M. 4D CT amplitude binning for the generation of a time-averaged 3D mid-position CT scan. *Phys Med Biol*. 2014;59(18):5517.

5. Chirindel A, Adebahr S, Schuster D, et al. Impact of 4D-(18)FDG-PET/CT imaging on target volume delineation in SBRT patients with central versus peripheral lung tumors. Multi-reader comparative study. *Radiother Oncol*. 2015;115(3):335-341.

6. Deng Z, Pang J, Yang W, et al. Four-dimensional MRI using three-dimensional radial sampling with respiratory self-gating to characterize temporal phase-resolved respiratory motion in the abdomen. *Magn Reson Med*. 2015; 75:1574–1585.

7. Nagamachi S, Wakamatsu H, Kiyohara S, et al. The reproducibility of deep-inspiration breath-hold 18F-FDG PET/CT technique in diagnosing various cancers affected by respiratory motion. *Ann Nucl Med*. 2010;24(3):171-178.

8. Kim HS, Lee KS, Ohno Y, van Beek EJR, Biederer J. PET/CT versus MRI for diagnosis, staging, and follow-up of lung cancer. *J Magn Reson Imaging*. 2015;42(2):247-260.

9. Keall PJ, Mageras GS, Balter JM, et al. The management of respiratory motion in radiation oncology report of AAPM Task Group 76a). *Med Phys*. 2006;33(10).

10. Solberg TD, Agazaryan N, Goss BW, Dahlbom M, Lee SP. A feasibility study of 18F-fluorodeoxyglucose positron emission tomography targeting and simultaneous integrated boost for intensity-modulated radiosurgery and

radiotherapy. *Spec Suppl*. 2004;101:381-389.

11. Hirsch FW, Sattler B, Sorge I, et al. PET/MR in children. Initial clinical experience in paediatric oncology using an integrated PET/MR scanner. *Pediatr Radiol*. 2013;43(7):860-875.

12. Al-Nabhani KZ, Syed R, Michopoulou S, et al. Qualitative and quantitative comparison of PET/CT and PET/MR imaging in clinical practice. *J Nucl Med*. 2014;55(1):88-94.

13. Garibotto V, Heinzer S, Vulliemoz S, et al. Clinical applications of hybrid PET/MRI in neuroimaging. *Clin Nucl Med*. 2013;38(1):e13--e18.

14. Rakheja R, DeMello L, Chandarana H, et al. Comparison of the Accuracy of PET/CT and PET/MRI Spatial Registration of Multiple Metastatic Lesions. *Am J Roentgenol*. 2013;201(5):1120-1123

15. Pipe JG. Motion correction with PROPELLER MRI: application to head motion and free-breathing cardiac imaging. *Magn Reson Med*. 1999;42(5):963-969.

16. Tavallaei MA, Johnson PM, Liu J, Drangova M. Design and evaluation of an MRI-compatible linear motion stage. *Med Phys*. 2016;43(1):62-71.

17. National Electrical Manufacturers Association (NEMA). *NEMA Standards Publication NU 2-2007: Performance Measurements of Positron Emission Tomographs*. Rosslyn, VA: National Electrical Manufacturers Association; 2007.

18. Tavallaei M, Atashzar S, Drangova M. Robust Motion Control of Ultrasonic Motors Under Temperature Disturbance. *Ind Electron IEEE Trans*. 2015;PP(99):2360 – 2368.

19. Schneiders NJ. Solutions of two paramagnetic ions for use in nuclear magnetic resonance phantoms. *Med Phys*. 1988;15(1):12-16.

20. Martinez-Möller A, Souvatzoglou M, Delso G, et al. Tissue Classification as a

Potential Approach for Attenuation Correction in Whole-Body PET/MRI: Evaluation with PET/CT Data. *J Nucl Med*. 2009;50(4):520-526.

21. Dixon WT. Simple proton spectroscopic imaging. *Radiology*. 1984;153(1):189-194.

22. Askoxylakis V, Dinkel J, Eichinger M, et al. Multimodal hypoxia imaging and intensity modulated radiation therapy for unresectable non-small-cell lung cancer: the HIL trial. *Radiat Oncol*. 2012;7(1):1-7.

23. Plathow C, Ley S, Fink C, et al. Analysis of intrathoracic tumor mobility during whole breathing cycle by dynamic MRI. *Int J Radiat Oncol Biol Phys*. 2004;59(4):952-959.

24. Hirokawa Y, Isoda H, Maetani YS, Arizono S, Shimada K, Togashi K. Evaluation of motion correction effect and image quality with the periodically rotated overlapping parallel lines with enhanced reconstruction (PROPELLER) (BLADE) and parallel imaging acquisition technique in the upper abdomen. *J Magn Reson Imaging*. 2008;28(4):957-962.

25. Oppelt A, Graumann R, Barfuss H, Fischer H, Hartl W, Schajor W. FISP—a new fast MRI sequence. *Electromedica*. 1986;54(1):15-18.

26. Comtat C, Bataille F, Michel C, et al. OSEM-3D reconstruction strategies for the ECAT HRRT. In: *Nuclear Science Symposium Conference Record, 2004 IEEE*. Vol 6. ; 2004:3492-3496.

27. Fedorov A, Beichel R, Kalpathy-Cramer J, et al. 3D Slicer as an Image Computing Platform for the Quantitative Imaging Network. *Magn Reson Imaging*. 2012;30(9):1323-1341.

28. Erdi YE, Mawlawi O, Larson SM, et al. Segmentation of lung lesion volume by adaptive positron emission tomography image thresholding. *Cancer*. 1997;80(S12):2505-2509.

29. Sheng JC and PWR and TAA and JAM and JRB and K, Cai J, Read PW, et al. Evaluation of the reproducibility of lung motion probability distribution function (PDF) using dynamic MRI. *Phys Med Biol*. 2007;52(2):365.

30. Hoffman EJ, Huang S-C, Phelps ME. Quantitation in positron emission computed tomography: 1. Effect of object size. *J Comput Assist Tomogr*. 1979;3(3):299-308.

31. Fürst S, Grimm R, Hong I, et al. Motion Correction Strategies for Integrated PET/MR. *J Nucl Med*. 2015;56(2):261-269.

32. Hope TA, Verdin EF, Bergsland EK, Ohliger MA, Corvera CU, Nakakura EK. Correcting for respiratory motion in liver PET/MRI: preliminary evaluation of the utility of bellows and navigated hepatobiliary phase imaging. *EJNMMI Phys*. 2015;2:21.

33. Dutta J, Huang C, Li Q, El Fakhri G. Pulmonary imaging using respiratory motion compensated simultaneous PET/MR. *Med Phys*. 2015;42(7):4227-4240.

34. Würslin C, Schmidt H, Martirosian P, et al. Respiratory Motion Correction in Oncologic PET Using T1-Weighted MR Imaging on a Simultaneous Whole-Body PET/MR System. *J Nucl Med*. 2013;54(3):464-471.

35. Grimm R, Fürst S, Souvatzoglou M, et al. Self-gated MRI motion modeling for respiratory motion compensation in integrated PET/MRI. *Med Image Anal*. 2015;19(1):110-120.

Chapter 4

4 Description and evaluation of an amplitude-based 4D-PET/MRI protocol to characterize tumour respiratory motion

Positron emission tomography (PET) has been established as an effective tool to aid in cancer diagnosis,[1,2] staging,[3-8] and determining treatment response.[9-11] In combination with an anatomical modality like x-ray computed tomography (CT), PET has also proven to be useful for radiotherapy treatment (RT) planning. The combined anatomical and molecular information has not only been used to delineate whole target volumes,[8,12-17] but also used to aid in radiation dose escalation to glucose avid subregions of tumour volumes to help improve treatment outcomes.[18]

However, the application of 3D PET in thoracic RT planning can be problematic, as it often suffers from motion averaging due to respiration. Motion averaging prevents accurate radiotracer activity measurements and obscures the target volume.[19] Dynamic PET techniques, which correlate subsets of 3D PET data to a particular respiration phase or amplitude, offer possible solutions to motion-artefact prone anatomy and have been demonstrated with hybrid PET/CT.[19,20] However, PET/CT data sets are acquired sequentially, with CT scans taking only seconds and PET requiring several minutes to acquire a sufficient number of detected coincidence events. The binning of 3D PET into respiratory-correlated data subsets can greatly reduce motion averaging,[21,22] but each individual data subset alone suffers from diminished photon statistics, decreasing signal-to-noise. Also, PET subsets may not match the respiratory amplitude/phase of the CT acquired in the same imaging session. As patient attenuation correction (AC) of PET is based on a CT image acquired during the same imaging session, the quantitative accuracy of PET may suffer as a result of mismatched respiratory amplitude/phase between modalities.[23] Four-dimensional (4D) CT offers a potential solution to the need for a matching anatomical image and AC for each PET subset. However, the sequential nature of these scans still leaves them susceptible to mismatches due to patient shifting between acquiring each modality and possible differences between modalities in respiratory positions for each data bin.[24]

One major advantage of hybrid PET/MRI is the simultaneous acquisition of both modalities. Previous work on the topic of 4D-PET with MRI have used dynamic sets of MRI and/or PET data for the purpose of motion correction while maintaining or improving on quantitative accuracy of PET.[25-30] But currently, there are no clinical implementations of a dynamic 4D-PET/MRI protocol to characterize tumour respiratory motion for the purposes of radiotherapy treatment planning.

In the following, I describe a 4D-PET/MRI protocol using MR sequences and PET acquisition methods that are currently available clinically on hybrid PET/MRI systems. This technique is validated using a programmable PET/MRI/CT compatible tumour respiratory motion phantom.

4.1 Material and Methods

4.1.1 Motion Phantom Study

A tumour respiratory motion phantom assembly was designed to allow for quality assurance measurements of motion correction protocols in PET, MRI, CT or any combination of these modalities simultaneously. The main torso compartment is made of acrylic plastic and has an elliptical cross-section to simulate the shape and volume of a human torso. There are two cylindrical openings that extend through the length of the torso compartment to simulate lungs. The torso phantom is hollow and can be filled with 11.7 L of MR signal-producing fluid (0.03 gL^{-1} of $MnCl_2{\cdot}4H2O$ and 4 gL^{-1} of NaCl) and PET radiotracer. Additionally, there are four acrylic spheres with different internal diameters of 10, 17, 22, and 28mm that can also be filled with doped water and PET radiotracer. These hollow spheres attach to an MR-compatible linear motion stage (MR_1A_XRV2, Vital Biomedical Technologies, London, Canada) via an extension holder made of polystyrene solid foam. The motion stage can be programmed to move the spheres in any user define motion pattern and the extension holder allows the acrylic spheres to move freely within the lung compartments of the torso phantom (See Figure 4-1). The motion stage is fabricated of non-magnetic materials and has a 95-mm long carriage with a 50 mm range. An ultrasonic motor (USR60-NM, Fukoku-Shinsei) drives the stage's motion and can be user defined. A more detailed description of the motion stage can be found in Tavallaei *et al* (2016).[31]

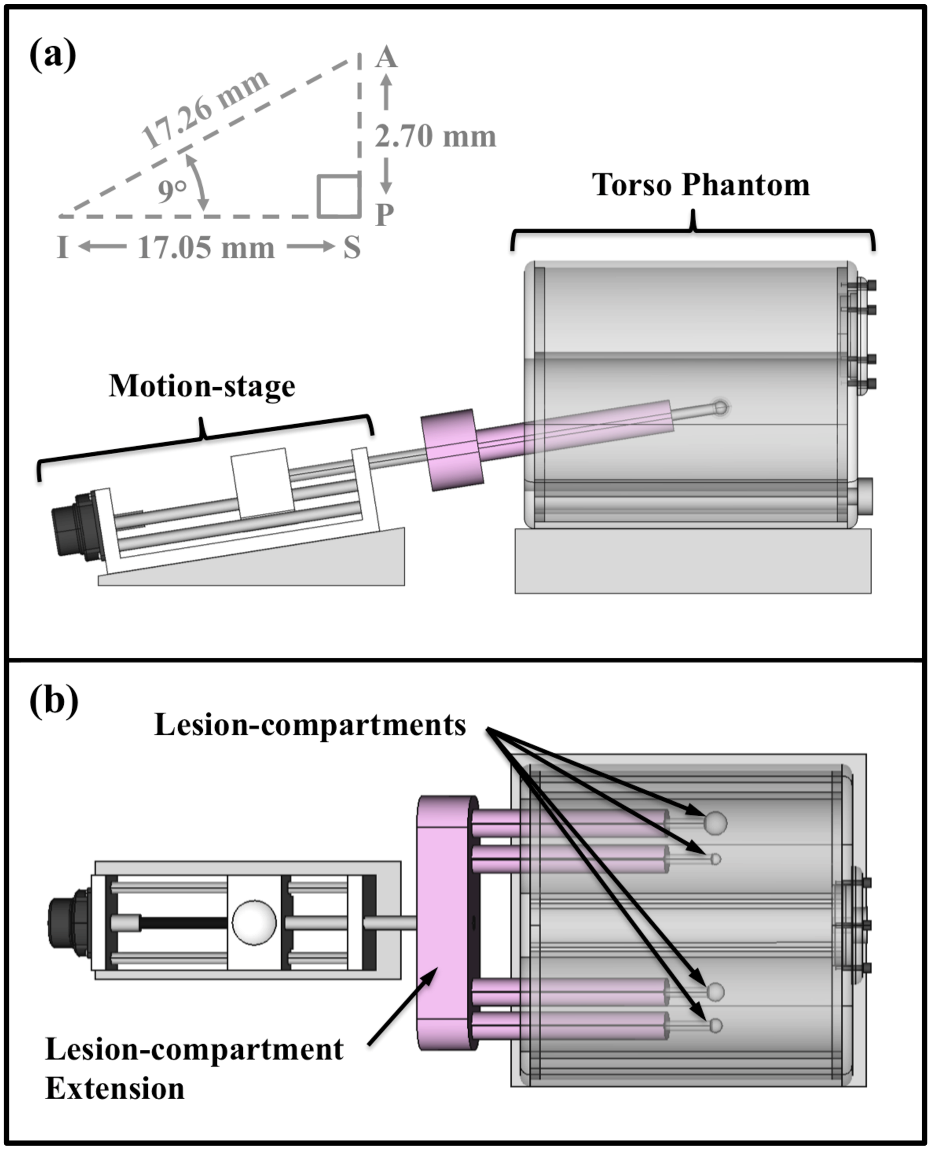

Figure 4-1: Side (a), and top (b) views of the experimental setup. The respiratory bellows and a foam block were attached adjacent the motion stage carriage to provide a trigger for the MRI scans. In the configuration shown four lesion compartments were imaged simultaneously as they underwent S/I motion. All materials are MRI compatible.

In this study, the spheres were each filled with 17 kBq of ^{18}F per mL of MR fluid to simulate glucose-avid lung tumours, while the torso compartment was filled with 4.27 kBq of ^{18}F per mL of MR fluid to simulate normal background uptake in healthy tissues. This provided a target-to-background ratio of 3.98. Three PET/MRI acquisitions of the phantom were acquired, each with a different motion profile. Data files from real patient breathing traces, captured with a Real-Time Position Management suite (Varian Medical Systems, Palo Alto, USA) during CT simulation, were retrospectively used to program two of the motion profiles for the motion stage. Each was scaled to have a maximum distance of 17.26 mm between the minimum and maximum amplitude throughout the breathing trace. The first patient trace (RMP-Pat1) had an average respiratory cycle time of 3.97 seconds and the second trace (RMP-Pat2) had an average respiratory cycle time of 2.34 seconds, and each motion profile demonstrated a different combination of respiration irregularities that may be encountered in the clinic. The third motion profile (RMP-Sim) was a simulated breathing trace consisting of a 30 mm peak-to-peak sinusoidal motion pattern with a dwell at the bottom third of the profile and a period of 3.5 seconds (see Figure 4-2). The motion stage was placed on a 9° incline to produce motion in both the super-inferior (S-I) and anterior-posterior (A-P) directions.

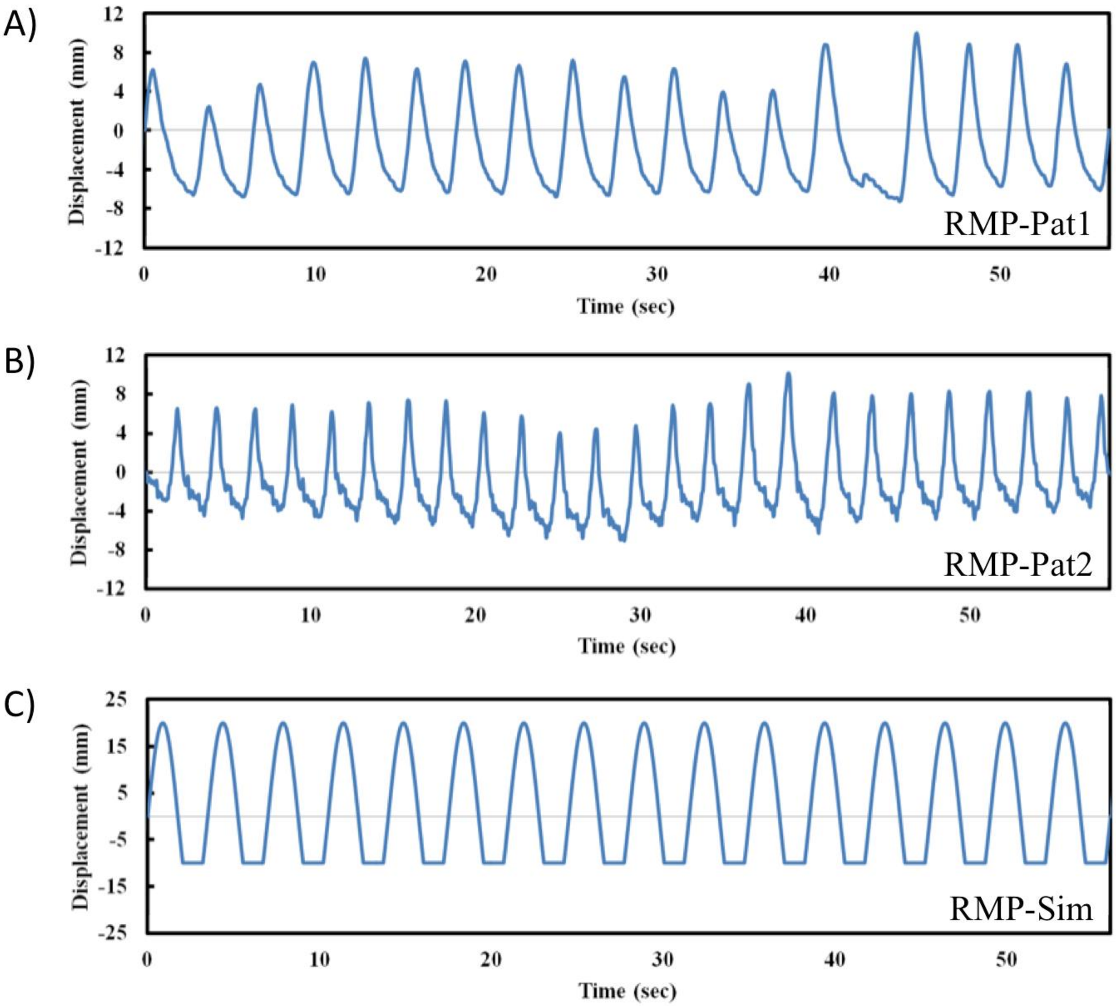

Figure 4-2: Respiratory motion profiles for A) RMP-Pat1, B) RMP-Pat2, and C) RMP-Sim.

Both MRI and PET datasets were acquired and post-processed as described above. Since the motion profile of the phantom is known to be accurate to 0.1 mm with normalized RMSE < 3%,[32] the motion stage data files and derived respiratory phase positions were used as the ground-truth for centroid position comparisons.

4.1.2 Hybrid PET-MR System

A hybrid PET-MRI scanner (Biograph mMR, Siemens Medical, Erlangen, Germany) was used to acquire both 3D and 4D image data. The PET scanner is made up of 8 rings of 56 detector blocks, located in between the radiofrequency and gradient coils. Each block has an 8 × 8 array of lutetium oxyorthosilicate crystals, attached to a 3 × 3 array of avalanche photodiodes APDs), which are water-cooled. The system contains no septa and the transaxial resolution is 4.31 mm and 5.06 mm full-width at half-maximum (FWHM) at 10 mm and 100 mm radius from isocenter, respectively. The axial resolution is 4.28 mm and 6.41 mm FWHM at 10 mm and 100 mm from the isocenter, respectively. System sensitivity was measured as 13.2 kcps/MBq along the center of the scanner field of view and 10.4 kcps/MBq at a 10 cm radial offset. These measurements were taken in accordance with NEMA standard NU 2-2007 and found to be consistent with a previous publication.[33] The manufacturer advertises the system to have a coincidence-timing window of 5.86 ns and time resolution of 2.93 ns. The MR component of this system contains a ~3.0 T superconducting magnet, with an actively shielded whole-body gradient coil with a bore diameter of 60 cm and length of 163 cm. The gradient coils are capable of providing a maximum amplitude of 45 mT/m and a maximum slew rate of 200 (T/m)/s.

4.1.3 4D-PET-MRI Technique

4.1.3.1 MR Imaging

A two-compartment-model attenuation map (μ-map) was first acquired to correct for PET photon attenuation from water content of phantom;[34] maps were acquired with the phantom in a static position to simulate a breath-hold. MR-based μ-maps are derived from a T1-weighted two-point Dixon 3D volumetric interpolated breath-hold examination (VIBE) sequence.[35] The following parameters were used for this acquisition: repetition time (TR) = 3.6 ms, echo times (TE) = 2.46 ms, integrated Parallel Acquisition Technique (iPAT) – GeneRalized Autocalibrating Partially Parallel Acquisitions (GRAPPA) R factor = 2, number of averages (NA) = 1, flip angle (FA) = 10°, matrix size = 192 × 126, slices = 128, voxel size = $2.6 \times 2.6 \times 3.12$ mm^3, and acquisition time (TA) = 0:21 min. Dynamic 2D MR images of the phantom with moving lesion compartments were acquired in 53 adjacent coronal planes using an ultrafast gradient echo pulse sequence (TurboFLASH).[36] The scan parameters were: TR/TE = 242.25/1.12 ms, NA = 1, FA = 10°, matrix = 192 × 192, voxel size = $1.8 \times 1.8 \times 5.0$ mm^3, BW = 1002 Hz/pixel. Within each of the 53 coronal planes, 50 images were captured over an acquisition time of 11:45 minutes, with a frame rate of ~4.19 frames/s. A radiofrequency body coil was used to transmit and two six-element flexible Body Matrix coils and matching elements of the built-in spine-array coil were used as the receiving coil elements.

4.1.3.2 PET Imaging

Dynamic PET data was acquired in list-mode in a single bed position for the duration of the MR acquisitions (~ 12 min). Count rates and total number of counts for the three acquisitions were: RMP-Pat1 – 417,607 cps/ 300,676,912; RMP-Pat2 – 253,675 cps/ 182,646,121; and RMP-Sim – 249,462 cps/ 179,612,612. All PET data sets were reconstructed offline with ordinary Poisson ordered subsets expectation maximization (3D-OP-OSEM) algorithm[37] (3 iterations, 21 subsets, and 2 mm Gaussian filter), using e7 tools software package (version 2.0) (NYU Langone Medical Center and Siemens Healthcare). Decay and scatter correction for all PET image reconstructions were performed in e7 tools. The resulting image volumes had: matrix size = 256 × 256, slices = 127, and voxel size = 2.8 × 2.8 × 2.0 mm^3.

4.1.3.3 Image Data Post-Processing

Respiratory phases were calculated by dividing the distance between the minimum and maximum respiratory amplitudes into 5 amplitude positions. Each amplitude position was then divided into either inspiration or expiration, based on the slope of the tangent at that point in the curve. This made for a total of 10 respiratory phases. Data files from the motion stage were used as surrogate traces for sorting. To achieve our 4D-PET-MRI technique, all 2D MR images acquired within a coronal slice were retrospectively sorted according to amplitude and slope of the point along a surrogate respiratory trace, which corresponded to the image acquisition time, using Matlab code written in house. Phase slice bins containing multiple images were averaged. This was repeated for all slices. For cases where an image slice was missing for a particular phase, images from the phase with the opposite slope but matching amplitude, or next adjacent phase were used. The result was 10 3D-MRI volumes representing the 10 different phases of respiratory motion.

Deformation fields were calculated between each of the 10 3D-MRI volumes using the General Registration (BRAINS) module in 3D Slicer 4.6.2 with the following parameters: B-Spline Grid Size = (15, 15, 5) over the 345.6 × 345.6 × 265 mm^3 image volume, Maximum Step Length = 0.09, Cost Metric = mean square error (MSE).[38] All other parameters were set to defaults. The appropriate subset of deformation fields was applied to the MR-based μ-map, which was acquired at a single *'breath-hold'* position, to create μ-maps for the other 9 phases of respiration.

For each 4D-PET data set, list-mode events were sorted into 10 phases of respiration according to the same surrogate and respiratory phases as the 2D-MRI sorting, also using Matlab code written in house. Gated PET data sets included all counts within 20% of the respiratory trace above baseline generated by the bellows device. As mentioned above, all binned PET data was corrected for attenuation during image reconstruction, using the *'phase-matched'* MR-based μ-maps. The full set of 90 estimated respiratory deformation fields also allowed for warping each PET image volume to every combination of respiratory phase. These deformations were applied and counts were summed at each phase to improve the statistics of each image volume. A summary of this process is illustrated in Figure 4-3.

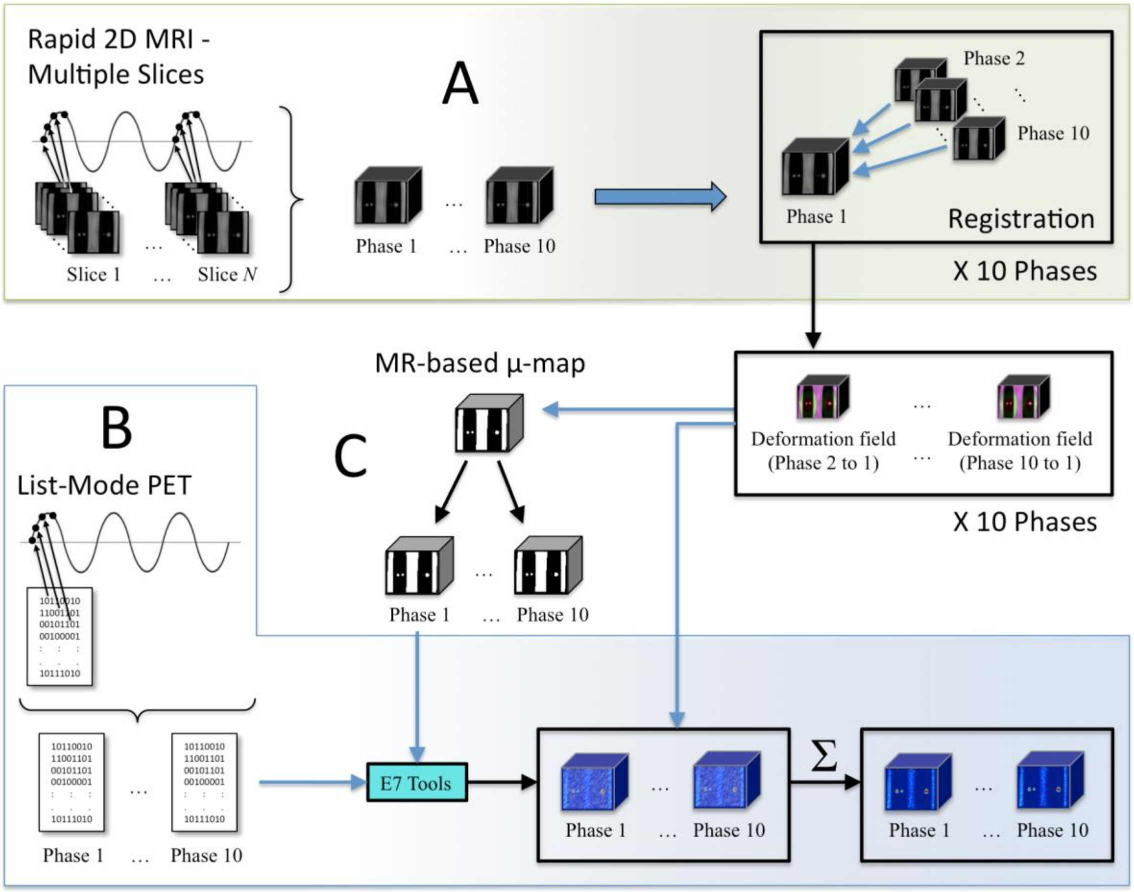

Figure 4-3: The workflow for our proposed 4D-PET-MRI technique. A) Construction of 4D-MRI from dynamic 2D images, B) Calculation of 4D-μ-map, and C) 4D-PET construction.

4.1.4 Data analysis

4.1.4.1 Displacement Accuracy

Displacement of sphere centroids in all 4D volumes (MRI, PET, μ-maps) were calculated and compared with expected values calculated from motion profiles shown in Figure 4-2. A binary mask for each sphere in all 4D volumes was created. For MR volumes, VOI segmentation was performed based on a thresholding algorithm.[39] In PET volumes, spheres were segmented using a method describe by Erdi *et al.*, where the upper threshold value was set to the maximum voxel value within the spherical volume of interest (VOI) and the lower threshold value was set by a calculation based on the source-to-background ratio and the expected lesion volume.[40] Each centroid coordinate was calculated according to the following:

$$c_a = \sum_{i=1}^{n} w_i c_i \Big/ \sum_{i=1}^{n} w_i, \tag{7}$$

where c_a is the calculated x, y, or z-coordinate for the centroid; w_i represents the voxel intensity of the i-th of n voxels in the VOI, and c_i is the x, y, or z-coordinate of the i-th voxel. Actual and expected displacement values for each sphere in all 4D volumes were plotted over % respiratory. This was done for each motion profile.

4.1.4.2 PET Image Analysis

Mean voxel value and standard deviation, maximum voxel values, and volumetric measurements of segmented lesion compartment volumes in PET images were calculated with the 'Label Statistics' module in 3D Slicer.[41] Contrast-to-noise ratios (CNR) were calculated using the segmented VOI described above. Spherical VOIs, identical to the known size of each lesion compartment, was placed within the main torso compartment of the phantom to provide a background (BG) measurement. The following equation was used to calculate CNR:

$$CNR = (\bar{s}_{VOI} - \bar{s}_{BG}) / \sigma_{BG} \quad , \tag{8}$$

where $\bar{s}$ represents the mean intensity of the VOI and σ is the standard deviation of the VOI.

4.2 Results

Representative 4D-PET-MR images of RMP-Pat1 are shown in Figure 4-4. In all three cases, both the 4D-MRI and 4D-PET volumes showed good consistency with the motion phantom and the derived phase images were adequate enough to characterize the motion of the lesion compartments.

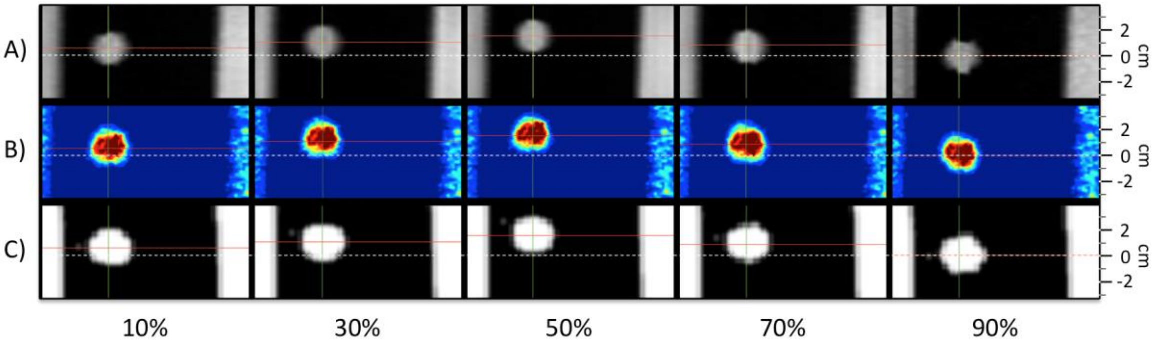

Figure 4-4: Five frames of 4D-PET/MRI: Sagittal view of A) amplitude-sorted 4D-MRI, B) corresponding 4D-PET volumes, and C) MR-based μ-maps of 28 mm diameter sphere.

Figure 4-5 shows the CNR values calculated for the 4D-PET, along with the single gate and ungated acquisitions for each of the four spherical lesion compartments. The general trend showed all CNR values improve as the size of the sphere increased. This was especially the case with the RMP-Sim motion profile, which had a larger peak-to-peak range. Volumetric measurements of segmented spheres in PET images are shown in Figure 4-6. Segmentation method failed for 10 mm sphere in gated and ungated reconstructions of RMP-Sim motion, while there was a high level of variability of 10 mm sphere volume measurements for all other images. Volume measurements for all 4D frames of RMP-Pat1 and RMP-Pat2 showed good agreement with known sphere volumes for 17 mm, 22 mm, and 28 mm. Slight overestimations of volumes for 17 – 28 mm spheres were seen in the all 4D frames of RMP-Sim motion, due to larger range of motion causing residual smearing of activity within each frame, while segmented sphere volumes in gated images slightly underestimated and those in ungated images overestimated sphere volumes. Mean voxel values within segmented sphere volumes are shown in Figure 4-7. Standard deviation also increased with mean voxel values. Mean voxel values in RMP-Sim images were lower than values for RMP-Pat1 and RMP-Pat2, also due to larger range of motion causing residual smearing of activity within each frame.

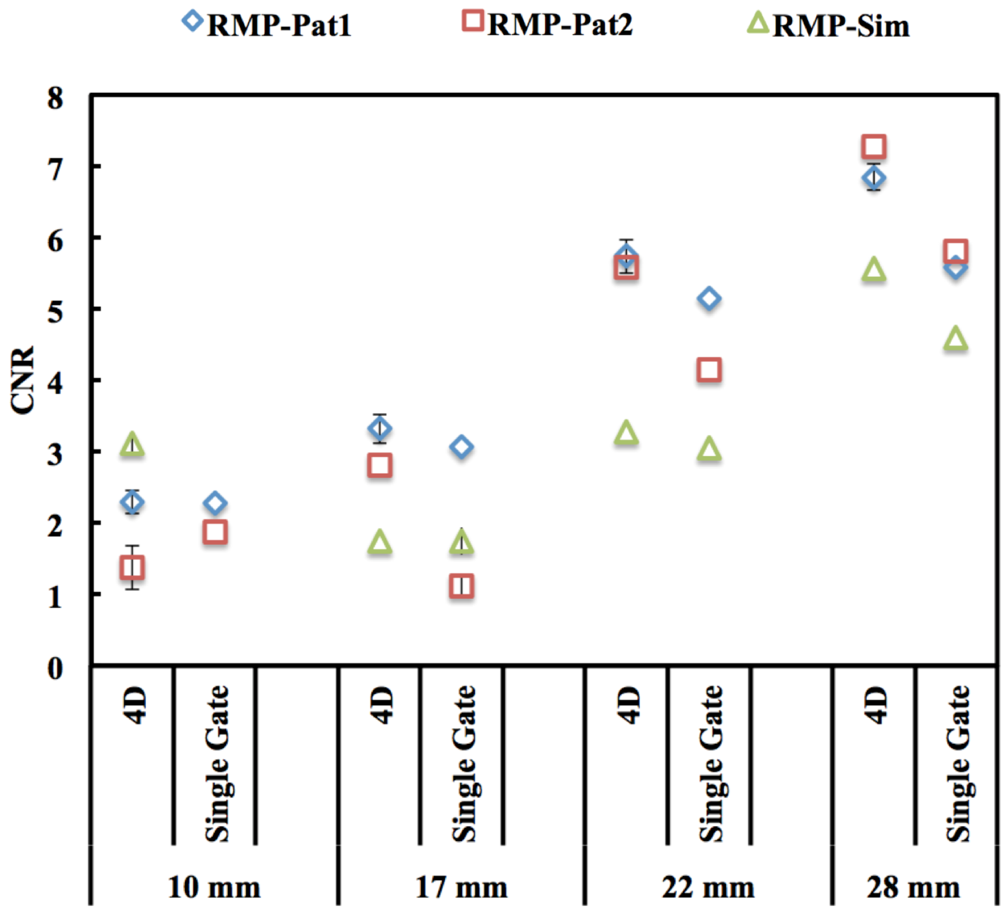

Figure 4-5: Contrast-to-noise-ratios of the 10 mm, 17 mm, 22 mm, and D) 28 mm diameter spheres for 4D-PET, and single gate PET volumes acquired during RMP-Pat1, RMP-Pat2, and RMP-Sim motion profiles.

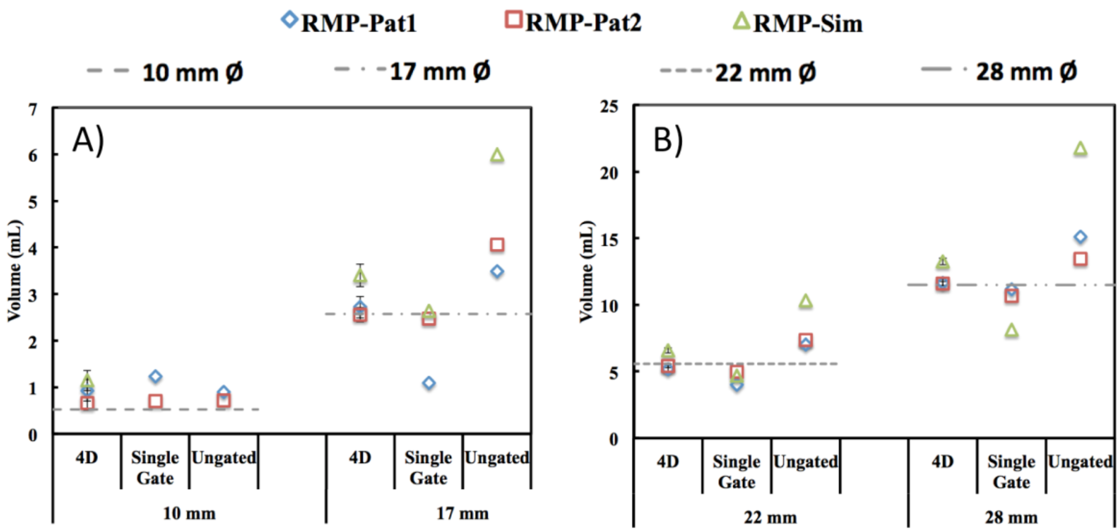

Figure 4-6: Volume measurements of segmented spheres in PET reconstructions for A) 10 and 17 mm, and B) 22 and 28 mm diameter spheres for 4D, gated, and ungated PET acquired during RMP-Pat1, RMP-Pat2, and RMP-Sim motion profiles. Horizontal lines indicate known volumes for each sphere.

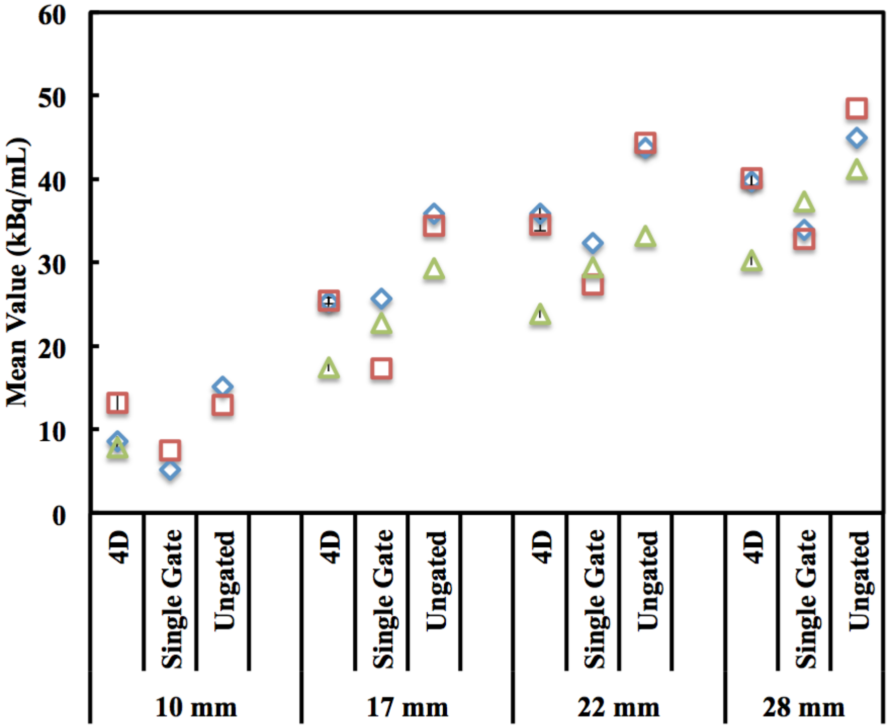

Figure 4-7: Mean voxel intensity of each sphere diameter in PET images RMP-Pat1, RMP-Pat2, and RMP-Sim motion profiles. Error bars represent the standard deviations between phases of 4D-PET.

Figure 4-8 shows superior-inferior (S-I) and anterior-posterior (A-P) centroid displacement measurements through each 4D phase in PET, MRI, and μ-map volumes for the RMP-Pat1 motion profile. The same measurements for RMP-Pat2, and RMP-Sim motion profiles are shown in Figure 4-9 and Figure 4-10 respectively. In the two patient derived motion profiles, RMP-Pat1 has periodic irregularities with an end-inhale standard deviation (SD) = 1.93 mm and end-exhale SD = 0.41 mm over the entire respiratory trace, while RMP-Pat2 contains a baseline shift with end-inhale S.D. = 1.41 mm, end-exhale S.D. = 1.02 mm. Despite these motion irregularities, good agreement with expected centroid positions was achieved. For the regular but larger motion profile, RMP-Sim, excellent agreement with expected values was achieved, except in the case of the 10 mm sphere in the 0% phase PET image. A failure of the segmentation technique, due to extreme smearing of PET activity, prevented centroid measurement.

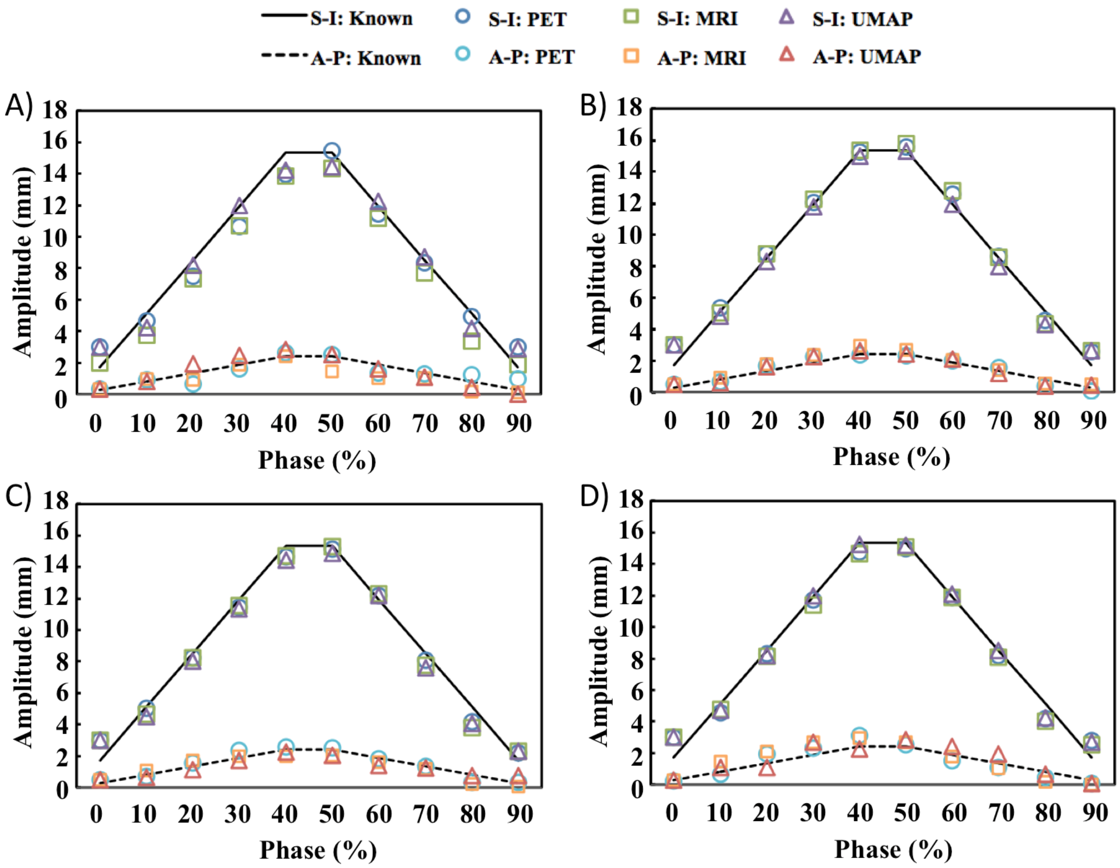

Figure 4-8: RMP-Pat1 centroid measurements in each frame of 4D PET, MRI, and μ-map volumes for the A) 10 mm diameter sphere, B) 17 mm diameter sphere, C) 22 mm diameter sphere, and D) 28 mm diameter sphere.

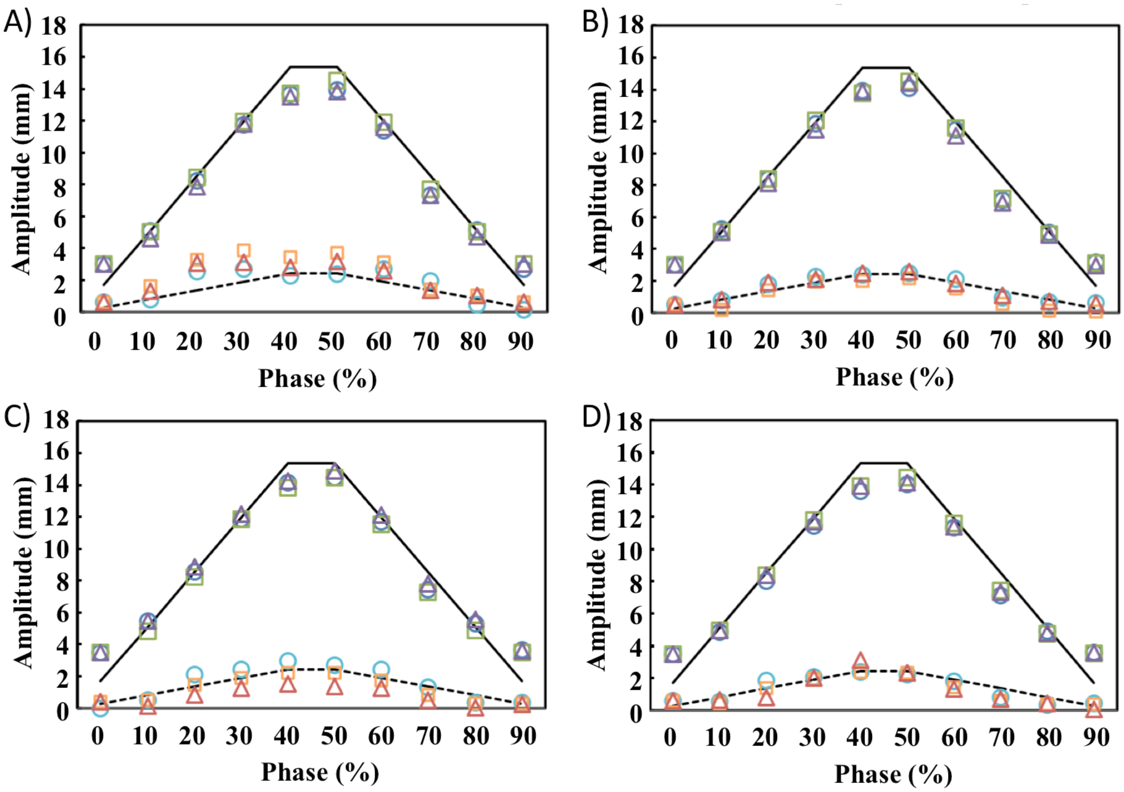

Figure 4-9: RMP-Pat2 centroid measurements in each frame of 4D PET, MRI, and μ-map volumes for A) 10 mm, B) 17 mm, C) 22 mm, and D) 28 mm diameter spheres.

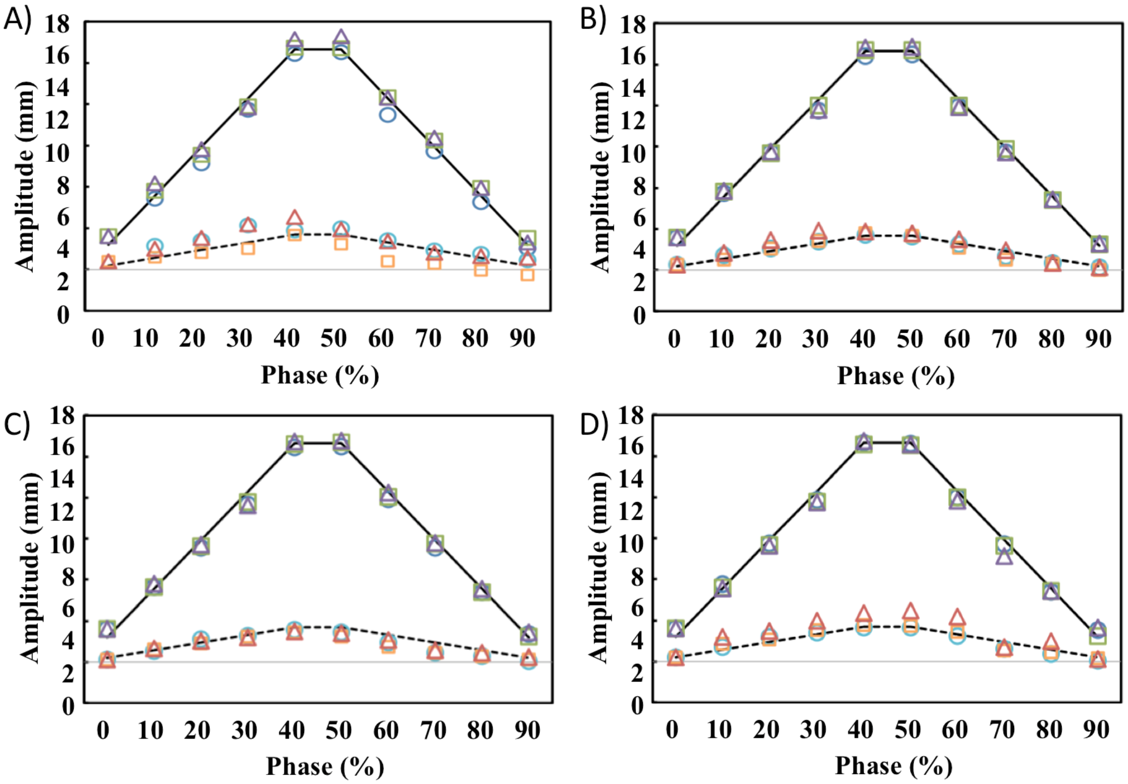

Figure 4-10: RMP-Sim centroid measurements in each frame of 4D PET, MRI, and µ-map volumes for A) 10 mm, B) 17 mm, C) 22 mm, and D) 28 mm diameter spheres.

Table 4-1: Pearson correlation coefficient values between measured centroid displacement positions and their expected position values.

		28 mm Ø		22 mm Ø		17 mm Ø		10 mm Ø	
		A-P	S-I	A-P	S-I	A-P	S-I	A-P	S-I
RMP-Pat1	PET	0.95	0.99	0.96	0.99	0.96	1.00	0.85	0.99
	MRI	0.91	0.99	0.91	0.99	0.98	0.99	0.87	0.99
	μ-map	0.94	0.99	0.96	0.99	0.96	0.99	0.95	0.99
RMP-Pat2	PET	0.91	0.99	0.96	0.99	0.95	0.99	0.87	0.99
	MRI	0.92	0.99	0.95	0.99	0.92	0.99	0.91	0.99
	μ-map	0.90	0.99	0.91	0.99	0.96	0.99	0.90	0.99
RMP-Sim	PET	0.96	1.00	0.94	1.00	0.97	1.00	0.90	1.00
	MRI	0.95	1.00	0.92	1.00	0.96	1.00	0.82	1.00
	μ-map	0.94	0.99	0.96	1.00	0.94	1.00	0.90	1.00

4.3 Discussion

In this study I reported on a retrospective 4D-PET-MRI technique that uses a respiratory surrogate to sort both rapid 2D-MR images over multiple slices and dynamic list-mode PET, using an MR sequence and PET acquisition mode that are available on clinical systems today. The preliminary results from this work suggest that this technique can be used to image anatomy affected by respiratory motion, and potentially used for target delineation in radiotherapy planning of thoracic and/or abdominal lesions. However, further improvements to the image registration technique is desirable to improve the ability to characterize lesions smaller than 17 mm in diameter undergoing motion greater than 1.7 cm. A method described by Brehm *et al* uses a cyclic registration technique for motion compensation and found it to outperform spatial registration using demons deformable registration algorithm for motion estimation to obtain the deformation fields between respiratory phases.[42] This strategy may provide the desired improvements. Additionally, further optimization of MRI parameters to increase temporal resolution, and minimize effects to signal-to-noise ratio and pixel size in-plane could allow more phase volumes to be constructed, improving motion characterization, as well as minimize any need to supplement missing phase-slice images with their close approximations.

Although these preliminary results demonstrate that this technique produces good quality images at multiple phases of respiration, this technique needs to be further validated with patient data. Recent work by Fayad *et al.* describes a technique to generate a 4 phase 4D-PET/MR image dataset. This technique involves the acquisition and sorting of PET data into 4 bins corresponding to the 4 predetermined phases of respiration. Deformation fields between each non-attenuation corrected PET reconstruction are calculated and applied to a single static MR acquisition and MR-based μ-map to generate 4D-MRI and 4D-μ-map volumes.[28] This study shows a high correlation between generated and acquired MR and corresponding μ-maps series, reducing the need for longer 4D MR acquisitions. However, the 4 phases do not differentiate between inspiration/exhalation, and thus may not account for lung hysteresis. Additionally, 4 phases may not be sufficient enough to adequately characterize motion for radiotherapy planning purposes or correct for larger motion profiles.

It is important to note that the current breath-hold Dixon sequence for attenuation correction may prove to be challenging for some patients, and motion during acquisition often results in artefacts, which impact PET accuracy.[43] As such, the development of a free-breathing method may prove beneficial for these cases. A recently introduced free-breathing technique has been proposed for cardiac PET-MRI[44] and may prove useful in other thoracic and abdominal imaging, however this approach is not yet widely available.

In our PET analysis, extreme smearing of PET activity in the 10 mm diameter sphere caused the segmentation technique to fail in the gated and ungated images of the RMP-Sim motion. Although segmentation of the 10 mm sphere was achieved in the 4D technique, the instability of CNR and volume values suggest the registration step of our method was not able to calculate appropriate deformation fields for this sphere. This is due to its small size in relation to the magnitude of motion. The CNR values for the 17 mm sphere in all frames of the 4D PET images were very low, due to inadequate deformation fields being calculated between phases. This is all despite improvements in mean voxel intensity values seen in segmented VOIs for our 4D technique over the single gated PET reconstructions (Figure 4-7). demonstrates a limitation of the registration method during larger extents of motion. All other PET measurements suggest our 4D-PET-MRI technique performed well.

Centroid measurements of spheres in PET, MR, and μ-maps show excellent correlation with the expected motion profile values at each phase (see Figure 4-8 to Figure 4-10). However, in all instances the larger deviations from expected centroid positions were found in the 10 mm sphere measurements, suggesting a limitation of this technique's ability to characterize motion of smaller tumours (<17 mm diameter). A motion compensated PET/MR technique that uses a novel radial navigated MR pulse sequence to construct up to 12 gates is used to calculate deformation fields between gates.[26] The deformation fields are then applied to both PET and μ-map volumes to create a single motion corrected volume. The simulation study shows the resulting PET image to have a 10-15% improvement in CNR for 10 mm pulmonary lesions in relation to a single gate acquisition. Although the lack of clinical availability of this pulse sequence is a limitation of this technique, it may provide the necessary improvements in temporal resolution and contrast to correct for motion of smaller lesions in 4D-PET-MRI.

4.4 Conclusions

Our study demonstrates the feasibility of a novel retrospective 4D-PET-MRI technique with attenuation correction in a dynamic PET/MR/CT compatible tumour respiratory motion phantom. Our technique has the advantage of using a clinically available pulse sequence, eliminating the need for less available more exotic sequences or MR pulse sequence programming.

4.5 References

1. Wu Y, Li P, Zhang H, et al. Diagnostic value of fluorine 18 fluorodeoxyglucose positron emission tomography/computed tomography for the detection of metastases in non--small-cell lung cancer patients. *Int J Cancer*. 2013;132(2):E37--E47.

2. Veronesi G, Travaini LL, Maisonneuve P, et al. Positron emission tomography in the diagnostic work-up of screening-detected lung nodules. *Eur Respir J*. 2015;45(2):501-510.

3. Antoch G, Stattaus J, Nemat AT, et al. Non–Small Cell Lung Cancer: Dual-Modality PET/CT in Preoperative Staging. *Radiology*. 2003;229(2):526-533.

4. Dwamena BA, Sonnad SS, Angobaldo JO, Wahl RL. Metastases from Non-Small Cell Lung Cancer: Mediastinal Staging in the 1990s—Meta-analytic Comparison Of PET and CT. *Radiology*. 1999;213(2):530-536.

5. Gould M, MD MS, Kuschner W, et al. Test Performance of Positron Emission Tomography and Computed Tomography for Mediastinal Staging in Patients with Non-Small-Cell Lung Cancer: A Meta-Analysis. *Ann Intern Med*. 2003;139(11):879-892.

6. Lardinois D, Weder W, Hany TF, et al. Staging of Non–Small-Cell Lung Cancer with Integrated Positron-Emission Tomography and Computed Tomography. *N Engl J Med*. 2003;348(25):2500-2507.

7. Pieterman RM, van Putten JWG, Meuzelaar JJ, et al. Preoperative Staging of Non–Small-Cell Lung Cancer with Positron-Emission Tomography. *N Engl J Med*. 2000;343(4):254-261.

8. Vanuytsel LJ, Vansteenkiste JF, Stroobants SG, et al. The impact of 18F-fluoro-2-deoxy-d-glucose positron emission tomography (FDG-PET) lymph node staging on the radiation treatment volumes in patients with non-small cell lung cancer. *Radiother Oncol*. 2000;55(3):317-324.

9. Bollineni VR, Widder J, Pruim J, Langendijk JA, Wiegman EM. Residual 18F-FDG-PET Uptake 12 Weeks After Stereotactic Ablative Radiotherapy for Stage I Non-Small-Cell Lung Cancer Predicts Local Control. *Int J Radiat Oncol • Biol • Phys*. 2012;83(4):e551-e555.

10. Gayed I, Vu T, Iyer R, et al. The Role of 18F-FDG PET in Staging and Early Prediction of Response to Therapy of Recurrent Gastrointestinal Stromal Tumors. *J Nucl Med*. 2004;45(1):17-21.

11. Weber WA, Petersen V, Schmidt B, et al. Positron Emission Tomography in Non–Small-Cell Lung Cancer: Prediction of Response to Chemotherapy by Quantitative Assessment of Glucose Use. *J Clin Oncol*. 2003;21(14):2651-2657.

12. Biehl KJ, Kong F-M, Dehdashti F, et al. 18F-FDG PET Definition of Gross Tumor Volume for Radiotherapy of Non–Small Cell Lung Cancer: Is a Single Standardized Uptake Value Threshold Approach Appropriate? *J Nucl Med*. 2006;47(11):1808-1812.

13. Bradley J, Thorstad WL, Mutic S, et al. Impact of FDG-PET on radiation therapy volume delineation in non–small-cell lung cancer. *Int J Radiat Oncol*. 2004;59(1):78-86.

14. Caldwell CB, Mah K, Ung YC, et al. Observer variation in contouring gross tumor volume in patients with poorly defined non-small-cell lung tumors on CT: the impact of 18FDG-hybrid PET fusion. *Int J Radiat Oncol • Biol • Phys*. 2001;51(4):923-931.

15. Erdi YE, Rosenzweig K, Erdi AK, et al. Radiotherapy treatment planning for patients with non-small cell lung cancer using positron emission tomography (PET). *Radiother Oncol*. 2002;62(1):51-60.

16. Mah K, Caldwell CB, Ung YC, et al. The impact of 18 FDG-PET on target and critical organs in CT-based treatment planning of patients with poorly defined non-small-cell lung carcinoma: a prospective study. *Int J Radiat Oncol • Biol •*

Phys. 2002;52(2):339-350.

17. Paulino AC, Thorstad WL, Fox T. Role of fusion in radiotherapy treatment planning. *Semin Nucl Med*. 2003;33(3):238-243.

18. Solberg TD, Agazaryan N, Goss BW, Dahlbom M, Lee SP. A feasibility study of 18F-fluorodeoxyglucose positron emission tomography targeting and simultaneous integrated boost for intensity-modulated radiosurgery and radiotherapy. *Spec Suppl*. 2004;101:381-389.

19. Callahan J, Kron T, Siva S, et al. Geographic miss of lung tumours due to respiratory motion: a comparison of 3D vs 4D PET/CT defined target volumes. *Radiat Oncol*. 2014;9(1):291.

20. Aristophanous M, Berbeco RI, Killoran JH, et al. Clinical Utility of 4D FDG-PET/CT Scans in Radiation Treatment Planning. *Int J Radiat Oncol*. 2012;82(1):e99-e105.

21. Nehmeh SA, Erdi YE, Pan T, et al. Four-dimensional (4D) PET/CT imaging of the thorax. *Med Phys*. 2004;31(12):3179-3186.

22. Wolthaus JWH, Van Herk M, Muller SH, et al. Fusion of respiration-correlated PET and CT scans: correlated lung tumour motion in anatomical and functional scans. *Phys Med Biol*. 2005;50(7):1569.

23. Erdi YE, Nehmeh SA, Pan T, et al. The CT motion quantitation of lung lesions and its impact on PET-measured SUVs. *J Nucl Med*. 2004;45(8):1287-1292.

24. Nehmeh SA, Erdi YE, Pan T, et al. Quantitation of respiratory motion during 4D-PET/CT acquisition. *Med Phys*. 2004;31(6):1333-1338.

25. Würslin C, Schmidt H, Martirosian P, et al. Respiratory Motion Correction in Oncologic PET Using T1-Weighted MR Imaging on a Simultaneous Whole-Body PET/MR System. *J Nucl Med*. 2013;54(3):464-471.

26. Dutta J, Huang C, Li Q, El Fakhri G. Pulmonary imaging using respiratory motion compensated simultaneous PET/MR. *Med Phys*. 2015;42(7):4227-4240.

27. Fayad H, Schmidt H, Wuerslin C, Visvikis D. Reconstruction-Incorporated Respiratory Motion Correction in Clinical Simultaneous PET/MR Imaging for Oncology Applications. *J Nucl Med*. 2015;56(6):884-889.

28. Fayad H, Schmidt H, Kuestner T, Visvikis D. 4D MR and attenuation map generation in PET/MR imaging using 4D PET derived deformation matrices: a feasibility study for lung cancer applications. *J Nucl Med*. October 2016.

29. Tsui TF and JW and GF and B. Non-rigid dual respiratory and cardiac motion correction methods after, during, and before image reconstruction for 4D cardiac PET. *Phys Med Biol*. 2016;61(1):151.

30. Rank CM, Heußer T, Wetscherek A, et al. Respiratory motion compensation for simultaneous PET/MR based on highly undersampled MR data. *Med Phys*. 2016;43(12):6234-6245.

31. Tavallaei MA, Johnson PM, Liu J, Drangova M. Design and evaluation of an MRI-compatible linear motion stage. *Med Phys*. 2016;43(1):62-71.

32. Tavallaei M, Atashzar S, Drangova M. Robust Motion Control of Ultrasonic Motors Under Temperature Disturbance. *Ind Electron IEEE Trans*. 2015;PP(99):2360 – 2368.

33. Delso G, F\urst S, Jakoby B, et al. Performance measurements of the Siemens mMR integrated whole-body PET/MR scanner. *J Nucl Med*. 2011;52(12):1914-1922.

34. Martinez-Möller A, Souvatzoglou M, Delso G, et al. Tissue Classification as a Potential Approach for Attenuation Correction in Whole-Body PET/MRI: Evaluation with PET/CT Data. *J Nucl Med*. 2009;50(4):520-526.

35. Dixon WT. Simple proton spectroscopic imaging. *Radiology*. 1984;153(1):189-

194.

36. Haase A, Frahm J, Matthaei D, Hanicke W, Merboldt K-D. FLASH imaging. Rapid NMR imaging using low flip-angle pulses. *J Magn Reson*. 1986;67(2):258-266.

37. Comtat C, Bataille F, Michel C, et al. OSEM-3D reconstruction strategies for the ECAT HRRT. In: *Nuclear Science Symposium Conference Record, 2004 IEEE*. Vol 6. ; 2004:3492-3496.

38. Johnson HJ, Harris G, Williams K. BRAINSFit: Mutual Information Registrations of Whole-Brain 3D Images, Using the Insight Toolkit. *Insight J*. 2007.

39. Otsu N. A threshold selection method from gray-level histograms. *Automatica*. 1975;11(285-296):23-27.

40. Erdi YE, Mawlawi O, Larson SM, et al. Segmentation of lung lesion volume by adaptive positron emission tomography image thresholding. *Cancer*. 1997;80(S12):2505-2509.

41. Fedorov A, Beichel R, Kalpathy-Cramer J, et al. 3D Slicer as an Image Computing Platform for the Quantitative Imaging Network. *Magn Reson Imaging*. 2012;30(9):1323-1341.

42. Brehm M, Paysan P, Oelhafen M, Kunz P, Kachelrieß M. Self-adapting cyclic registration for motion-compensated cone-beam CT in image-guided radiation therapy. *Med Phys*. 2012;39(12):7603-7618.

43. Keller SH, Holm S, Hansen AE, et al. Image artifacts from MR-based attenuation correction in clinical, whole-body PET/MRI. *Magn Reson Mater Physics, Biol Med*. 2013;26(1):173-181.

44. Robson PM, Dweck MR, Trivieri MG, et al. Coronary Artery PET/MR Imaging: Feasibility, Limitations, and Solutions. *JACC Cardiovasc Imaging*. 2017.

Chapter 5

5 Conclusions and Future Work

An important goal in radiotherapy planning is to optimize delivered dose to tumours while sparing surrounding healthy tissues. The ability to achieve this goal relies heavily on the detail and accuracy of information that can discriminate between cancerous and healthy tissues and provide spatial information about the treatment target and surrounding tissues. Hybrid PET-MRI is the marriage of two gold standards in medical imaging. MRI is capable of imaging soft-tissues with superb detail and contrast, and can provide information related to perfusion and permeability. PET on the other hand, in combination with an ever-expanding selection of radiotracers, brings complimentary information about the distribution of molecular characteristics of tissues. This thesis describes the development of techniques to improve the utility of hybrid PET-MRI for radiotherapy planning applications. In this chapter, I summarize the work and findings of the previous three chapters, and present the overall conclusions from the thesis. I will then reiterate the research questions and hypotheses that were initially proposed in the introduction (see Section 1.6). This is followed by a discussion of our proposed answers to those research questions. Finally, I will motivate potential future research directions related to this work and our findings. More specifically, future work that will: 1) demonstrate the improvements in PET quantitation with MVCT-based attenuation correction of various MRI hardware components in a clinical setting; and 2) further investigate the benefits of using 4D PET-MRI for clinical radiotherapy planning of tumours in sites impacted by respiratory motion.

5.1 Techniques to Improve Accuracy of MRI Hardware Attenuation Maps in PET-MRI

In the second chapter of this thesis, I implemented two different techniques to improve upon current methods of μ-map construction for MRI hardware containing dense materials used in PET-MRI. The first technique used a DECT scan (80 kVp and 140 kVp) of the MRI hardware (four-channel breast receive-only coil) to construct virtual monoenergetic image volumes, effectively reducing the amount of beam hardening caused by dense materials such as metal. The second technique used a tomotherapy linear accelerator to create CT images at megavoltage energies (1.0 MV) of the four-channel breast coil. In the megavoltage range, Compton scatter is the dominant photon interaction and better photon penetration through dense materials can be achieved. Two scans of homogenous cylindrical phantoms were acquired. The first scan was acquired in the presence of the breast coil, while the second acquisition was taken with the phantoms in a polystyrene rigid foam fixture, positioned identical to the breast coil. Both μ-map construction techniques were compared to a previously published technique that calculated a hardware μ-map from a standard SECT at kilovoltage energies. The DECT-based technique reduced the amount of visible metal artefact streaking in the image volumes and this translated to improved accuracy of the μ-map. This improvement was demonstrated in the DECT-based μ-map corrected PET volume, which showed improved homogeneity throughout the phantoms. Although this technique improved on the SECT-based method by reducing the effects of beam hardening, the virtual monoenergetic images from which the μ-maps are calculated were still subject to other sources of error (i.e. signal truncation, and noise from scattered radiation). However, the MVCT-based technique improved further on the artefact reduction seen in the virtual monoenergetic image reconstructions from DECT. The lack of visible artefacts in the MVCT images resulted in an artefact free μ-map, which facilitated a more accurate correction of PET photon attenuation from the breast coil.

5.2 Development of a PET/MRI/CT-Compatible Tumour Respiratory Motion Phantom for Quality Assurance

In Chapter 3, I designed a PET-MR-CT compatible respiratory motion phantom for quality assurance of motion-correction protocols in hybrid imaging modalities. The all-acrylic phantom had five compartments and was created to represent an average human torso with air cavities representing the lungs. The main torso compartment contained three smaller cylinders running the full length of the torso – two compartments to represent the lungs and a single smaller compartment to represent a spine. The two lung compartments are open at the inferior end of the torso to allow lesion-mimicking compartments to move freely inside while attached to the MRI compatible motion stage.[1]

In this study, lesions were simulated with four acrylic spheres (28 mm, 22 mm, 17 mm, and 10 mm internal diameters). I then used this phantom to evaluate the accuracy and sensitivity of a clinically available real-time dynamic MR images and a respiratory-triggered PET-MRI protocol in detecting the lesions while moving at two different magnitudes of motion (peak-to-peak extent of 1.5 and 3 cm). Displacement measurements of lesion centroids in dynamic MR images using the real-time balanced steady-state free precession sequence (TrueFISP),[2] showed excellent correlation with known displacement values ($r^2 = 0.994$ to 0.998 and $r^2 = 0.997$ to 0.999 for 1.5 cm and 3.0 cm displacement respectively). The respiratory-triggered T2-weighted single-shot turbo spin echo sequence (BLADE)[3] saw sphere diameter measurement increases in the direction of motion are between 1.2 and 3.8 mm for 1.5 cm of motion and 2.5 to 5.1 mm for 3.0 cm of motion. These are within the maximum expected motion artefact values, once image sampling is taking into account. PET images from data binned according to the respiratory-triggered MR acquisition resulted in a reduction in mean and maximum voxel intensities for both motion magnitudes when compared to static PET. Gated PET show a slight increase in lesion compartment volumes, due to residual smearing of PET activity during the gating window. Overall, the results show that both the respiratory-triggered MRI and gated PET perform well under the motion conditions presented and allow for excellent co-registration of the modalities. It was noted however, that the current breath-hold protocol used for acquiring and calculating MR-based MRAC maps may still pose a challenge for non-compliant patients. Additionally, it was found that the phantom developed for this study provides a good model for performing routine quality assurance of respiratory-triggered PET-MRI and as such was able to provide useful tool for the development of the technique presented in Chapter 4.

5.3 Development of a 4D PET-MRI Protocol to Characterize Respiratory Motion

Chapter 4 presents the description and results from evaluating a 4D-PET/MRI post-processing technique, using MR sequences and PET acquisition methods that are already available on clinical hybrid PET/MRI systems. This technique is validated using the programmable PET/MRI/CT compatible tumour respiratory motion phantom that was developed and presented in Chapter 3 as a tool to evaluate a diagnostic PET/MRI lung protocol with motion correction. It was suggested in the discussion of Chapter 3 that, in addition to quality assurance measurements of existing protocols, my phantom could be used for protocol development. The work in Chapter 4 demonstrates the use of this phantom for the development of a 4D-PET/MRI technique.

First, an MR-based μ-map was acquired with a T1-weighted two-point Dixon 3D volumetric interpolated breath-hold examination (VIBE) sequence,[4] at the beginning of each acquisition. This was followed by a dynamic 2D MR images of the phantom with moving lesion compartments were acquired in 53 adjacent coronal slices (50 per slice) using an ultrafast gradient echo pulse sequence (TurboFLASH).[5] Dynamic PET data was also acquired in list-mode at a single bed position for the duration of the MR acquisitions (~ 12 min). Using the data files from the motion stage as surrogate trace for sorting, 10 respiratory phases were calculated by dividing the distance between the minimum and maximum respiratory amplitudes into 5 amplitude positions and then dividing those according to inspiration or expiration. All 2D MR images and list-mode PET data were sorted into their respective bins according to this surrogate, resulting in 10 3D-MRI volumes and 10 list-mode PET files, one for each respiratory phase. Each list-mode PET file was reconstructed into 10 PET image volumes. Deformation fields were calculate between all phases using the newly constructed MRI volumes and then applied to the single-phase μ-map to produce a μ-map for each of the ten phases. The deformation fields were also applied to each PET volume. This allows all counts collected throughout the scan to be summed at each of the 10 phases, to improve image statistics. As mentioned previously, our validation study used our torso phantom with four acrylic lesion compartment spheres (10, 17, 22, and 28mm). The spheres were connected to an MR-compatible motion stage that was programmed with 3 different motion profiles (2 irregular patient profiles and 1 sinusoidal pattern with a dwell at the bottom third of the cycle). Both the torso and the spheres were filled with MRI fluid and ^{18}F to mimic signals from a patient with lung lesions. Volumetric measurements of 17, 22, and 28 mm segmented spheres volumes in PET showed good agreement with known values in all 4D-PET images. 4D-PET CNR values showed a slight improvement over the single gate reconstructions for 22 and 28 mm spheres and similar values to single gate for the 17 mm sphere. The 10 mm sphere showed poor and inconsistent values for all PET measurements. This was due to a combination of segmentation method failure and inaccurate deformation field calculation between phases for the 10 mm sphere. Centroid displacement measurements for all spheres in all 4D images showed excellent correlation with their ground truth positions in both A-P and S-I directions (r^2 = 0.91 to 1.0, 0.91 to 1.0, 0.92 to 1.0, and 0.85 to 1.0 for 28, 22, 17, and 10 mm spheres respectively).

I conclude that our retrospective 4D-PET-MRI technique with attenuation correction is capable of providing information to characterize tumour respiratory motion while providing the added benefit of using a clinically available pulse sequence and PET acquisition method, eliminating the need for less available more exotic sequences or MR pulse sequence programming. The hypothetical benefits of such a technique include adding complementary information about tumour molecular characteristics and soft-tissue details of MRI to 4D-CT for radiotherapy planning in motion prone anatomy, such as lung and liver.

5.4 Conclusions

The overall goal of this thesis was to develop techniques to overcome two outstanding issues in hybrid PET-MRI: 1) Attenuation correction of MRI hardware composed of dense materials; 2) Quality assurance of motion correction protocols intended for radiotherapy treatment planning. This goal was motivated by the following research questions:

Q1 Can accurate μ-maps be derived from DECT and MVCT images of RF coils, for use in quantitative PET-MR imaging?

Q2 Can a MR-PET compatible motion phantom be designed to evaluate the accuracy and PET sensitivity of respiratory-triggered PET-MRI protocols under controlled conditions?

Q3 Can tumour respiratory motion be characterized using coregistered dynamic 3D MRI and PET volumes?

Chapter 2 of the thesis addressed **Q1**. The DECT-derived virtual monochromatic images noticeably reduced the beam hardening artefacts that were observed in the SECT images. This led to improvements in μ-map accuracy, which is seen as increased homogeneity of PET activity in ROI measurements. However, some metal artefacts remained due to projection truncation and/or photon starvation at lower energies of the two spectra, and threshold values were applied to the μ-map to remove the remaining artefacts. The MVCT images did not contain any visible metal artefacts leading to an artefact-free μ-map, which did not require any other correction strategies to remove artefacts seen in μ-maps calculated from keV energy CT images.

Q2 was addressed within chapter 3 of the thesis. By designing a PET-MRI compatible tumour respiratory motion phantom and then evaluating the accuracy and sensitivity of an already available clinical PET-MRI protocol with it, I was able to fulfill an unmet need for a programmable motion phantom for use in routine quality assurance of multi-modality motion correction protocols.

In chapter 4 of the thesis, I addressed **Q3**. I was able to use pre-existing PET and MRI imaging protocols, which are clinically available on hybrid PET-MRI systems, to develop a 4D-PET-MRI post processing technique. This also eliminates the need for sequences that have limited availability or the need for MR pulse sequence programming. The imaging protocol developed and validated in this chapter can easily be translated into a patient specific imaging protocols for precision radiotherapy, where respiratory motion is a concern, including lung, esophageal, and liver cancer.

5.5 Future Work

5.5.1 MVCT-based μ-maps for Additional Hardware Components

In addition to further validating the MVCT-based μ-map of the four-channel breast coil with patient datasets, this technique could be applied to other types of MRI hardware that typically will be required to be positioned within the PET field of view on hybrid PET-MRI systems. Previous work on correcting for PET attenuation of a head and neck coil found the lock, signal cables, connectors, and most of all the casing between both coils were all important sources of attenuation.[6] A 17% loss of true counts due to its presence was found, which is greater than the ~10% found with the breast coil. This may be a good application for our MVCT-based approach, along with other, more highly attenuating MR hardware.

5.5.2 Development of Routine Quality Assurance Procedures

The development of our tumour respiratory motion fulfills an unmet need for a programmable motion phantom that can be used for quality assurance of motion correction protocols, as well as protocol development. Future work should involve the development of standard procedures for routine quality assurance of protocols to both ensure consistent accuracy of motion correction/characterization, as well as define functional limitations or constraints of such protocols. Further refinement of the phantom design, including development of purpose specific lesion compartments to attach to the motion stage could broaden the phantom's range of uses.

5.5.3 Further Improvements to 4D-PET-MRI Technique

As mentioned in Chapter 4, further improvements to the image registration technique improve the ability to characterize lesions smaller than 17 mm in diameter undergoing motion greater than 1.7 cm. Brehm *et al* uses a cyclic registration technique for motion compensation and found it to outperform spatial registration using demons deformable registration algorithm for motion estimation to obtain the deformation fields between respiratory phases.[7] This strategy may provide the desired improvements. Dutta *et al.* also presented a motion compensated PET/MR technique that uses a novel radial navigated MR pulse sequence to construct up to 12 gates is used to calculate deformation fields between gates.[8] This method proved effective at correcting motion of 10 mm pulmonary lesions in a simulation study. Both of these techniques should be investigated further for their applications to 4D-PET-MRI.

Additionally, exploring the optimization of MRI parameters to increase temporal resolution, and minimize effects to the signal-to-noise ratio and pixel size may allow more phase volumes to be constructed. This could improve motion characterization, as well as minimize any need to supplement missing phase-slice images with their close approximations.

It is hoped that the tools and techniques developed in this thesis will expand the use of quantitative hybrid PET-MRI for radiotherapy planning, to improve conformality of dose to targets while reducing toxicity to healthy tissues, thereby positively influencing the standard of care for cancer patients.

5.6 References

1. Tavallaei MA, Johnson PM, Liu J, Drangova M. Design and evaluation of an MRI-compatible linear motion stage. *Med Phys*. 2016;43(1):62-71.

2. Oppelt A, Graumann R, Barfuss H, Fischer H, Hartl W, Schajor W. FISP—a new fast MRI sequence. *Electromedica*. 1986;54(1):15-18.

3. Pipe JG. Motion correction with PROPELLER MRI: application to head motion and free-breathing cardiac imaging. *Magn Reson Med*. 1999;42(5):963-969.

4. Dixon WT. Simple proton spectroscopic imaging. *Radiology*. 1984;153(1):189-194.

5. Haase A, Frahm J, Matthaei D, Hanicke W, Merboldt K-D. FLASH imaging. Rapid NMR imaging using low flip-angle pulses. *J Magn Reson*. 1986;67(2):258-266.

6. Delso G, Martinez-Moller A, Bundschuh RA, et al. Evaluation of the attenuation properties of MR equipment for its use in a whole-body PET/MR scanner. *Phys Med Biol*. 2010;55(15):4361-4374.

7. Brehm M, Paysan P, Oelhafen M, Kunz P, Kachelrieß M. Self-adapting cyclic registration for motion-compensated cone-beam CT in image-guided radiation therapy. *Med Phys*. 2012;39(12):7603-7618.

8. Dutta J, Huang C, Li Q, El Fakhri G. Pulmonary imaging using respiratory motion compensated simultaneous PET/MR. *Med Phys*. 2015;42(7):4227-4240.

Curriculum Vitae

JOHN PATRICK, Ph.D.

EDUCATION

2017	**Ph.D. in Medical Biophysics** The University of Western Ontario, London, Canada **Thesis:** MR-PET in Lung Cancer Radiotherapy Applications, Including Respiratory Motion Management Strategies **Distinction:** CIHR – STP (Strategic Training Program) in Cancer Research and Technology Transfer (CaRTT) **Technical Training:** Linear Accelerator Quality Assurance Internship
2013	**M.Sc. in Medical Biophysics** The University of Western Ontario, London, Canada **Thesis:** Atlas-based Attenuation Correction for PET/MRI **Distinction:** CIHR – STP (Strategic Training Program) in Vascular Research Scholarship **Additional Training:** REAC/TS – Emergency Management of Radiation Accident Victims
2010	**B.Sc. Honors specialization in Bioinformatics *(Computer Science Concentration)*** The University of Western Ontario, London, Canada **Year 4 Thesis:** Definition of Unique Sequences in Human Genome by *ab initio* Copy Number Determination
2002	**Certificate in Industrial Craftsperson (General Machinist)** Fanshawe College, London, Canada **Apprenticeship:** Phillips Tool and Mould Ltd., London, Canada

EMPLOYMENT

05/2015 – 08/2015 & 05/2014 – 08/2014	**Linear Accelerator Quality Assurance Internship**, London Regional Cancer Program Responsibilities included weekly mechanical, safety, and radiation dosimetry testing on Varian external beam radiotherapy units.
2011 – 2013	**Physics Assistant**, St. Joseph's Health Care - London Responsibilities included Acceptance Testing (NEMA) of PET/MRI, and X-ray CT imaging for Thames Valley Veterinary Services
2005 – Present	**Research Assistant**, Lawson Health Research Institute Machinist/Prototyping Technician & IT support

1998 – 2006	**General Machinist**, Phillips Tool and Mould Ltd.

ACADEMIC SCHOLARSHIPS

2014 – 2015	CIHR Strategic Training Program (CIHR – STP) in Cancer Research and Technology Transfer (CaRTT). [$14,100/year]
2011 – 2016	Western Graduate Research Scholarship (WGRS). [~$2,500/term]
2013 – 2014	Lawson Health Research Institute Internal Research Fund Studentship.
2012 – 2014	Mitacs-Accelerate Internship Program. [$15,000]
2010 – 2012	CIHR – STP in Vascular Research Scholarship. [$12,000/yr]

INVITED TALKS

24/04/2014	**2014 A. C. Burton Day Student Speakership** “Construction of an Attenuation map for a PET/MRI Breast coil”, London, Canada.
28/09/2013	**2013 Biograph mMR User Group Meeting** “MR Attenuation map for mMR Breast coil”, London, Canada.

TEACHING AND SUPERVISING

01/2015 – 05/2015	**Curriculum Design and Development**, “Problem Discovery and Solving” (graduate level course), Department of Medical Biophysics, Western University. Responsibilities included application of formal pedagogical concepts in the design of learning objectives, lecture material, planned exercises, and assessment tools for 0.5 credit graduate level course. (to be offered in the Fall 2015)
10/2013 – 01/2014	**Co-Supervision**, MSc Project of Marianna Inglese from Sapienza Università Di Roma, Department of Biomedical Engineering, Project Title: “Correction of attenuation caused by MRI RF coils in PET images acquired on hybrid PET/MRI platforms”

PUBLICATIONS

J C Patrick, M A Tavallaei, H Biernaski, R T Thompson, R Z Stodilka, M Drangova, and S Gaede. "Comparing the effects of motion magnitude and TR on PROPELLER MRI (BLADE) and respiratory triggered PET with a multimodality tumour motion phantom on MR-PET", The Journal of Nuclear Medicine. *Submitted*

John C. Patrick, R. Terry Thompson, Aaron So, John Butler, David Faul, Frank S. Prato, and Stewart Gaede. "Technical Note: Comparison of Megavoltage and Dual-energy CT-based μ-maps for a 4 Channel Breast Coil in PET/MRI", Medical Physics. *Accepted*

Marshall HR, **Patrick J**, Laidley D, Prato FS, Butler J, Théberge J, Thompson RT, Stodilka RZ. "Description and assessment of a registration-based approach to include bones for attenuation correction of whole-body PET/MRI", Medical physics. 2013 Aug 1;40(8):082509.

Stodilka RZ, Modolo J, Prato FS, Robertson JA, Cook C, **Patrick J**, Beuter A, Thomas AW, Legros A. "Pulsed magnetic field exposure induces lasting changes in neural network dynamics", Neurocomputing. 2011 Jun 30;74(12):2164-75.

Roumeliotis M, Ephrat P, **Patrick J**, Carson JJ. "Development and characterization of an omni-directional photoacoustic point source for calibration of a staring 3D photoacoustic imaging system", Optics express. 2009 Aug 17;17(17):15228-38.

MANUSCRIPTS IN PREPARATION

J.C. Patrick, J Thiessen, D. Capaldi, R.T. Thompson, R.Z. Stodilka, M. Drangova, S. Gaede. "Description and evaluation of an amplitude-based 4D-PET/MRI protocol to characterize tumour respiratory motion", *TBD.*

REPORTS

John C. Patrick, Olfat KamelHasan, Andrea Lum, Robert Stodilka, "Collaborating with the Institute for Clinical Evaluative Sciences (ICES): A Guidance Document for Medical Imaging, Dept. of Medical Imaging", Western Universtity (2014).

Patrick, J, Sabondjian, E, Butler, J, Théberge, J, Thompson, T, Prato, F, & Stodilka, R. "NEMA Report: Acceptance testing of Siemens Biograph mMR PET/MRI", St. Joseph's Health Care London (2013).

Legros, A., Gow, J., McNamee, D., Corbacio, M., **Patrick, J.**, Keenliside, L., & R.Z. Stodilka. "Diagnostic Assessment of Cerebral Impairment in Canadian Forces (CF) Operations – *Phase II, Milestone 2* Final Report", Lawson Health Research Institute (2008)

ORAL PRESENTATIONS

J.C. Patrick, M.A. Tavallaei, F.S. Prato, R.T. Thompson, M. Drangova, S. Gaede, “Development of a PET/MR/CT Compatible Tumour Motion Phantom”, IUPESM World Congress on Medical Physics and Biomedical Engineering (2015), Toronto, Ont., June 7-12, 2015.

John Patrick, “PET/MRI in Lung Cancer Radiotherapy Applications”, Medical Biophysics Departmental Talks (Western University, Canada) – London, Ontario. December 11, 2014.

John C. Patrick, Aaron So, John Butler, David Faul, Slav Yartsev, Terry Thompson, Frank S. Prato, Stewart Gaede, “Constructing an Attenuation map for a PET/MR Breast coil”, 2014 Canadian Organization of Medical Physicists (COMP) Annual Scientific Meeting - J.R. Cunningham young investigator symposium (YIS), Banff, Alberta, July 9 – 12, 2014.

O. El-Sherif, I. Xhaferllari, **J. Patrick**, E. Yu, S. Gaede, “Dosimetric Analysis of Respiratory Induced Cardiac Intrafraction Motion in Left-sided Breast Cancer Radiotherapy”, 2014 Canadian Organization of Medical Physicists (COMP) Annual Scientific Meeting - J.R. Cunningham young investigator symposium (YIS), Banff, Alberta, July 9 – 12, 2014.

John Patrick, Aaron So, John Butler, Slav Yartsev, Terry Thompson, Frank S. Prato, Stewart Gaede, **“**Construction of an Attenuation map for mMR Breast coil”, 2014 Imaging Network Ontario Symposium (ImNO), Toronto, Ont., March 24 – 25, 2014.

John Patrick, “Construction of an Attenuation map for mMR Breast coil”, Medical Biophysics Departmental Talks (Western University, Canada) – London, Ontario. October 3, 2013.

JC Patrick, E Sabondjian, J Théberge, J Butler, G Moran, RT Thompson, J Mandel, R Stodilka, FS Prato, S Gaede
“PET/MRI: First Year Experience”. CARO-COMP 2013 Joint Scientific Meeting – Montreal, Quebec. September 18-21, 2013.

John Patrick, “PET/MRI in Lung Cancer Radiotherapy Applications”, Medical Biophysics Departmental Talks (The University of Western Ontario) – London, Ontario. April 11, 2013.

J Patrick, H Marshal, E Sabondjian, J Butler, I Rachinsky, T Thompson, J Théberge, F Prato, R Stodilka, “The Role of Body Mass & Gender in Atlas Construction in PET/MRI”, Canadian Organization of Medical Physicists (COMP) 58th Annual Scientific Meeting – Halifax, Nova Scotia, July 13, 2012.

H.R. Marshall, D.T. Laidley, MD, **J. Patrick**, BSc, J. Butler, BSc, R.T. Thompson, PhD, F. Prato, I. Rachinsky, MD, MSc, R.Z. Stodilka, PhD, “Three MRI-based attenuation correction methods for PET.”, Society of Nuclear Medicine (SNM) 2012 Annual Meeting – Miami Beach, Florida, June 9-13, 2012.

John Patrick, “The Role of BMI & Gender in Atlas Design for PET/MRI”, Medical Biophysics Departmental Talks (Western University, Canada) – London, Ontario. March 8, 2012.

John Patrick, Ben Shirley, Stephanie Dorman, Natasha Caminsky, “FISH and aCGH Microarray Probe Design Using Ab Initio Methods”, Ontario Centres of Excellence (Connections Student Presentation Forums) – London, Ontario. April 7, 2011.

John Patrick, “Atlas-based Attenuation Correction for Whole-body PET/MRI”, Medical Biophysics Departmental Talks (The University of Western Ontario) – London, Ontario. March 31, 2011.

P.K. Rogan, **J.C. Patrick**. “Definition of Unique Sequences in Human Genome by ab initio Copy Number Determination”. SHARCNET Research Day - York University, May 6th, 2010.

Patrick J., Rogan P. “Identifying unique sequences directly from the human genome”. UWO Research in Computer Science Conference (UWORCS) –London, Ontario. April 12th, 2010.

Stodilka, R.Z., Legros, A., Sabondjian, E., **Patrick, J**., Robertson, J., Prato, F.S., & A.W. Thomas. “Eliciting A Brain Model To Respond To Simple and Complex Stimuli”. BioEM 2009 Davos, Switzerland, June 14-19, 2009.

POSTER PRESENTATIONS

John C. Patrick, Mohammad A. Tavallaei, R. Terry Thompson, Robert Z. Stodilka, Maria Drangova, and Stewart Gaede, “Image Quality Comparisons of Different Motion Magnitudes and TR Values in MR-PET”, AAPM 58th Annual Meeting & Exhibition – Washington, DC. July 31st – August 4th, 2016.

J.C. Patrick, M.A. Tavallaei, R.Z. Stodilka, R.T. Thompson, M. Drangova, and S. Gaede, “Impact of Motion Magnitude and TR in Respiratory-Triggered MR-PET”, The 13th Annual Oncology Research & Education Day – London, Ontario. June 26th, 2016. *Submitted*

J.C. Patrick, M.A. Tavallaei, R.T. Thompson, F.S. Prato, M. Drangova, S. Gaede, “Development of a Tumour Motion Phantom for PET, MRI, and CT”, The 12th Annual Oncology Research & Education Day – London, Ontario. June 26th, 2015.

J.C. Patrick, M.A. Tavallaei, F.S. Prato, R.T. Thompson, M. Drangova, S. Gaede, “Construction of a PET/MR/CT Compatible Tumour Motion Phantom”, London Health Research Day (2015) – London, Ont., April 1, 2015.

J.C. Patrick, M.A. Tavallaei, F.S. Prato, R.T. Thompson, M. Drangova, S. Gaede, “Tumour Motion Phantom for PET/MRI/CT”, 2015 Imaging Network Ontario Symposium (ImNO) – London, Ont., March 30 – 31, 2015.

John Patrick, John Butler, Terry Thompson, Frank Prato, Stewart Gaede, “Constructing an Attenuation Map for a PET/MRI Breast Coil Using MVCT”, The 11th Annual Oncology Research & Education Day – London, Ontario. June 20th, 2014.

John C. Patrick, Aaron So, John Butler, Slav Yartsev, Terry Thompson, Frank S. Prato, Stewart Gaede, “Construction of an Attenuation map for mMR Breast coil”, 2014 Imaging Network Ontario Symposium (ImNO) – Toronto, Ont., March 24 – 25, 2014.

JC Patrick, E Sabondjian, J Théberge, J Butler, G Moran, RT Thompson, J Mandel, R Stodilka, FS Prato, S Gaede, “PET/MRI: First Year Experience”. CARO-COMP 2013 Joint Scientific Meeting – Montreal, Quebec. September 18 – 21, 2013.

John Patrick, Harry Marshall, John Butler, Terry Thompson, Frank Prato, Stewart Gaede, and Robert Stodilka. “Body Mass and Gender Considerations for Atlas-based Attenuation Correction in PET/MRI”. 8th Annual London Imaging Discovery Forum – London, Ontario. June 13, 2013.

Patrick JC, Marshall H, Butler J, Rachinsky I, Thompson T, Théberge J, Prato F, Stodilka RZ. “Atlas Construction for PET/MRI Attenuation Correction in an Oncology Population”, The 9th Annual Oncology Research & Education Day – London, Ontario. June 22nd, 2012.

Patrick, John, Marshall, Harry R., Sabondjian, Eric, Butler, John, Theberge, Jean, Thompson, Robert T., Prato, Frank, Stodilka, Robert Z. “Importance of gender and BMI in atlas design for PET/MRI attenuation correction”, Society of Nuclear Medicine (SNM) 2012 Annual Meeting – Miami Beach, Florida. June 9 – 13, 2012.

D.T. Laidley, MD, H.R. Marshall, **J. Patrick**, BSc, J. Butler, BSc, F. Prato, R.T. Thompson, PhD, I. Rachinsky, MD, MSc, R.Z. Stodilka, PhD, “Performance of PET/MRI attenuation correction in an oncology population.”, Society of Nuclear Medicine (SNM) 2012 Annual Meeting – Miami Beach, Florida. June 9 – 13, 2012.

John Patrick, Harry Marshall, Eric Sabondjian, John Butler, Jean Theberge, Terry Thompson, Irina Rachinsky, Frank Prato, Robert Stodilka, “BMI and Gender Dependence in Atlas Construction for Attenuation Correction in PET/MRI”, London Health Research Day – London, Ontario. March 20, 2012.

Harry Marshall, Frank S. Prato, **John Patrick**, David Laidley, John Butler, Jean Theberge, R. Terry Thompson, Robert Z. Stodilka, “To segment, to register, or to map? A comparison of three MRI-based attenuation correction methods for whole-body PET.”, London Health Research Day – London, Ontario. March 20, 2012.

H. R. Marshall, D. Laidley, **J. Patrick**, J. Butler, R. T. Thompson, J. Theberge, F. S. Prato, R. Z. Stodilka, “Attenuation correction in whole-body PET/MRI imaging”, Imaging Network Ontario (ImNO) Annual Symposium – Toronto, Ontario. February 13 – 14, 2012.

Eric Sabondjian, **John Patrick**, Robert Z Stodilka, Martin E King, Gerald Wisenberg, Frank S Prato. “Cardiac SPECT/CT: Comparing Slow-Rotation and Fast-Rotation CT for Attenuation Correction in Cardiac Imaging”, Joint American Association of Physicists in Medicine (AAPM)/ Canadian College of Physicists in Medicine (COMP) Meeting – Vancouver, British Columbia. July 31 – August 4, 2011.

John Butler, Jodi Miller, Harry Marshall, Ali Silavi, **John Patrick**, William Pavlosky, Gregor Reid, Don Taves, Jamie Gregor, Khalil Sultan, Frank S. Prato, Terry Thompson, Rob Stodilka. “MRI-based 3D Volumetric Serial Assessments of Physiologic Large Intestine Gas - Proof of Principle”, International Society for Magnetic Resonance in Medicine 19th Annual Meeting & Exhibition – Montreal, Quebec. May 7 – 13, 2011.

H.R. Marshall, **J. Patrick**, R. Z. Stodilka, B. Lewden, J. Theberge, E. Sabondjian, A. Legros, A. Mitchell, L. Dorrington, J. Sykes, R. T. Thompson, and F. S. Prato. “Attenuation correction in PET/MRI versus SPECT/MRI”, Imaging Network Ontario (ImNO) Annual Symposium. – Toronto, Ontario. January 31 – February 1, 2011.

J.C. Patrick, B.C. Shirley, P.K. Rogan. “Identifying unique sequences directly from the human genome”. The American Society of Human Genetics 60th Annual Meeting – Washington DC. November 2-6, 2010.

AFFILIATIONS

Student Member	Canadian Organization of Medical Physicists (COMP)
Student Member	American Association of Physicist in Medicine (AAPM)